RESORBABLE NANOCOMPOSITES FOR BONE REMODELING IN WEIGHT-BEARING FRACTURES

By

Sichang Lu

Dissertation

Submitted to the Faculty of the

Graduate School of Vanderbilt University

in partial fulfillment of the requirements

for the degree of

DOCTOR OF PHILOSOPHY

in

Chemical Engineering

December 16, 2017

Nashville, Tennessee

Approved:

Scott Guelcher, Ph.D.

Matthew Lang, Ph.D.

Julie Sterling, Ph.D.

Jamey Young, Ph.D.

ACKNOWLEDGEMENTS

First, I would like to acknowledge the funding sources that have supported this work, including National Institute of Arthritis and Musculoskeletal and Skin Diseases of the National Institute of Health, Orthopaedic Trauma Extremity Research Program, Armed Forces Institute of Regenerative Medicine, US Army Institute of Surgical Research, Medtronic, Inc., and National Science Foundation.

I would like to express great gratitude to my research advisor, Dr. Scott Guelcher, for his tremendous instruction and support during my entire Ph.D. training course, which have enabled me to grow into a more independent researcher who is confident to express her opinions, enjoys problem-solving and discovering new findings. Dr. Guelcher is a very responsible and enthusiastic mentor. Although he has a very busy schedule meeting with people and writing grants, he always takes the time to discuss data and new ideas with his students. He is always excited about our findings and inspires us to try new things. Dr. Guelcher’s passion for scientific research has had a great influence on me. I would also like to thank my committee members for their help over the course of my time here: Dr. Matthew Lang, Dr. Julie Sterling, and Dr. Jamey Young. Their advice and feedback after each committee meeting enabled me to accomplish my research objectives.

I feel very fortunate to work with great collaborators on many different projects. I would like to thank Dr. Julie Sterling and her lab, especially Alyssa Merkel, for their expertise and support on bone biology. Also thank you to Dr. Joseph Wenke at US Army Institute of Surgical Research, Dr. Jeffrey Nyman and Sasidhar Uppuganti at the Biomechanics Lab, Dr. Tony Hmelo and Dr. Dmitry Koktysh at Vanderbilt Institute of Nanoscale Science and Engineering, Dr. Jenny Schafer at Vanderbilt Cell Imaging Shared Resource, and Dr. Dan Shimko, Dr. Kerem Kalpakci, Cheyenne Rhodes and Bre Jacobs from Medtronic.

I would also like to acknowledge the help and friendship I have received from the Chemical and Biomolecular Engineering Department. Special thanks to our lab manager, Katarzyna Zienkiewicz, who is incredibly supportive in every aspect of lab work. Thank you to former students (Dr. Ruijing Guo, Dr.

Jon Page, Dr. Drew Harmata, and Dr. Anne Talley) for helping me get started on each project. Dr. Margarita Prieto-Ballangee, Dr. Elizabeth Adolph, Madison McGough, Joe Vanderburgh, Tom Spoonmore, Dustin Groff, Lauren Boller, Greg Lowen and David Florian all made my time in the lab much more enjoyable. Thank you to the Chemical Engineering staff Rae Uson, Mary Gilleran, Angie Pernell, and Mark Holmes for all of the help during my tenure.

Finally, I would like to acknowledge my family and friends who have supported me through these years. Thank you to my parents, my aunt, uncle and cousin, for their love and support. I could not have accomplished my Ph.D. without you. I also want to thank all my friends in China and in the US for the support and inspiration in every aspect of life.

Overall, I would also like to acknowledge Vanderbilt University for providing such a supportive and friendly environment for international students and scholars. I feel grateful to have the opportunity to participate in various activities, meet friends from different culture backgrounds and cultivate myself to become an open-minded person.

TABLE OF CONTENTS

Chapter

LIST OF TABLES

LIST OF FIGURES

CHAPTER 1 - INTRODUCTION

As the main component of the human skeletal system, bone serves important functions in our daily lives, including providing mechanical support, protecting vital organs, and providing metabolic function. However, bone diseases are very common. In the United States, an estimated 1.5 million individuals suffer from bone fractures annually.[1] Large volumetric bone loss caused by trauma, disease, or congenital defects often requires bone grafting procedures.[2-4] Since 1990, the number of bone grafting procedures per year has been increasing, surpassing 1.6 million per year in 2005, and is expected to double in the next 25years.[5]

Intra-articular fractures (e.g., tibial plateau fractures) involve a weight-bearing joint which is subjected to repetitive, dynamic physiological loading from daily activities, and are thus more challenging to treat.[6] These fractures require open reduction and internal fixation along with subchondral grafting to maintain articular congruency of the fracture. Poor articular reduction, joint instability, and mal-alignment of tibial plateau fractures can contribute to poor outcomes in the knee, including post-traumatic osteoarthritis and early total joint arthroplasty.[7, 8]

Current treatment for intra-articular fractures requires implantation of orthopedic prosthetics. Despite the compelling need for bone grafting, current orthopedic implant materials do not fulfill all the requirements for successful bone grafts, and do not guarantee the patient's ability to return to his or her normal active lifestyle. Specifically, current orthopedic implant materials have average lifetime of only 10-15 years, due to lack of integration with host bone and/or differences in mechanical properties between host bone and implants.[9-14] Therefore, researchers have focused on developing biomaterials that provide both biological functionality and load-bearing capacity. An ideal bone graft for treatment of defects at weight-bearing sites provides bone-like strength, stimulates osteogenic differentiation and mineralization, resorbs at a rate aligned with patient biology, and provides favorable handling properties (i.e., can be easily manipulated, shaped, or injected into a defect, allowing for adaption to irregularly shaped defects and avoiding invasive surgical procedures).

Polyurethanes (PURs) can be prepared by reactive liquid molding of two liquid reactants and set *in situ* to form rigid networks, thus are suitable for injection of bone cements. Lysine-derived PUR networks have been reported to induce minimal inflammatory response when implanted *in vivo,* support cellular infiltration and new bone formation, and degrade into non-cytotoxic decomposition products.[15-24] To improve osteoconductivity of lysine-derived PUR networks, mineralized microparticles (e.g., ceramics, allograft bone particles) have been incorporated with lysine-derived PUR networks to form composites in which the particles provide biological functionality and the polymer phase enhances the toughness.[25-30] While results from pre-clinical studies highlight the potential of PUR composites as suitable biomaterials for bone tissue engineering, further investigation on improving load-bearing capacity and resorption of the composites is needed.

The merging of nanotechnology and orthopedics provides an exciting opportunity to improve materials used for bone regeneration. Nanoscale materials (with features ranging from 1-100 nm) result in superior properties compared to their conventional counterparts or micron structured materials. Specifically, biomaterials with nanoscale features mimicking the nanostructure of natural bone can directly interact with cells, stimulate cell growth, and guide tissue regeneration.[31] In addition, the unique surface properties of nanomaterials can also mediate adsorption of proteins which are essential for cell attachment, and further regulate cell behaviors.[31]

The goal of this dissertation was to design PUR-based nanocomposite bone grafts that possess both biological functionality and load-bearing capacity for treatment of bone defects at weight-bearing sites. Novel nanocrystalline hydroxyapatite (nHA)-poly(ester urethane) (PEUR) nanocomposites were synthesized by a novel solvent-free grafting reaction to meet this goal. *In vitro* characterization included chemical reaction, rheology, mechanical properties, protein adsorption, and cell culture analysis.[32] The nanocomposites were further tested *in vivo* in a weight-bearing ovine tibial plateau model to evaluate remodeling under physiological loading. In order to fully understand the remodeling of the resorptive components in the graft, *in vitro* osteoclast culture experiments were conducted to allow for quantitative comparison of osteoclast-mediated volume resorption rates on synthetic substrates.

Chapter III reports novel injectable and settable nHA-PEUR nanocomposites prepared from PUR and nanocrystalline hydroxyapatite (nHA) particles that meet the targeted properties for resorbable weight-bearing bone cements. The composites can be injected by simple mixing using a two-component syringe. A solvent-free process for grafting lysine triisocyanate (LTI) to nHA particles was used to fabricate the nanocomposites. Detailed characterization of the grafting reaction and its effect on nHA dispersion, mechanical properties, osteoblast mineralization and osteoclast-mediated resorption of the nanocomposites are presented. This chapter has been published as a journal article titled "Resorbable Nanocomposites with Bone-Like Strength and Enhanced Cellular Activity" in Journal of Materials Chemistry B, 2017, 5, 4198. [32]

Chapter IV presents a detailed study on the grafting reaction of LTI to nHA described in Chapter III. In order to keep the material stable during storage, it is essential to achieve 100% conversion of surface hydroxyl groups of nHA through the grafting reaction. The grafting reaction was conducted under different conditions and characterized by FTIR. Surface Nitrogen/Phosphorous ratio of nHA particles and the change in %NCO (i.e., the wt% of reactive isocyanate groups) of the reaction mixture were measured as markers for the extent of the reaction. In addition, several methods for calculating the theoretical equivalent weight of nHA (i.e., the mass of nHA that corresponds to one mole of reactive surface hydroxyl group) are discussed.

Chapter V incorporates the injectable nHA-PEUR nanocomposites described in Chapter III with ceramic mini-granules to form settable, resorbable bone grafts that can be easily shaped by hand before hardening. The grafts were tested in weight-bearing sheep tibial plateau defects and non-weight-bearing sheep femoral plug defects. Two questions were to be investigated: (a) do the grafts maintain mechanical stability as being resorbed under physiological loading; (b) how mechanical loading affects graft remodeling *in vivo*. Static compressive properties as well as dynamic fatigue properties of the grafts were investigated. Microcomputed tomography (μCT), histology and histomorphometry analysis were performed to evaluate remodeling progression.

In order to design bone grafts that undergo active remodeling and effectively integrate with host bone, a detailed understanding of osteoclast-mediated resorption on different substrates is needed. **Chapter VI** presents a standardized, quantifiable method to analyze relative osteoclast resorption rates on synthetic substrates, including hydroxyapatite (HA), β-tricalcium phosphate (β-TCP), dentin and bioactive glass (BG), using co-culture technique based on established cell lines. Osteoclast formation and activity were measured by actin/DAPI staining and tartrate-resistant acid phosphatase (TRAP) activity. Rates of resorption of the substrates relative to that of dentin were calculated from optical profilometry measurements of resorption area at three time points.

To conclude, **Chapter VII** summarizes the main findings presented in this dissertation and lists suggestions for future studies. As a whole, this dissertation presents advancements in the development of PUR-based synthetic grafts for bone repair and restoration at weight-bearing sites.

References

1. Smith, R., *Bone Health and Osteoporosis: A Report of the Surgeon General*. 2004, US Department of Health and Human Services, Public Health Service, Office of the Surgeon General: Rockville, MD. p. 68-70.
2. Lew, T.A., et al., *Characterization of Craniomaxillofacial Battle Injuries Sustained by United States Service Members in the Current Conflicts of Iraq and Afghanistan.* Journal of Oral and Maxillofacial Surgery, 2010. **68**(1): p. 3-7.
3. Ward, B.B., S.E. Brown, and P.H. Krebsbach, *Bioengineering strategies for regeneration of craniofacial bone: a review of emerging technologies.* Oral Diseases, 2010. **16**(8): p. 709-716.
4. Costello, B.J., et al., *Regenerative Medicine for Craniomaxillofacial Surgery.* Oral and Maxillofacial Surgery Clinics of North America, 2010. **22**(1): p. 33-+.
5. *US Census Bureau Stastical Abstracts of the United States*, U.C. Bureau, Editor. 2006: Washington, DC.
6. Ramakrishna, S., et al., *Biomedical applications of polymer-composite materials: a review.* Composites Science and Technology, 2001. **61**(9): p. 1189-1224.
7. Rivera, J.C., et al., *Posttraumatic Osteoarthritis Caused by Battlefield Injuries: The Primary Source of Disability in Warriors.* Journal of the American Academy of Orthopaedic Surgeons, 2012. **20**: p. S64-S69.
8. Anderson, D.D., et al., *Is Elevated Contact Stress Predictive of Post-Traumatic Osteoarthritis for Imprecisely Reduced Tibial Plafond Fractures?* Journal of Orthopaedic Research, 2011. **29**(1): p. 33-39.
9. Webster, T.J., *Nanophase ceramics as improved bone tissue engineering materials.* American Ceramic Society Bulletin, 2003. **82**(6): p. 23-28B.
10. Buser, D., et al., *Interface shear strength of titanium implants with a sandblasted and acid-etched surface: A biomechanical study in the maxilla of miniature pigs.* Journal of Biomedical Materials Research, 1999. **45**(2): p. 75-83.
11. Webster, T.J., *Nanophase ceramics: The future orthopedic and dental implant material.* Advances in Chemical Engineering, 2001. **27**: p. 125-166.
12. Simon, S.R. and A.A.o.O. Surgeons, *Orthopaedic Basic Science*. 1994: American Academy of Orthopaedic Surgeons.
13. Daniels, A.U., et al., *Mechanical-Properties of Biodegradable Polymers and Composites Proposed for Internal-Fixation of Bone.* Journal of Applied Biomaterials, 1990. **1**(1): p. 57-78.
14. Terjesen, T. and K. Apalset, *The Influence of Different Degrees of Stiffness of Fixation Plates on Experimental Bone Healing.* Journal of Orthopaedic Research, 1988. **6**(2): p. 293-299.
15. Bennett, S., et al., *Initial biocompatibility studies of a novel degradable polymeric bone substitute that hardens in situ.* Bone, 1996. **19**(1): p. S101-S107.
16. Adolph, E.J., et al., *Injectable polyurethane composite scaffolds delay wound contraction and support cellular infiltration and remodeling in rat excisional wounds.* Journal of Biomedical Materials Research Part A, 2012. **100A**(2): p. 450-461.
17. Page, J.M., et al., *Biocompatibility and chemical reaction kinetics of injectable, settable polyurethane/allograft bone biocomposites.* Acta Biomaterialia, 2012. **8**(12): p. 4405-4416.
18. Borkenhagen, M., et al., *In vivo performance of a new biodegradable polyester urethane system used as a nerve guidance channel.* Biomaterials, 1998. **19**(23): p. 2155-2165.
19. Guelcher, S., et al., *Synthesis, In vitro degradation, and mechanical properties of two-component poly(ester urethane)urea scaffolds: Effects of water and polyol composition.* Tissue Engineering, 2007. **13**(9): p. 2321-2333.

20. Guelcher, S.A., et al., *Synthesis and in vitro biocompatibility of injectable polyurethane foam scaffolds.* Tissue Engineering, 2006. **12**(5): p. 1247-1259.
21. Zhang, J.Y., et al., *A new peptide-based urethane polymer: synthesis, biodegradation, and potential to support cell growth in vitro.* Biomaterials, 2000. **21**(12): p. 1247-1258.
22. Zhang, J.Y., et al., *Synthesis, biodegradability, and biocompatibility of lysine diisocyanate-glucose polymers.* Tissue Engineering, 2002. **8**(5): p. 771-785.
23. Elliott, S., et al., *Identification of biodegradation products formed by L-phenylalanine based segmented polyurethaneureas.* Journal of Biomaterials Science-Polymer Edition, 2002. **13**(6): p. 691-711.
24. Saad, B., et al., *Development of degradable polyesterurethanes for medical applications: In vitro and in vivo evaluations.* Journal of Biomedical Materials Research, 1997. **36**(1): p. 65-74.
25. Dumas, J.E., et al., *Synthesis, characterization, and remodeling of weight-bearing allograft bone/polyurethane composites in the rabbit.* Acta Biomaterialia, 2010. **6**(7): p. 2394-2406.
26. Dumas, J.E., et al., *Synthesis and Characterization of an Injectable Allograft Bone/Polymer Composite Bone Void Filler with Tunable Mechanical Properties.* Tissue Engineering Part A, 2010. **16**(8): p. 2505-2518.
27. Dumas, J.E., et al., *Injectable reactive biocomposites for bone healing in critical-size rabbit calvarial defects.* Biomedical Materials, 2012. **7**(2).
28. Yoshii, T., et al., *Synthesis, characterization of calcium phosphates/polyurethane composites for weight-bearing implants.* Journal of Biomedical Materials Research Part B-Applied Biomaterials, 2012. **100B**(1): p. 32-40.
29. Dumas, J.E., et al., *Balancing the Rates of New Bone Formation and Polymer Degradation Enhances Healing of Weight-Bearing Allograft/Polyurethane Composites in Rabbit Femoral Defects.* Tissue Engineering Part A, 2014. **20**(1-2): p. 115-129.
30. Adhikari, R., et al., *Biodegradable injectable polyurethanes: Synthesis and evaluation for orthopaedic applications.* Biomaterials, 2008. **29**(28): p. 3762-3770.
31. Tran, N. and T.J. Webster, *Nanotechnology for bone materials.* Wiley Interdisciplinary Reviews-Nanomedicine and Nanobiotechnology, 2009. **1**(3): p. 336-351.
32. Lu, S., et al., *Resorbable Nanocomposites with Bone-like Strength and Enhanced Cellular Activity*. Journal of Materials Chemistry B, 2017. **5**(22): p. 4198-4206.

CHAPTER 2 - BACKGROUND

General principles for bone tissue engineering

Tissue engineering was defined by Vacanti in 1997 as the application of “the principles of engineering and the life sciences toward the development of biological substitutes that restore, maintain, or improve tissue function”. Bone tissue engineering aims to repair bone defects caused by disease, trauma or congenital defects.

Bone is a dynamic tissue that constantly undergoes remodeling in the body. Bone remodeling starts with bone-degrading osteoclasts resorbing the bone, followed by bone-forming osteoblasts laying down new bone matrix to fill resorption lacunas. Osteoblasts and osteoclasts act in balance in maintaining bone integrity and in response to injuries.

Bones have complex structures which contribute to their light weight and high strength. Specifically, bone is a natural nanostructured composite composed of organic compounds (mainly collagen) reinforced with an inorganic phase (various forms of nanocrystalline calcium phosphates).[1] Although the properties and structure of bone can significantly differ depending on anatomical location, the natural nanostructure is common between all bone types.

Researchers in bone tissue engineering have been working to develop alternative materials to autografts and allografts in order to address the growing clinical need for bone grafting materials for different types of bone defects. The essential characteristics for bone grafts and considerations for graft design include:

(a) Biocompatibility, which is the most important property. It is defined by Williams in 2008 as the ability of the material “to perform its intended function, including an appropriate degradation profile, without eliciting any undesirable local or systemic effects in that host”.[2]

(b) Osteoconductivity is the ability for the material to provide a surface that encourages cells to adhere, proliferate, and produce bone.

(c) Interconnectivity means the material needs to have interconnected pores for nutrient and waste transport for the survival of cells. Studies have suggested the minimal pore size for bone formation is 100 μm.[3-6]

(d) Biodegradability is the ability of the material to degrade *in vivo*. There are varies degradation mechanisms, such as physiochemical degradation, cell-mediated degradation and mechanical degradation, etc.[7, 8]

(e) Bioactivity refers to the tendency of the material to form chemical bonds with host bone.

(f) Osteoinductivity is the ability of the material to induce bone formation by stimulating differentiation of osteoprogenitor cells to osteoblasts.

(g) Manufacturability refers to the ease and flexibility to fabricate the material.

(h) Mechanical integrity refers to the ability of the material to maintain bone-like strength while actively remodeling until complete healing. Compressive, flexural (bending) and tensile strength as well as elastic modulus for human cortical and trabecular (cancellous) bone are summarized in **Table 2.1**, which is reprinted from ref. [9]

Table 2.1 Summary of the mechanical properties of human bone. Reprinted from Acta Biomaterialia, 7, Amy J. Wagoner Johnson and Brad A. Herschler, A Review of the Mechanical Behavior of CaP and CaP/Polymer Composites for Applications in Bone Replacement and Repair, Page No. 17, Copyright (2011), with permission from Elsevier.

	Compressive Strength (MPa)	**Flexural Strength (MPa)**	**Tensile strength (MPa)**	**Modulus (GPa)**	**Porosity (%)**
Cortical bone	130-180	135-193	50-151	12-18	5-13
Cancellous bone	4-12	NA	1-5	0.1-0.5	30-90

NA indicates data not available.

Grafting materials for bone tissue engineering

Autografts (bone harvested from the patient) are considered the golden standard for bone defect repair due to their osteoconductive, osteoinductive and osteogenic properties. However, there are multiple complications and risks associated with the use of autografts and allografts (from a donor), such as limited supply, morbidity at the donor site, and safety issues with allografts.[10-12] While autografts and allografts are appropriate options for some simple and non-load-bearing defects, for many applications the use of autografts and allografts is not an option. As a result, researchers are working on development of synthetic bone grafts that promote healing of various types of bone defects in order to meet the clinical needs.

PMMA cements

Poly(methyl methacrylate) (PMMA) bone cements were approved by the U. S. Food and Drug Administration (FDA) in the 1970's for use in arthroplastic procedure of the hip, knee and other joints for fixation of implants. PMMA cements act as space filler that hold the implant against the bone. They are formed by mixing a liquid MMA monomer phase with a powdered MMA-styrene co-polymer phase.[13] When the two phases are mixed, the liquid monomer polymerizes around the powdered co-polymer and forms hardened PMMA. In addition, various additives are added to the system, including hydroquinone as stabilizer, di-benzoyl peroxide (BPO) as initiator, N, N-dimethyl-p-toluidine (DmpT) as accelerator, and zirconium dioxide (ZrO_2) or barium sulphate ($BaSO_4$) as contrast agent in order to make the cement radiopaque.

PMMA cements have several unique properties that make them useful as bone grafting materials. For example, antibiotics can be added to the formulation, which makes PMMA bone cements capable of delivering drugs directly to the surgical sites. In order to be incorporated with PMMA cements, the antibiotics need to be heat resistant and last for longer duration of time. Various antibiotics, including Gentamycin, Erythromycin, Cefuroxime, Tobramycin, Vancomycin, have been successfully used with PMMA bone cements. Studies have shown that adding antibiotics in quantities < 2 g per standard packet of PMMA does not have adverse effect on mechanical properties of PMMA.[13]

Other than delivering antibiotics, PMMA cements also exhibit high strength and provide mechanical compatibility with host bone, which makes them the only biomaterial indicated for bone structural repair. Performance requirements for PMMA cements have been established, including compressive strength of 70-90 MPa, compressive modulus of 2000-3000 MPa, bending strength ≥ 70 MPa, and bending modulus ≥1800 MPa (**Table 2.2**).[14, 15]

Table 2.2 Mechanical requirements for PMMA bone cements

Compressive Strength (MPa)	Elasticity Modulus (MPa)	Bending Strength (MPa)	Bending Modulus (MPa)
70-90	2000-3000	≥70	≥1800

One of the major drawbacks of PMMA cements is biologically inertness. They are neither osteoconductive nor osteoinductive, and do not remodel, which causes long-term problems such as device loosening and failure.[16-20] The wear debris from PMMA cements promotes local inflammatory activity, resulting in chronic complications, such as prosthetic loosening and periprosthetic osteolysis.[21]

In addition to being biologically inert, current PMMA bone cements have other issues, for example, the preparation of PMMA cements involves mixing a liquid phase with powder and waiting for the viscosity of the system to become workable. Once the polymerization process of PMMA is initialized by mixing, the workable time is very limited. Failure to place PMMA cements within the working time results in leakage of toxic monomer to the surrounding tissue or filling the defect inadequately.[22] Another disadvantage of PMMA cements is that the reaction to form the cement is highly exothermic. The temperature of the polymerization reaction can reach up to 82-86 °C in the body, which is harmful to the surrounding host tissue.[13]

Research studies have been conducted to address the drawbacks of PMMA cements, mainly in the field of enhancing bone – cement interface by addition of bioactive additives, such as HA, β-TCP, bioactive glass, and sodium fluoride.[23-26]

Ceramics

Ceramics (e.g., metallic oxides, calcium phosphates, glass ceramics) have been used widely for orthopedic applications due to their biocompatibility with bone cells and tissues.[27-29] They are also considered bioactive because their surface properties support bone cell adhesion, proliferation and differentiation. Specific ceramic materials such as HA and tricalcium phosphate (TCP) have similar chemistry composition to the mineral component of natural bone, and create strong bond to tissues when react with physiological fluids. These bioactive ceramics also have a high affinity for cell adhesion proteins and growth factors, thus are also appropriate carriers for growth factors.

Among a wide range of ceramics used for orthopedic applications, calcium phosphates have been studied most extensively and have been used as fillers for treatment of bone defects.[30] Three types of calcium phosphates have received most attention: hydroxyapatite (HA, $Ca_5(PO_4)_3(OH)$, calcium to phosphate ratio=1.67), β-tricalcium phosphate (β-TCP, $Ca_3(PO_4)_2$, calcium to phosphate ratio=1.5), and biphasic calcium phosphate (BCP, composites of HA and β-TCP with no specific ratio).[31, 32] The most well-known difference between HA and β-TCP is their degradation rates. TCPs have a much shorter degradation time compared to HA, and HA is considered relatively non-degrading.[33]

Calcium Phosphate Cements (CPCs)

First created in the 1980s, calcium phosphate cements (CPCs) are extensively studied for repair of load-bearing bone defects. Despite of varying compositions, CPCs are generally produced by a reaction between a solid and a liquid phase. The solid phase consists of one or several kinds of calcium phosphate, and the liquid phase is usually water or a solution containing calcium or phosphate. When the two phases are mixed, needle-like or plate-like calcium phosphate crystals precipitate from the solution due to oversaturation. The entanglement of the precipitated needle-like or plate-like calcium phosphate crystals results in setting and hardening of the cement.[34]

This unique property gives one of the main advantages of CPCs - injectable and settable *in vivo* at body temperature. After mixing of the solid and liquid phase, CPCs form a paste that progressively sets and hardens into a solid mass. The paste can be easily manipulated, shaped or injected into a defect, which allows for adaption to irregularly shaped defects and avoids invasive surgical procedures.

The final product for the CPC reaction after setting is brushite or apatite, which has excellent biological properties. Brushite is 1-2 orders of magnitude more soluble than apatite at physiological pH, and may transform to apatite *in vivo*. Apatite is similar to the mineral composition found in mammalian bones. CPCs have shown to be osteoconductive, and can be resorbed by osteoclasts *in vitro* and *in vivo.* In an *in vitro* study, RAW 264.7 cells formed multinucleated TRAP positive osteoclast-like cells when cultured on brushite CPCs.[35] Phenotypic characteristics of osteoclasts including formation of sealing zone and ruffled border were observed by ultra-structural analysis of SEM. Furthermore, evidence of osteoclasts penetrating deep inside the surface of the cements suggests that the cements were demineralized by osteoclast-mediated resorption *in vitro*. In an *in vivo* study, CPCs were injected into proximal tibia metaphyseal and distal femoral metaphyseal defects in dogs and were evaluated through 78 weeks.[36] Histological analysis showed the cements were osteoconductive *in vivo*, with the entire surface area of cements covered with bone two weeks after surgeries. The cements underwent gradual remodeling by osteoclast mediated resorption associated with adjacent new bone formation, and were gradually replaced by bone.

Although CPCs seem are promising for bone regeneration, the main issue that limits CPCs for weight-bearing applications is generally low mechanical strength. Although the compressive strength of CPCs is comparable to that of cortical bone, their low fracture toughness and poor mechanical reliability preclude their use for bone repair at weight-bearing sites. In a weight-bearing ovine tibial plateau model, CPCs revealed cracks within the cement and gaps between the host bone and the implants (**Figure 2.1**), and thus can only be used as bone void fillers or be stabilized with additional hardware.[37, 38]

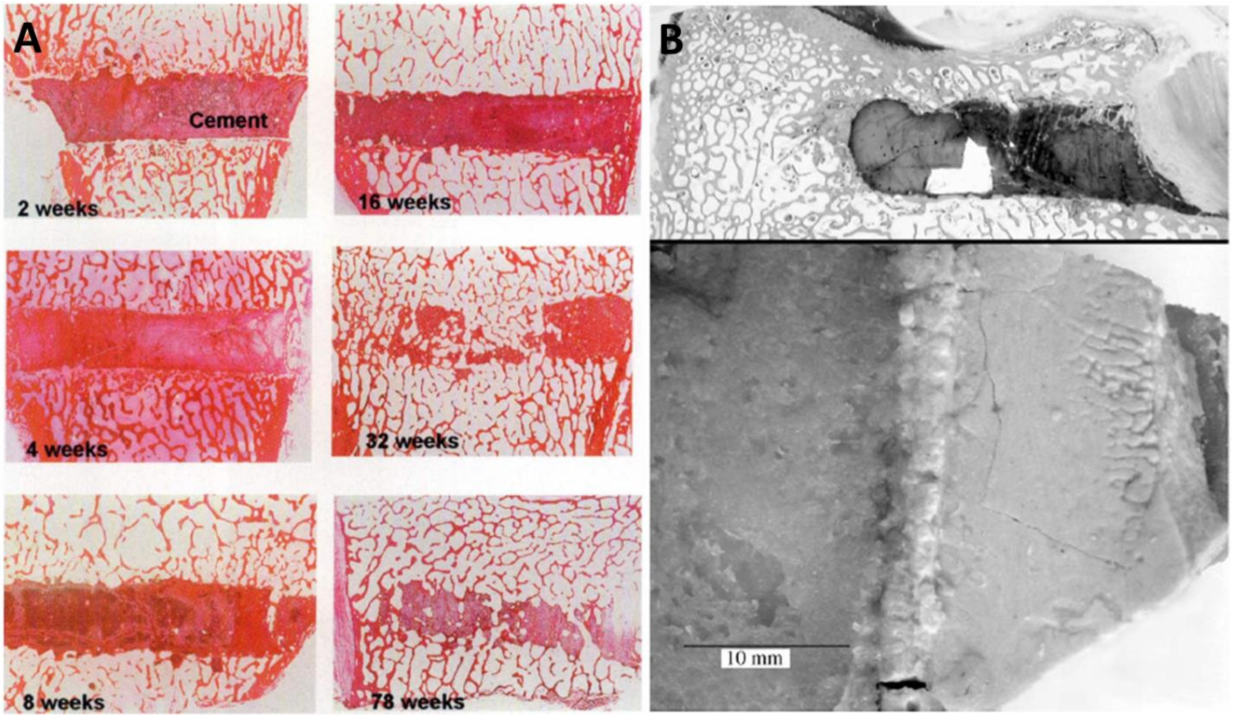

Figure 2.1 CPCs gradually remodeled in canine tibia metaphyseal defects but are mechanically unstable in highly loaded defects in ovine. (A) representative sections of canine tibia metaphyseal defects (coronal view) at 2, 4, 8, 16, 32, and 78 weeks. Reprinted from Elizabeth Frankenburg, Steven Goldstein, Thomas Bauer, et al, Biomechanical and Histological Evaluation of a Calcium Phosphate Cement*, Journal of Bone & Joint Surgery, 80, 8, Page 1116 [36] (B) sagittal section through ovine tibia metaphyseal defect (top) showing cracks of CPCs under loading, and transversal view of the defect from an *ex vivo* model (bottom) that looked very similar to the one observed in the *in vivo* study. Reprinted from Journal of Materials Science: Materials in Medicine, Mechanical Characterization of a Bone Defect Model Filled with Ceramic Cements, 15, 2004, Page 1069, A. Gisep, et al., with permission of Springer. [38]

Polymeric biocomposites

In general, ceramic materials have high compressive strength but low fracture toughness and poor mechanical reliability, which put them at a disadvantage as grafting materials for bone tissue engineering despite of their excellent biological properties. Polymers reduce the brittleness of ceramics and they can be easily fabricated into specific shapes and structures, but in general they lack bioactivity and are too flexible and weak to meet the mechanical requirements for bone tissue engineering. The combination of polymers with ceramics is a promising approach to develop composites with tailored physical and biological properties.[39]

Although reinforcement of polymer materials with particulate ceramic phase is considered a common strategy to improve the biological and mechanical properties of polymers to meet the requirements for bone tissue engineering, the addition of ceramics to polymers does not generally increase the strength of the composite compared to that of the monolithic polymer.[9] Findings from previous studies show that the addition of HA does not increase the mechanical strength of the resulting composites.[40-44] In HA reinforced polyetherketoneketone (PEKK) composites, elastic modulus increased initially from 0 to 20 vol% HA, but subsequently decreased from 20-40 vol% HA. The yield strength of composites loaded with 40 vol% HA was lower than that of composites loaded with 20 vol% HA and PEKK alone.[42] Another study revealed the strength of PEEK/calcium silicate composites decreased with increasing calcium silicate loading.[45] This behavior results from decreased interaction between the ceramic particles and the polymer matrix.[46] At high loadings, HA particles act as “flaws” in the polymer matrix due to poor interfacial bonding.[47] Surface grafting L-lactic acid oligomers of HA (op-HA) increased bending and compressive strength of op-HA/PLGA composites at low op-HA loadings (20 wt%) compared to non-grafted HA/PLGA composites. However, at higher op-HA loadings, the mechanical properties followed similar trend of decreasing bending and compressive strength.[43] Thus, while incorporation of HA in polymeric biocomposites may enhance biological properties of polymers, it does not seem to have a positive effect on mechanical properties of the biocomposites. One approach to improve the mechanical properties of the composites is to create nanoscale features by nanotechnology, which is reviewed in the following “Nanotechnologies and nanomaterials in bone tissue engineering” section.

Polyurethanes for bone tissue engineering

Polyurethanes (PURs[48]) have been incorporated in a wide variety of medical devices since the 1960s due to their toughness, durability, biocompatibility and improved biostability. In recent years, biodegradable polyurethanes have raised increased interest for use as tissue engineering scaffolds as well as drug delivery systems. PURs are synthesized by reacting isocyanates with hydroxyl and amino-functional molecules, which yields urethane linkages and urea linkages, respectively. A variety of PUR materials can be prepared using PUR chemistry, including segmented elastomers, adhesives, flexible foams and rigid networks, among which two-component rigid networks have the ability to be prepared by reactive liquid molding of two liquid reactants and set *in situ* to form a solid mass, thus are suitable for injection of bone cements.

Two-component PUR rigid networks are synthesized by reaction of either a viscous isocyanate or an isocyanate-terminated prepolymer with viscous active hydrogen components, such as polyamines, water and polyols. Polyols are viscous liquids with hydroxyl end groups and a backbone of polyether, polyester, or polycarbonate, etc. With at least one of the reactants having functionality >2, the resulting polymer is a crosslinked network formed *in situ* with tough, elastomeric mechanical properties. Among numerous sources for isocyanates to formulate PUR networks, PURs prepared from lysine-derived polyisocyanates, including lysine methyl ester diisocyanate (LDI) and lysine triisocyanate (LTI), induce minimal inflammatory response *in vivo*, support cellular infiltration and new bone formation, and degrade into noncytotoxic decomposition products *in vitro* and *in vivo*.[49-58] These findings highlight the potential of PUR networks synthesized from lysine-derived polyisocyanates for bone tissue engineering.

To enhance the osteoconductivity and mechanical properties of the PURs, calcium phosphate particles, allograft bone particles, or demineralized bone matrix are often incorporated with lysine-derived PURs to prepare grafts for bone regeneration. A study investigating injectable PUR systems synthesized by reaction of pentaerythritol-LDI prepolymer, DL-lactic acid and glycolic acid polyols and incorporation of β-TCP particles (10 μm) showed that the polymers had suitable properties for orthopaedic applications, including compressive strength comparable to that of cortical bone and *in vitro* degradation through hydrolysis of urethane and urea groups. When implanted in sheep femoral condyle defects, the material had no adverse tissue reaction, and evidence of new bone formation, polymer degradation was observed with increased implant time for up to 6 months.[59] However, in this study, the remodeling rate of the implant scaled with the rate of polymer degradation due to relatively low volume fraction and small particle size of the β-TCP. Recent study has highlighted the importance of balancing the rates of new bone formation and implant degradation to promote complete healing.[60] Various approaches have been utilized to achieve this goal. In a recent study, injectable and biodegradable allograft/LTI-PUR composites with tunable mechanical properties, degradation rates and setting and working times were developed by changing the porosity and catalyst amount.[61] In another study, recombinant human bone morphogenetic protein-2 (rhBMP-2), which is a growth factor that stimulates proliferation and differentiation of osteoprogenitor cells, was incorporated into allograft/LTI-PUR composites. Incorporation of rhBMP-2 increased the rate of new bone formation and altered the degradation mechanism of PUR network to match the rate of new bone formation, resulting in more extensive healing.[60] Recently, poly(thioketal urethane) networks that are hydrolytically stable and degrade in response to reactive oxygen species secreted by cells associated with bone remodeling have been developed, offering a new approach for the design of cell-degradable bone grafts.[62]

Two-component polyurethane rigid networks are injectable and settable *in situ* without adverse tissue reaction, exhibit highly tunable mechanical properties and degradation rates, and support cellular infiltration and new bone formation. These properties underscore the potential of two-component polyurethane rigid networks as bone grafting materials for bone tissue engineering.

Nanotechnologies and nanomaterials in bone tissue engineering

Conventional materials for bone tissue engineering cannot satisfy the high performance demands necessary for today's patient and still require improvement. Recent discoveries have highlighted that nanotechnologies improve properties of materials used for bone tissue engineering. Nanotechnologies have been used in a wide range of materials, including metals, ceramics, polymers and composites. In these materials, either nanostructured surface features or constituent nanomaterials with at least one dimension from 1 to 100 nm have been implemented. Due to these nanoscale features, nanomaterials show superior properties compared to their conventional counterparts. Specifically, the nanoscale features of nanomaterials directly interact with cells, stimulating cell growth as well as guiding tissue regeneration. In addition to dimension similarity to structure of native bone tissue, nanomaterials also exhibit unique surface properties due to significantly increased surface area and roughness compared to conventional or micron structured materials. The surface properties of nanomaterials mediate the adsorption of proteins, such as fibronectin, vitronectin and laminin, which further regulates cell attachment and behavior on the materials (**Figure 2.2**).[63] Furthermore, cell favorable surface properties of nanomaterials promote specific protein interactions and more efficiently stimulate new bone growth compared to conventional materials.[64-66] Since bone is a natural nanocomposite consists of inorganic (bone apatite) and organic (mainly collagen) components, ceramic, polymeric materials and composites have been studied for bone tissue engineering. [1]

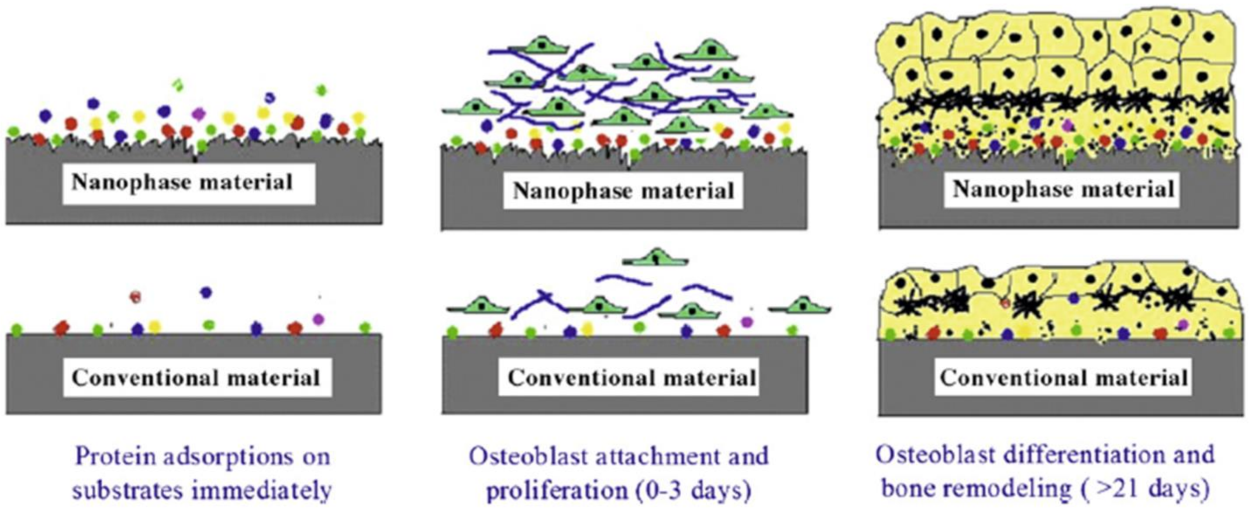

Figure 2.2 Schematic illustration of the mechanism by which nanomaterials may be superior to conventional materials for bone regeneration. The bioactive surfaces of nanomaterials mimic those of natural bones to promote greater amounts of protein adsorption and efficiently stimulate more new bone formation than conventional materials. Reprinted from Nano Today, 4, Lijie Zhang and Thomas J. Webster, Nanotechnology and Nanomaterials: Promises for Improved Tissue Regeneration, Page No. 68, Copyright (2009), with permission from Elsevier. [67]

Nanophase Ceramics

Conventional ceramics have long been known to have good biocompatibility and osteoconductivity. However, there are still many difficulties in their clinical applications because of the natural brittleness of ceramics and insufficient prolonged bonding to the juxtaposed bone. Therefore, novel ceramic materials that promote and sustain osseointegration with host bone is necessary.[68] An *in vitro* study reported significantly higher osteoblast adhesion on nanophase alumina and titania substrates compared to micron-sized counterparts.[69] Since this trend was observed for both alumina and titania, researchers implied that the enhanced osteoblast adhesion was dependent only on the surface topography and roughness. Enhanced osteoblast functions were also observed on nanophase alumina, titania and HA, indicating the unique surface properties of nanophase ceramics enhance bonding of implants to juxtaposed bone.[70]

Among the nanoceramics used for bone tissue engineering, nanocrystalline hydroxyapatite (nHA) is extensively studied due to its composition similarity to native bone apatite and ability to promote mineralization. *In vitro* studies reported that osteoblast adhesion, proliferation, alkaline phosphatase activity and deposition of calcium-containing mineral were significantly greater on nHA compared to conventional HA.[65, 70] In addition, enhanced osteoclast-like cell functions were also observed for nHA compared to conventional HA, including the synthesis of tartrate-resistant acid phosphatase (TRAP) and resorption.[71]

Examination of the underlying mechanism reveals that the surface topography of nanophase ceramics, specifically grain size, leads to highest vitronectin adsorption (key protein for osteoblast adhesion), which contributes to enhanced adhesion and function of osteoblasts.[65]

Nanostructured Polymers

Similar to ceramics, studies have revealed that nanophase polymers promote enhanced adsorption and conformation of proteins that regulate osteoblast functions. PLGA casts of nanophase carbon fibers showed increased osteoblast adhesion compared to PLGA casts of conventional carbon fibers due to the high degree of nano-scale surface roughness.[72] Since adsorption of proteins important for osteoblast adhesion is known to promote osteoblast function, it is envisioned that in future, specific nano-scale surface features could be engineered through nanotechnology that generates specific surface energy required to promote adsorption of select protein for mediating adhesion and functions of certain cell type.[68]

Ceramic/polymer nanocomposites

Ceramic/polymer nanocomposites combine the advantages of both types of materials and better mimic the constituents of natural bone tissue.[46, 73-75] A nHA/collagen composite with composition and microstructure both mimicking the natural bone provided a microenvironment resembling that seen *in* *vivo*, which promoted new bone matrix deposition. Moreover, cells within the composite acquired a 3D polygonal shape.[76] Bone cell function has also been reported to be enhanced on ceramic/polymer nanocomposites due to cell interaction with nanophase ceramic and nanophase polymer collectively compared to individually. Alkaline phosphatase activity and calcium deposition by osteoblasts were significantly enhanced on PLA/calcium metaphosphate composites compared to PLA alone.[77] Nanophase ceramic/polymer composites also promote osteoblast adhesion and functions compared to conventional composites. An *in vitro* study revealed that osteoblast adhesion, alkaline phosphatase synthesis and calcium deposition was enhanced on PLGA/nanophase titania composites compared to PLGA/conventional grain size titania composites with greater weight percentage of titania.[78] 3D nanoparticulate hydroxyapatite/poly (L-lactic acid) (NHAP/PLLA) scaffolds had significantly higher protein adsorption and enhanced osteoblast functions compared to micron particulate hydroxyapatite/poly (L-lactic acid) (MHAP/PLLA) scaffolds.[79]

Another advantage of ceramic/polymer nanocomposites over conventional composites is improved mechanical properties. Nanocomposites with nanometer grain size have greater mechanical properties than conventional composites with micron grain size.[80] Nanoceramic/PLA composites with nanophase (<100 nm) alumina, titania and HA showed significantly greater bending moduli than those of conventional composites with coarser grained ceramics.[80] Specifically, nanophase titania/PLA (50/50 weight ratio) composites had bending modulus of 1960±250 MPa, which is comparable to that of trabecular bone, while the bending modulus of plain PLA and conventional micron size titania/PLA composites with the same weight ratio were 60±3 and 870±30 MPa, respectively.[80]

A common problem associated with nanocomposites is aggregation of ceramic nanoparticles in polymer matrix. This problem can be solved with sonication or surface grafting organic molecules to ceramic nanoparticles. Better dispersion of ceramic nanoparticles in the polymer phase results in enhanced cellular activity (attachment, proliferation and differentiation) as well as improved mechanical properties of ceramic/polymer nanocomposites. [73, 78, 81-88]

References

1. Wang, M., *Developing bioactive composite materials for tissue replacement.* Biomaterials, 2003. **24**(13): p. 2133-2151.
2. Williams, D., *Chapter 9 - Biocompatibility*, in *Tissue Engineering*. 2008, Academic Press: Burlington. p. 255-278.
3. Hing, K.A., *Bioceramic bone graft substitutes: Influence of porosity and chemistry.* International Journal of Applied Ceramic Technology, 2005. **2**(3): p. 184-199.
4. Suchanek, W. and M. Yoshimura, *Processing and properties of hydroxyapatite-based biomaterials for use as hard tissue replacement implants.* Journal of Materials Research, 1998. **13**(1): p. 94-117.
5. Liu, D.M., *Influence of porosity and pore size on the compressive strength of porous hydroxyapatite ceramic.* Ceramics International, 1997. **23**(2): p. 135-139.
6. Saiz, E., et al., *Preparation of porous hydroxyapatite scaffolds.* Materials Science & Engineering C-Biomimetic and Supramolecular Systems, 2007. **27**(3): p. 546-550.
7. Barrère, F., et al., *Chapter 8 - Degradation of bioceramics*, in *Tissue Engineering*. 2008, Academic Press: Burlington. p. 223-254.
8. Ducheyne, P., S. Radin, and L. King, *The Effect of Calcium-Phosphate Ceramic Composition and Structure on in vitro Behavior .1. Dissolution.* Journal of Biomedical Materials Research, 1993. **27**(1): p. 25-34.
9. Johnson, A.J.W. and B.A. Herschler, *A review of the mechanical behavior of CaP and CaP/polymer composites for applications in bone replacement and repair.* Acta Biomaterialia, 2011. **7**(1): p. 16-30.
10. Logeart-Avramoglou, D., et al., *Engineering bone: challenges and obstacles.* Journal of Cellular and Molecular Medicine, 2005. **9**(1): p. 72-84.
11. Vastel, L., et al., *Effect of different sterilization processing methods on the mechanical properties of human cancellous bone allografts.* Biomaterials, 2004. **25**(11): p. 2105-2110.
12. Palmer, S.H., C. Gibbons, and N.A. Athanasou, *The pathology of bone allograft.* Journal of Bone and Joint Surgery-British Volume, 1999. **81B**(2): p. 333-335.
13. Vaishya, R., M. Chauhan, and A. Vaish, *Bone cement.* J Clin Orthop Trauma, 2013. **4**(4): p. 157-63.
14. Kuehn, K.-D., *Bone Cements*. 2000, Berlin: Springer.
15. ISO, *International Standard 5833*, in *Implants for Surgery - Arylic Resin Cements*. 2002.
16. Jasty, M., et al., *The Initiation of Failure in Cemented Femoral Components of Hip Arthroplasties.* Journal of Bone and Joint Surgery-British Volume, 1991. **73**(4): p. 551-558.
17. Berry, D.J., et al., *Twenty-five-year survivorship of two thousand consecutive primary Charnley total hip replacements - Factors affecting survivorship of acetabular and femoral components.* Journal of Bone and Joint Surgery-American Volume, 2002. **84A**(2): p. 171-177.
18. Bettencourt, A., et al., *Surface studies on acrylic bone cement.* International Journal of Pharmaceutics, 2004. **278**(1): p. 181-186.
19. Aamodt, A., et al., *Documentation of hip prostheses used in Norway - A critical review of the literature from 1996-2000.* Acta Orthopaedica Scandinavica, 2004. **75**(6): p. 663-676.
20. Savarino, L., et al., *Microstructural Investigation of Bone-Cement Interface.* Journal of Biomedical Materials Research, 1995. **29**(6): p. 701-705.
21. Goldring, S.R., et al., *Formation of a Synovial-Like Membrane at the Bone-Cement Interface - Its Role in Bone-Resorption and Implant Loosening after Total Hip-Replacement.* Arthritis and Rheumatism, 1986. **29**(7): p. 836-842.
22. Vaishya, R., M. Chauhan, and A. Vaish, *Bone cement.* Journal of Clinical Orthopaedics and Trauma, 2013. **4**(4): p. 157-163.

23. Verne, E., et al., *Composite bone cements loaded with a bioactive and ferrimagnetic glass-ceramic: Leaching, bioactivity and cytocompatibility.* Materials Science & Engineering C-Materials for Biological Applications, 2015. **53**: p. 95-103.
24. Tihan, T.G., et al., *Effect of hydrophilic-hydrophobic balance on biocompatibility of poly(methyl methacrylate) (PMMA)-hydroxyapatite (HA) composites.* Materials Chemistry and Physics, 2009. **118**(2-3): p. 265-269.
25. Dall'Oca, C., et al., *The biocompatibility of bone cements: progress in methodological approach.* European Journal of Histochemistry, 2017. **61**(2): p. 79-89.
26. Sundfeldt, M., et al., *Does sodium fluoride in bone cement affect implant fixation? Part I: Bone tissue response, implant fixation and histology in nine rabbits.* Journal of Materials Science-Materials in Medicine, 2002. **13**(11): p. 1037-1043.
27. Davies, J.E. and T. Matsuda, *Extracellular-Matrix Production by Osteoblasts on Bioactive Substrata Invitro.* Scanning Microscopy, 1988. **2**(3): p. 1445-1452.
28. Sautier, J.M., J.R. Nefussi, and N. Forest, *Ultrastructural-Study of Bone-Formation on Synthetic Hydroxyapatite in Osteoblast Cultures.* Cells and Materials, 1991. **1**(3): p. 209-217.
29. Matsuda, T. and J.E. Davies, *the Invitro Response of Osteoblasts to Bioactive Glass.* Biomaterials, 1987. **8**(4): p. 275-284.
30. Bohner, M., *Calcium orthophosphates in medicine: from ceramics to calcium phosphate cements.* Injury-International Journal of the Care of the Injured, 2000. **31**: p. S37-S47.
31. Osborn, J.F. and H. Newesely, *The Material Science of Calcium-Phosphate Ceramics.* Biomaterials, 1980. **1**(2): p. 108-111.
32. Gauthier, O., et al., *Macroporous biphasic calcium phosphate ceramics versus injectable bone substitute: a comparative study 3 and 8 weeks after implantation in rabbit bone.* Journal of Materials Science-Materials in Medicine, 2001. **12**(5): p. 385-390.
33. Degroot, K., *Clinical-Applications of Calcium-Phosphate Biomaterials - a Review.* Ceramics International, 1993. **19**(5): p. 363-366.
34. Zhang, J.T., et al., *Calcium phosphate cements for bone substitution: Chemistry, handling and mechanical properties.* Acta Biomaterialia, 2014. **10**(3): p. 1035-1049.
35. Xia, Z.D., et al., *In vitro biodegradation of three brushite calcium phosphate cements by a macrophage cell-line.* Biomaterials, 2006. **27**(26): p. 4557-4565.
36. Frankenburg, E.P., et al., *Biomechanical and histological evaluation of a calcium phosphate cement.* Journal of Bone and Joint Surgery-American Volume, 1998. **80A**(8): p. 1112-1124.
37. Gisep, A., et al., *Resorption patterns of calcium-phosphate cements in bone.* Journal of Biomedical Materials Research Part A, 2003. **66A**(3): p. 532-540.
38. Gisep, A., et al., *Mechanical characterisation of a bone defect model filled with ceramic cements.* Journal of Materials Science-Materials in Medicine, 2004. **15**(10): p. 1065-1071.
39. Boccaccini, A.R. and J.J. Blaker, *Bioactive composite materials for tissue engineering scaffolds.* Expert Review of Medical Devices, 2005. **2**(3): p. 303-317.
40. Shikinami, Y. and M. Okuno, *Bioresorbable devices made of forged composites of hydroxyapatite (HA) particles and poly-L-lactide (PLLA): Part I. Basic characteristics.* Biomaterials, 1999. **20**(9): p. 859-877.
41. Wong, K.L., et al., *Mechanical properties and in vitro response of strontium-containing hydroxyapatite/polyetheretherketone composites.* Biomaterials, 2009. **30**(23-24): p. 3810-3817.
42. Converse, G.L., T.L. Conrad, and R.K. Roeder, *Mechanical properties of hydroxyapatite whisker reinforced polyetherketoneketone composite scaffolds.* J Mech Behav Biomed Mater, 2009. **2**(6): p. 627-35.
43. Cui, Y., et al., *The nanocomposite scaffold of poly(lactide-co-glycolide) and hydroxyapatite surface-grafted with L-lactic acid oligomer for bone repair.* Acta Biomaterialia, 2009. **5**(7): p. 2680-2692.

44. Cai, X., et al., *Preparation and characterization of homogeneous chitosan-polylactic acid/hydroxyapatite nanocomposite for bone tissue engineering and evaluation of its mechanical properties.* Acta Biomaterialia, 2009. **5**(7): p. 2693-2703.
45. Kim, I.Y., et al., *Bioactive Composites Consisting of PEEK and Calcium Silicate Powders.* Journal of Biomaterials Applications, 2009. **24**(2): p. 105-118.
46. Thomson, R.C., et al., *Hydroxyapatite fiber reinforced poly(alpha-hydroxy ester) foams for bone regeneration.* Biomaterials, 1998. **19**(21): p. 1935-1943.
47. Roeder, R.K., et al., *Hydroxyapatite-reinforced polymer biocomposites for synthetic bone substitutes.* Jom, 2008. **60**(3): p. 38-45.
48. Hinrichsen, G., *Polyurethane handbook (2nd ed.). Edited by G. Oertel, Hanser Publishers, Munich 1993, 770 pp., DM 358, ISBN 3-446-17198-3.* Acta Polymerica, 1994. **45**(5): p. 398-398.
49. Bennett, S., et al., *Initial biocompatibility studies of a novel degradable polymeric bone substitute that hardens in situ.* Bone, 1996. **19**(1): p. S101-S107.
50. Adolph, E.J., et al., *Injectable polyurethane composite scaffolds delay wound contraction and support cellular infiltration and remodeling in rat excisional wounds.* Journal of Biomedical Materials Research Part A, 2012. **100A**(2): p. 450-461.
51. Page, J.M., et al., *Biocompatibility and chemical reaction kinetics of injectable, settable polyurethane/allograft bone biocomposites.* Acta Biomaterialia, 2012. **8**(12): p. 4405-4416.
52. Borkenhagen, M., et al., *In vivo performance of a new biodegradable polyester urethane system used as a nerve guidance channel.* Biomaterials, 1998. **19**(23): p. 2155-2165.
53. Guelcher, S., et al., *Synthesis, In vitro degradation, and mechanical properties of two-component poly(ester urethane)urea scaffolds: Effects of water and polyol composition.* Tissue Engineering, 2007. **13**(9): p. 2321-2333.
54. Guelcher, S.A., et al., *Synthesis and in vitro biocompatibility of injectable polyurethane foam scaffolds.* Tissue Engineering, 2006. **12**(5): p. 1247-1259.
55. Zhang, J.Y., et al., *A new peptide-based urethane polymer: synthesis, biodegradation, and potential to support cell growth in vitro.* Biomaterials, 2000. **21**(12): p. 1247-1258.
56. Zhang, J.Y., et al., *Synthesis, biodegradability, and biocompatibility of lysine diisocyanate-glucose polymers.* Tissue Engineering, 2002. **8**(5): p. 771-785.
57. Elliott, S., et al., *Identification of biodegradation products formed by L-phenylalanine based segmented polyurethaneureas.* Journal of Biomaterials Science-Polymer Edition, 2002. **13**(6): p. 691-711.
58. Saad, B., et al., *Development of degradable polyesterurethanes for medical applications: In vitro and in vivo evaluations.* Journal of Biomedical Materials Research, 1997. **36**(1): p. 65-74.
59. Adhikari, R., et al., *Biodegradable injectable polyurethanes: Synthesis and evaluation for orthopaedic applications.* Biomaterials, 2008. **29**(28): p. 3762-3770.
60. Dumas, J.E., et al., *Balancing the Rates of New Bone Formation and Polymer Degradation Enhances Healing of Weight-Bearing Allograft/Polyurethane Composites in Rabbit Femoral Defects.* Tissue Engineering Part A, 2014. **20**(1-2): p. 115-129.
61. Dumas, J.E., et al., *Synthesis and Characterization of an Injectable Allograft Bone/Polymer Composite Bone Void Filler with Tunable Mechanical Properties.* Tissue Engineering Part A, 2010. **16**(8): p. 2505-2518.
62. McEnery, M.A.P., et al., *Oxidatively degradable poly(thioketal urethane)/ceramic composite bone cements with bone-like strength.* Rsc Advances, 2016. **6**(111): p. 109414-109424.
63. Webster, T.J., *Nanophase ceramics: The future orthopedic and dental implant material*, in *Nanostructured Materials*, J.Y. Ying, Editor. 2001, Academy Press: New York. p. 125-166.
64. Degasne, I., et al., *Effects of roughness, fibronectin and vitronectin on attachment, spreading, and proliferation of human osteoblast-like cells (Saos-2) on titanium surfaces.* Calcified Tissue International, 1999. **64**(6): p. 499-507.
65. Webster, T.J., et al., *Specific proteins mediate enhanced osteoblast adhesion on nanophase ceramics.* Journal of Biomedical Materials Research, 2000. **51**(3): p. 475-483.

66. Webster, T.J., et al., *Mechanisms of enhanced osteoblast adhesion on nanophase alumina involve vitronectin.* Tissue Engineering, 2001. **7**(3): p. 291-301.
67. Zhang, L.J. and T.J. Webster, *Nanotechnology and nanomaterials: Promises for improved tissue regeneration.* Nano Today, 2009. **4**(1): p. 66-80.
68. Tran, N. and T.J. Webster, *Nanotechnology for bone materials.* Wiley Interdisciplinary Reviews-Nanomedicine and Nanobiotechnology, 2009. **1**(3): p. 336-351.
69. Webster, T.J., R.W. Siegel, and R. Bizios, *Osteoblast adhesion on nanophase ceramics.* Biomaterials, 1999. **20**(13): p. 1221-1227.
70. Webster, T.J., et al., *Enhanced functions of osteoblasts on nanophase ceramics.* Biomaterials, 2000. **21**(17): p. 1803-1810.
71. Webster, T.J., et al., *Enhanced osteoclast-like cell functions on nanophase ceramics.* Biomaterials, 2001. **22**(11): p. 1327-1333.
72. Price, R.L., et al., *Nanometer surface roughness increases select osteoblast adhesion on carbon nanofiber compacts.* Journal of Biomedical Materials Research Part A, 2004. **70A**(1): p. 129-138.
73. Liu, H.N., E.B. Slamovich, and T.J. Webster, *Increased osteoblast functions on nanophase titania dispersed in poly-lactic-co-glycolic acid composites.* Nanotechnology, 2005. **16**(7): p. S601-S608.
74. Boccaccini, A.R. and V. Maquet, *Bioresorbable and bioactive polymer/Bioglass (R) composites with tailored pore structure for tissue engineering applications.* Composites Science and Technology, 2003. **63**(16): p. 2417-2429.
75. Hutmacher, D.W., *Scaffolds in tissue engineering bone and cartilage.* Biomaterials, 2000. **21**(24): p. 2529-2543.
76. Du, C., et al., *Three-dimensional nano-HAp/collagen matrix loading with osteogenic cells in organ culture.* Journal of Biomedical Materials Research, 1999. **44**(4): p. 407-415.
77. Jung, Y., et al., *A poly(lactic acid)/calcium metaphosphate composite for bone tissue engineering.* Biomaterials, 2005. **26**(32): p. 6314-6322.
78. Webster, T.J. and T.A. Smith, *Increased osteoblast function on PLGA composites containing nanophase titania.* Journal of Biomedical Materials Research Part A, 2005. **74A**(4): p. 677-686.
79. Wei, G.B. and P.X. Ma, *Structure and properties of nano-hydroxyapatite/polymer composite scaffolds for bone tissue engineering.* Biomaterials, 2004. **25**(19): p. 4749-4757.
80. McManus, A.J., et al., *Evaluation of cytocompatibility and bending modulus of nanoceramic/polymer composites.* Journal of Biomedical Materials Research Part A, 2005. **72A**(1): p. 98-106.
81. Wang, Z.L., et al., *Enhanced in Vitro Mineralization and in Vivo Osteogenesis of Composite Scaffolds through Controlled Surface Grafting of L-Lactic Acid Oligomer on Nanohydroxyapatite.* Biomacromolecules, 2016. **17**(3): p. 818-829.
82. Lee, H.J., et al., *The effect of surface-modified nano-hydroxyapatite on biocompatibility of poly(epsilon-caprolactone)/hydroxyapatite nanocomposites.* European Polymer Journal, 2007. **43**(5): p. 1602-1608.
83. Jiang, L.Y., et al., *Effect of l-lysine-assisted surface grafting for nano-hydroxyapatite on mechanical properties and invitro bioactivity of poly(lactic acid-co-glycolic acid).* Journal of Biomaterials Applications, 2016. **30**(6): p. 750-758.
84. Dong, S.J., et al., *Preparation, Surface Properties and Biological Activity of the Composite of Poly (lactide-co-glycolide) and Bioglass Nanoparticles Surface Grafted with Poly(L-lactide).* Chemical Journal of Chinese Universities-Chinese, 2009. **30**(5): p. 1018-1023.
85. Fan, R.R., et al., *Preparation and properties of g-TTCP/PBS nanocomposites and its in vitro biocompatibility assay.* International Journal of Biological Macromolecules, 2013. **59**: p. 227-234.
86. Jiang, L.Y., et al., *Effect of n-HA with different surface-modified on the properties of n-HA/PLGA composite.* Applied Surface Science, 2012. **259**: p. 72-78.

87. Jiang, L.X., et al., *Effect of a new surface-grafting method for nano-hydroxyapatite on the dispersion and the mechanical enhancement for poly(lactide-co-glycolide)*. Express Polymer Letters, 2014. **8**(2): p. 133-141.
88. Qiu, X.Y., et al., *Surface-modified hydroxyapatite linked by L-lactic acid oligomer in the absence of catalyst*. Journal of Polymer Science Part a-Polymer Chemistry, 2005. **43**(21): p. 5177-5185.

CHAPTER 3 - RESORBABLE NANOCOMPOSITES WITH BONE-LIKE STRENGTH AND ENHANCED CELLULAR ACTIVITY

Introduction

Bone substitutes utilized in the treatment of fractures at weight-bearing sites, such as intra-articular joints, are subjected to repetitive, dynamic physiological loading from daily activities.[1] An ideal bone cement rapidly sets after injection, provides bone-like strength, stimulates osteogenic differentiation of endogenous cells, and resorbs at a rate aligned with patient biology. Bone substitutes that remodel to form new bone while maintaining load-bearing capacity would significantly improve patient care.[2] However, biomaterials that provide both functionality and load-bearing capability are currently not available. Poly(methyl methacrylate) (PMMA) cement is indicated for use in arthroplasty procedures of the hip, knee, and other weight-bearing joints due to its high strength (≥ 70 MPa).[3, 4] However, PMMA is non-resorbable and does not integrate with host bone, resulting in device loosening and long-term failure.[5-9]

Injectable and settable calcium phosphate cements (CPCs) showed promise in early weight-bearing applications due to their bone-like compressive strength.[2, 10] Calcium phosphate cements (CPCs) are osteoconductive and resorbable, but their low bending strength and fatigue resistance preclude their use at weight-bearing sites.[2, 11] Biphasic CPCs reinforced with a polymeric or metallic phase exhibit enhanced mechanical properties compared to monophasic cements.[12-16] Reinforcement of CPCs with polymer or metal fibers increased bending strength to 139 MPa,[16] but there are a limited number of studies evaluating osteogenic differentiation and osteoclast-mediated resorption of these materials.

Recently, bioactive glass-polymer hybrids characterized by covalent nanoscale-interactions between the inorganic and organic phases have been reported to exhibit compressive strengths as high as 300 MPa and tunable degradation.[17-22] However, bioactive glass-polymer composites undergo uncontrolled degradation by hydrolysis, and the sol-gel approach requires solvents and elevated temperatures that preclude injection. Thus, there is a compelling need for settable bone cements that exhibit bone-like strength, stimulate osteogenic differentiation and mineralization of endogenous cells, and undergo osteoclast-mediated resorption at a rate aligned with patient biology.

Nanocrystalline (grain size < 100 nm) hydroxyapatite (nHA) enhances osteogenic differentiation, new bone formation, and osteoclast differentiation activity compared to micron-scale crystalline HA.[23-32] The reactive hydroxyl (OH) group on the surface of HA can be used to graft organic molecules, such as polyesters and polyisocyanates.[33-38] Grafting organic molecules to the surface of ceramic nanoparticles enhances their dispersion in organic polymers as well as interfacial binding between the polymer and ceramic phases, resulting in improved mechanical properties and stimulation of cell attachment, proliferation, and differentiation.[37, 39-45] However, the effects of surface grafting on mechanical and biological properties of reactive and settable nHA/polymer composite cements have not been investigated. Furthermore, studies investigating grafting of polyisocyanates to nHA have utilized solvents such as dimethyl formamide (DMF), which are cytotoxic and not suitable for injectable biomaterials.[36, 38] We have previously reported that lysine-derived poly(ester urethane)s (PEUR) undergo cell-mediated oxidative degradation.[46, 47] In this study, we grafted lysine triisocyanate (LTI) to the surface of nHA by a solvent-free process to yield a viscous prepolymer that can be further crosslinked with a polyester triol by injection through a double-syringe static mixer to form a nHA-PEUR nanocomposite cement. We investigated the effects of grafting LTI to nHA on nHA dispersion, mechanical properties, osteoblast mineralization, and osteoclast- and ROS-mediated resorption of the nHA-PEUR cements. This chapter has been published as a journal article titled “Resorbable Nanocomposites with Bone-Like Strength and Enhanced Cellular Activity” in Journal of Materials Chemistry B, 2017, 5, 4198.

Experimental

Materials

nHA particles were purchased from Sigma-Aldrich and dried at 80 °C under vacuum for 48 hours before use. LTI was supplied by Jinan Haohua Industry Co., Ltd (Jinan, China). Before use, LTI was purified by dissolving in tert-butyl methyl ether (TBME, Across-Organic) and refluxing with decolorizing carbon (Fisher Scientific) at 63°C for 22 hours. α-MEM, FBS, trypsin-EDTA and Antibiotic-Antimycotic were purchased from ThermoFisher Scientific. Mesenchymal stem cell media were purchased from PromoCell, Inc. Iron acetylacetonate (FeAA) catalyst, fibronectin, vitronectin, Alizarin Red S and 1α,25-Dihydroxyvitamin D3 were purchased from Sigma-Aldrich and used as received. The mouse MC3T3 osteoblast cell line was purchased from ATCC. Human bone marrow derived mesenchymal stem cells (hMSCs) were purchased from Extem Bioscience (San Francisco, CA). Dentin was acquired from the donation of a surrendered elephant tusk from the National Eagle and Wildlife Property Repository of the United States Department of the Interior, U.S. Fishes and Wildlife Service.

Synthesis and characterization of nHA-LTI/LTI prepolymer

nHA particles (Sigma) were mixed with LTI and FeAA (0.027 wt%) catalyst using a SpeedMixer (FlackTek, Inc, Landrum, SC) for 10 min and maintained at 50 °C for 3 h. %NCO of the resulting prepolymer was measured by titration.[48, 49] ATR-FTIR was performed using a Seagull Variable Angle Reflection Accessory (Harrick Scientific) attached to a Tensor 27 FTIR (Bruker) from 750 to 4000 cm^{-1}. The prepolymer was dissolved in dichloromethane and centrifuged to recover grafted nHA-LTI particles. XPS was performed using an Ulvac-PHI Versaprobe 5000. Particle samples were pressed into indium foil and mounted onto sample pucks before introducing them into the instrument. Monochromatic Al Kα x-rays (1486 eV), a 100-µm diameter x-ray spot, and a takeoff angle of 60^o off sample normal were used. Pass energies of 187.7 eV and 23.5 eV were utilized for the survey and high-resolution acquisitions, respectively. Charge neutralization was accomplished using 1.1 eV electrons and 10 eV Ar^+ ions. Placing the -CH_2- type bonding in the carbon 1s spectrum at 284.8 eV corrected any minor energy shifts due to charging. Relative atomic concentrations were calculated using peak areas and PHI handbook sensitivity factors.[50] nHA-LTI particles (> 200 per group) were re-dispersed in ethanol (0.1 wt%), sputter-coated, imaged by SEM (Zeiss Merlin), and measured by Image J. XRD was conducted using a Scintag XGEN-4000 X-ray diffractometer (λ = 154 nm). The peak at $2\theta = 26.04°$ was chosen for calculation of crystallite size, which corresponds to (0 0 2) Miller's plane family and shows the crystal growth along the c-axis of the HA crystalline structure.[51] Viscosity samples were loaded between 25-mm plates with 500-µm gap size on a TA AR2000ex rheometer.

Mechanical Testing

nHA-LTI and nHA nanocpmposites were cured and soaked in PBS at 37°C for 24 h. Quasi-static compression testing was conducted using an MTS 858 Bionix Servohydraulic test system (Eden Prairie, MN). Specimens were preloaded to 12 N and compressed until failure at 25 mm min^{-1}. Compressive modulus was calculated from the initial slope of the stress-strain curve, and compressive strength was determined from the maximum stress. Flexural strength and moduli were measured by 4-point bending of rectangular (36.9 mm x 7.4 mm x 3.7 mm) specimens. The support and load spans were maintained at 30.8 mm and 10.3 mm (1/3 of the support span), respectively (ASTM D6272-10).[52] Bending strength (σ_B) was calculated from the following equation:

$$\sigma_{\mathrm{B}} = FL / wd^2 \tag{3.1}$$

where F = load at fracture (N), L = support span length (mm), w = width (mm), and d = thickness (mm). Bending modulus (E_{B}) was calculated according to following equation:

$$E_{\mathrm{B}} = 0.21L^3m_0 / wd^3 \tag{3.2}$$

where m_0 = initial slope of the stress-strain curve.

Swelling

Specimens (0.56 ± 0.15 g) were incubated in methylene chloride for 24 h. Wet mass was measured immediately upon removal from the solvent. % swelling was calculated as:

$$\text{Swelling} = (M_{\mathrm{wet}} - M_{\mathrm{dry}}) / M_{\mathrm{dry}} \tag{3.3}$$

Contact angle and protein adsorption

Cured speciments were cut into chips with ~1 mm thickness and cross-sectional area compatible with a 24-well tissue culture plate. The surface of the chips was polished with a series of wet silicon carbide papers using K1000 roughness for 10 s, K1200 roughness for 10 s, and K4000 roughness for 60 s. Additionally, LTI-poly(ester-urethane) (LTI-PEUR) without nHA was prepared as a polymer control by mixing and curing LTI with poly(ε-caprolactone triol) and FeAA catalyst at the same conditions described for the nHA-PEUR composites above. The cured LTI-PEUR samples were polished using the same procedure as other samples. Water contact angle was measured using a Rame-Hart (Moutain Lakes, NJ) Model A-100 goniometer. Protein adsorption was measured by Pierce BCA kit after incubating samples in fibronectin or vitronectin solutions (5 μg ml^{-1}) at 37°C overnight.

Cell culture

MC3T3 cells were maintained in α-MEM with FBS (10%) and antibiotic-antimycotic (1%). Cells were detached at sub-confluency by trypsin EDTA (0.25%) and re-suspended ($5x10^4$ cells mL^{-1}) in complete medium and seeded on substrates pre-soaked in fibronectin solution (4 μg mL^{-1}). Cell proliferation and metabolism were measured by total protein (BCA Protein Assay Reagent, Thermo) and MTS assay (CellTiter 96® Aqueous Non-Radioactive Cell Proliferation Assay, Promega), respectively.

Mineralization

Human mesenchymal stem cells (hMSCs) were maintained in mesenchymal stem cell growth medium with antibiotic-antimycotic (1%). At sub-confluency, cells were detached and seeded on substrates pre-coated with fibronectin solution as described above.

After 3 days of culture on substrates, mesenchymal stem cell osteogenic differentiation medium was added to induce differentiation. After 7 days from induction, samples were washed with DPBS, fixed with formalin (10%), and stained with Alizarin Red S solution (2%). Acellular control substrates showed negligible Alizarin red staining. Stained cell layers were removed from the substrates and washed with distilled water before imaging under light microscopy. Mineralization was quantified by counting the %

stained area using Image J software. After imaging under light microscopy, alizarin red was extracted by SDS (5%), and absorbance at 550 nm and 405 nm was measured.

Osteoclastogenesis Assays

Dentin was cut into chips (~1 mm thick) and polished following the same prodedure described for nHA-PEUR above as a positive control with a chemical composition comparable to bone.[53, 54] MC3T3 cells were seeded on the substrates and cultured in osteoinductive medium supplemented with 1α,25-Dihydroxyvitamin D3 (10 nM) for two days before RAW 264.7 cells were added. MC3T3 and RAW cells were co-cultured in osteoinductive medium supplemented with 1α,25-Dihydroxyvitamin D3 (10 nM) for up to 28 days. At day 15, cells were washed with PBS, fixed in formalin (10%), permeabilized in Triton-X-100 (0.1%), stained with rhodamine phalloidin (Life Technologies) and DAPI, and imaged under a Zeiss LSM 710 confocal microscope. At day 28, samples were sonicated in water for 10 min, air-dried, and sputter-coated for imaging using a Zeiss Merlin SEM.

Statistical analysis

The statistical significance between experimental groups was determined by Student's *t test* or by a two-way ANOVA. Tukey's multiple comparison test was conducted as post-hoc test to determine statistical differences following ANOVA. Graphs show mean and S.D., and $p < 0.05$ was considered statistically significant.

Results

Prepolymer synthesis and characterization

To synthesize the injectable prepolymer, nHA (65 wt%) and LTI (35 wt%) were mixed with iron acetylacetonate (FeAA) catalyst (0.027 wt%) at 50°C for 3 h. The reactive mixture was initially granular (comparable to wet sand). After adding FeAA catalyst and mixing for 1 minute, the mixture transformed from a granular to a viscous dispersion of surface-grafted nHA (nHA-LTI) in LTI (referred to as the nHA-LTI/LTI prepolymer). LTI was grafted to nHA through reaction of a primary NCO group with a P-OH group on the surface of nHA (**Figure 3.1A**). To confirm the presence of grafted LTI, the %NCO of the catalyzed mixture (open black circles in **Figure 3.1B**) was measured by titration as a function of nHA concentration. Theoretical values of % NCO (filled black circles in **Figure 3.1B**) were calculated based on dilution assuming no reaction. The conversion of NCO groups to phosphate urethane groups is

$$\xi_{NCO} = (\%NCO_0 - \%NCO) / \%NCO_0 \qquad (4)$$

where $(\%NCO)_0$ and $(\%NCO)$ represent the theoretical (calculated assuming dilution) and experimental (meaured for the catalyzed mixture) NCO content, respectively. ξ_{NCO} (red line in **Figure 3.1B**) increased from 3.6 to 14.6% with increasing nHA concentration.

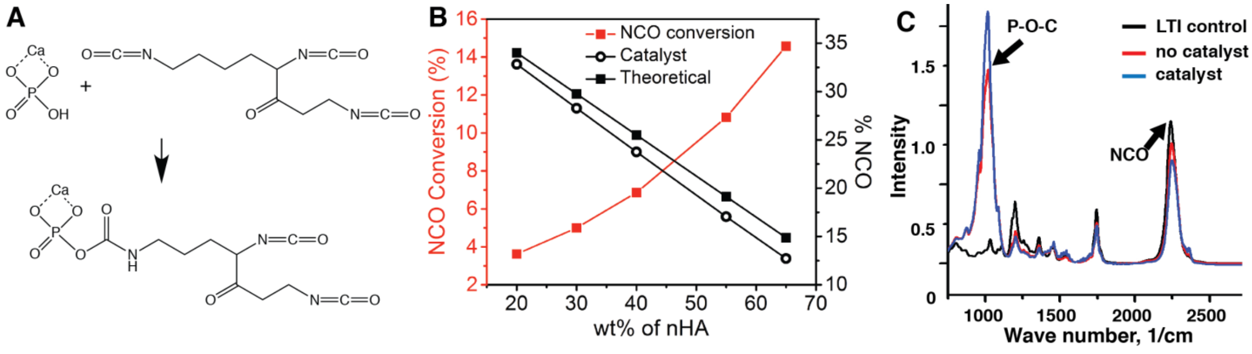

Figure 3.1 Synthesis of the nHA-LTI prepolymer. (A) Schematic of the urethane reaction between the P-OH groups on surface of nHA particles and the isocyanate groups of LTI. (B) The theoretical %NCO of the nHA/LTI mixture assuming no reaction occurred (filled black circles) was higher than the actual %NCO of the catalyzed nHA-LTI mixture (open black circles), and NCO conversion increased with nHA loading (red line). (C) FTIR spectra of LTI (black) and uncatalyzed (red) and catalyzed (blue) mixtures of nHA and LTI.

FTIR analysis of the catalyzed nHA-LTI/LTI dispersion showed a reduction in the N=C=O peak at 2260 cm^{-1} and an increase in the P-O-C peak at 1140 cm^{-1} compared to the uncatalyzed dispersion, suggesting that N=C=O groups in LTI were consumed and new P-O-C groups formed in the presence of catalyst (**Figure 3.1C**). These observations further confirm the reaction of LTI with nHA in the presence of catalyst.[38]

Surface characterization of grafted nHA

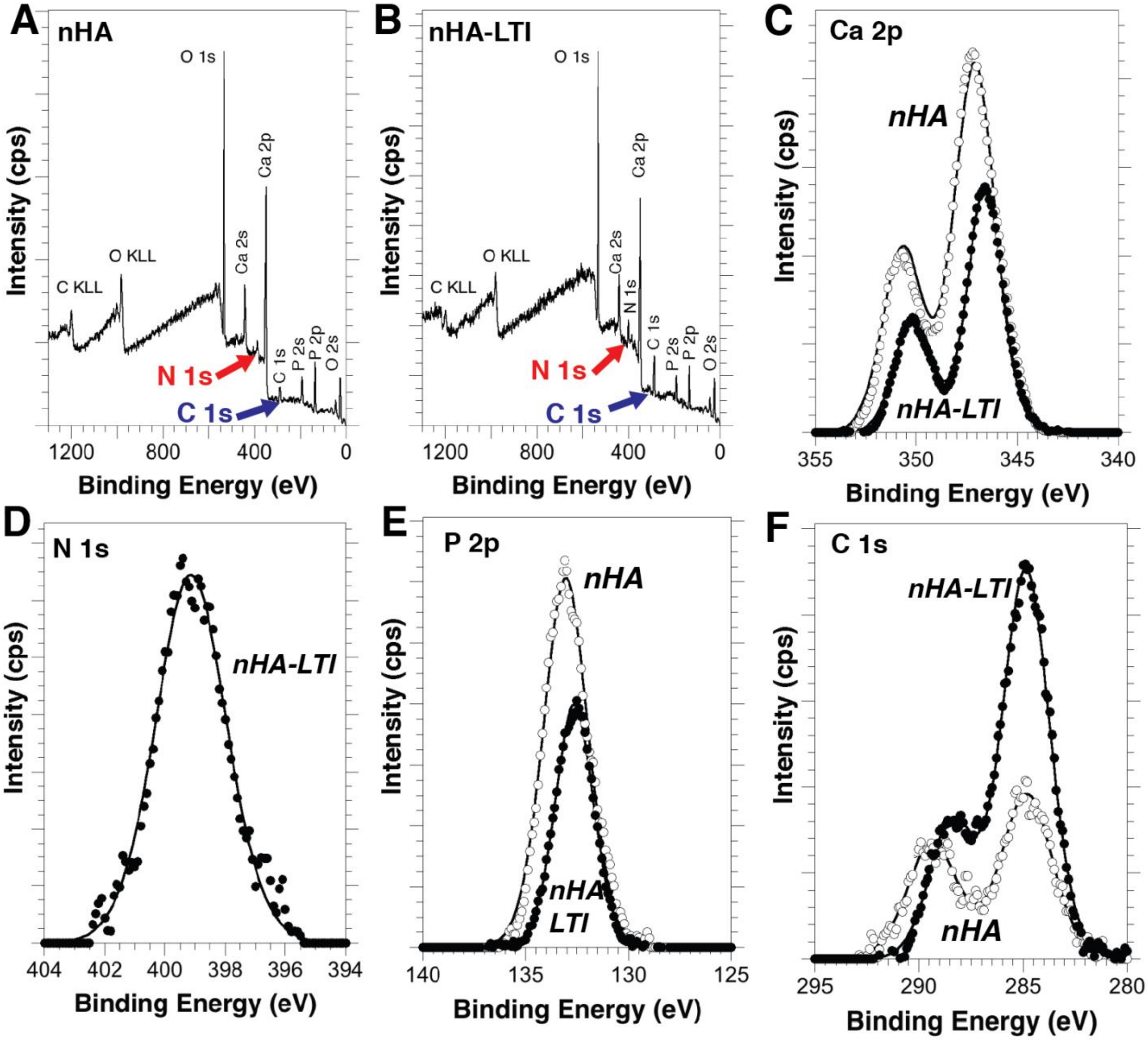

	Ca:P	C:P	N:P
nHA	**1.7**	**0.6**	**ND**
nHA-LTI	**1.7**	**2.2**	**0.6**

Figure 3.2 Surface characterization of grafted nHA particles. (A-B) XPS survey spectra of (A) nHA and (B) nHA-LTI particles recovered from the prepolymer. (C-F) XPS high-resolution spectra of (C) Ca, (D) N, (E) P, and (F) C peaks measured for nHA (open circles) and nHA-LTI (filled circles) particles.

The nHA particles grafted with LTI (nHA-LTI) were recovered from the catalyzed nHA-LTI/LTI prepolymer and their surface chemistry characterized using XPS. The increased C 1s peak (blue arrow) in the survey spectrum of the nHA-LTI particles (**Figure 3.2B**) compared to that in the survey spectrum of the nHA particles (**Figure 3.2A**), as well as the presence of the N1s peak (red arrow **Figure 3.2B**) in the nHA-LTI survey spectrum but not the nHA survey spectrum, are consistent with LTI grafting to the nHA particles. High-resolution spectra (**Figure 3.2C-F**) of the Ca 2p, P 2p, and C 1s peaks confirm differences in the chemical bonding states of these elements between the nHA and nHA-LTI samples. The binding energies of both the Ca 2p (346.5 eV) and P 2p (132.6 eV) transitions on the nHA-LTI surface are lower than the expected (and observed) binding energies of Ca 2p and P 2p electrons on the nHA surface (347.1 eV and 133.0 eV, respectively). This binding energy shift is indicative of a change in chemical bonding of these elements in the nHA particles due to LTI grafting. The carbon-oxygen type bonding evident in the C 1s spectrum from the nHA sample (**Figure 3.2F**) is typical of adventitious hydrocarbon adsorption due to atmospheric exposure and is attributed to residual chemicals from the nHA manufacturing process. The C 1s spectrum of the nHA-LTI sample contains contributions from $-CH_2-$ type bonding (284.8 eV) as well as O–C=O- type bonding (≈ 288 eV), which are consistent with the structure of grafted LTI. Quantitative analysis showed that Ca/P = 1.7 for both nHA-LTI and nHA, consistent with the stoichiometry of HA, while the C:P and N:P ratios increased after grafting (**Figure 3.2** Table). The conversion of OH groups (ξ_{OH}) is calculated from:

$$\xi_{OH} = (C:P) / (C:P)_{100\%} = (N:P) / (N:P)_{100\%} \qquad (5)$$

where $C:P_{100\%} = 5.5$ and $N:P_{100\%} = 1.5$ are the atomic ratios assuming complete reaction of the OH groups with the primary NCO groups in LTI (**Figure 3.1A**). Thus, the conversion of OH groups was 40%. At higher conversions, gelation of the nHA-LTI/LTI prepolymer was observed, which is conjectured to result from either urea formation due to water or allophonate crosslinking reactions between grafted phosphate urethane groups and LTI in the liquid phase.[55]

Effects of surface grafting on nHA size and crystallinity

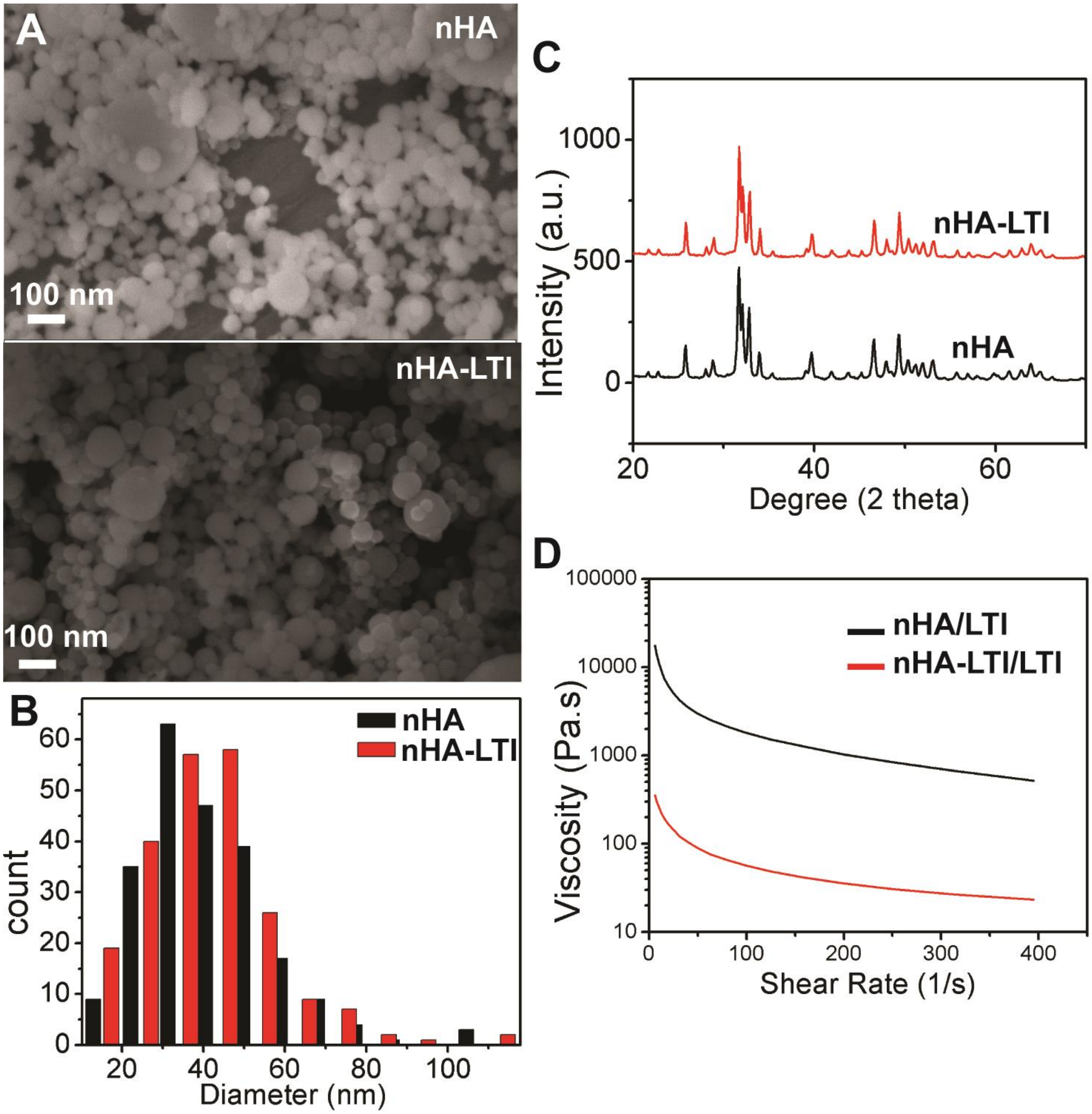

Figure 3.3 Effects of surface grafting on nHA properties. (A) SEM images and (B) particle size distribution of nHA and nHA-LTI particles measured from counts of >500 particles. (C) XRD spectra of nHA and nHA-LTI particles. (D) Viscosity of nHA-LTI/LTI prepolymer (red) was almost two orders of magnitude lower than that of the uncatalyzed nHA/LTI mixture (black).

The effects of LTI grafting on nHA particle size and crystallinity were assessed by SEM and x-ray diffraction (XRD). The particle size distribution measured from SEM images (**Figure 3.3A-B**) showed no difference in the mean size of nHA (45 ± 16 nm) and nHA-LTI (45 ± 15 nm) particles. Similarly, grafting did not alter nHA crystallinity (**Figure 3.3C**). The grain size determined from the XRD spectra using Scherrer equation was 36 nm (0 0 2 Miller's plane family) for both nHA and nHA-LTI.

Both nHA and nHA-LTI nanoparticles (65 wt%) were dispersed in LTI to prepare nHA/LTI and nHA-LTI/LTI prepolymers. The resulting dispersions were shear-thinning, as evidenced by the decrease in viscosity with increasing shear rate (**Figure 3.3D**). Furthermore, the viscosity of nHA-LTI/LTI was almost two orders of magnitude lower than that of nHA/LTI, which is consistent with the notion that grafting LTI to the nHA increases colloidal stability, resulting in a more homogeneous dispersion.[37, 39] At shear rates relevant to injectable bone cements (1 – 10 s^{-1}), the nHA-LTI/LTI prepolymer (65 wt% nHA) exhibited kinematic viscosity < 20,000 cSt, which enabled it to be injected.[2]

Effects of surface grafting on dispersion in nHA/PEUR nanocomposites

To demonstrate the injectability of the nHA-LTI nanocomposite, nHA-LTI/LTI prepolymer and PCL triol were mixed and injected through a double barrel syringe fitted with a static mixer (MedMix, **Figure 3.4A**). The NCO groups in LTI and nHA-LTI react with hydroxyl groups in the PCL triol to form crosslinked organic-inorganic hybrid polymers (**Figure 3.4B**). Dispersion of nHA and nHA-LTI in the nanocomposites was evaluated by SEM (**Figure 3.4C**). The area% of nHA-LTI aggregates was 5 times smaller than that measured for nHA (**Figure 3.4D**), which is consistent with the rheology data (**Figure 3.3D**) finding that nHA-LTI is more effectively dispersed in the reactive nanocomposite. Swelling (assessed by incubating the nanocomposites in dichloromethane for 24 h) decreased significantly with LTI grafting and increasing isocyanate index (**Figure 3.4E**), which further suggests that surface grafting enhanced dispersion and crosslinking. These findings are consistent with a recent study reporting that the colloidal stability of nHA grafted with lactic acid oligomers increased with increasing polymer concentration on the surface.[37]

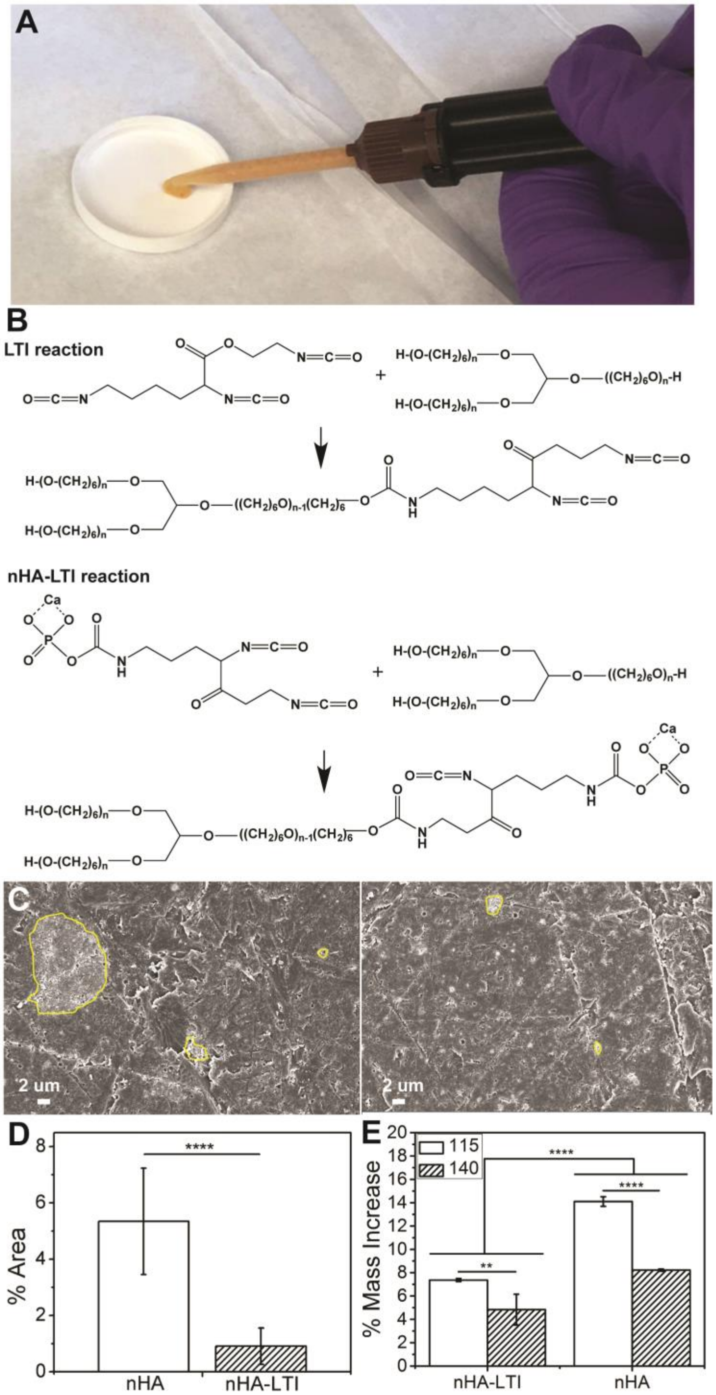

Figure 3.4 Effects of surface grafting on dispersion in nHA/PEUR composites. (A) Mixing and injection of nHA-LTI/LTI prepolymer with PCL triol in a double-barrel syringe fitted with a static mixture. (B)

Schematic illustrating the reaction between NCO groups in LTI and nHA-LTI with hydroxyl groups in poly(caprolactone) (PCL) triol to form crosslinked nanocomposites. (C) SEM images of aggregated particles (>1 µm, yellow lines) in nHA (left) and nHA-LTI (right) nanocomposites. (D) Area% of aggregates in nHA nanocomposites was 5 times larger than that measured for nHA-LTI nanocomposites. (E) Swelling of nHA and nHA-LTI nanocomposites after incubating in dichloromethane for 24 h decreased significantly with surface grafting and increasing index from 115 (white) to 140 (hatched).

Mechanical properties of nHA/PEUR composites

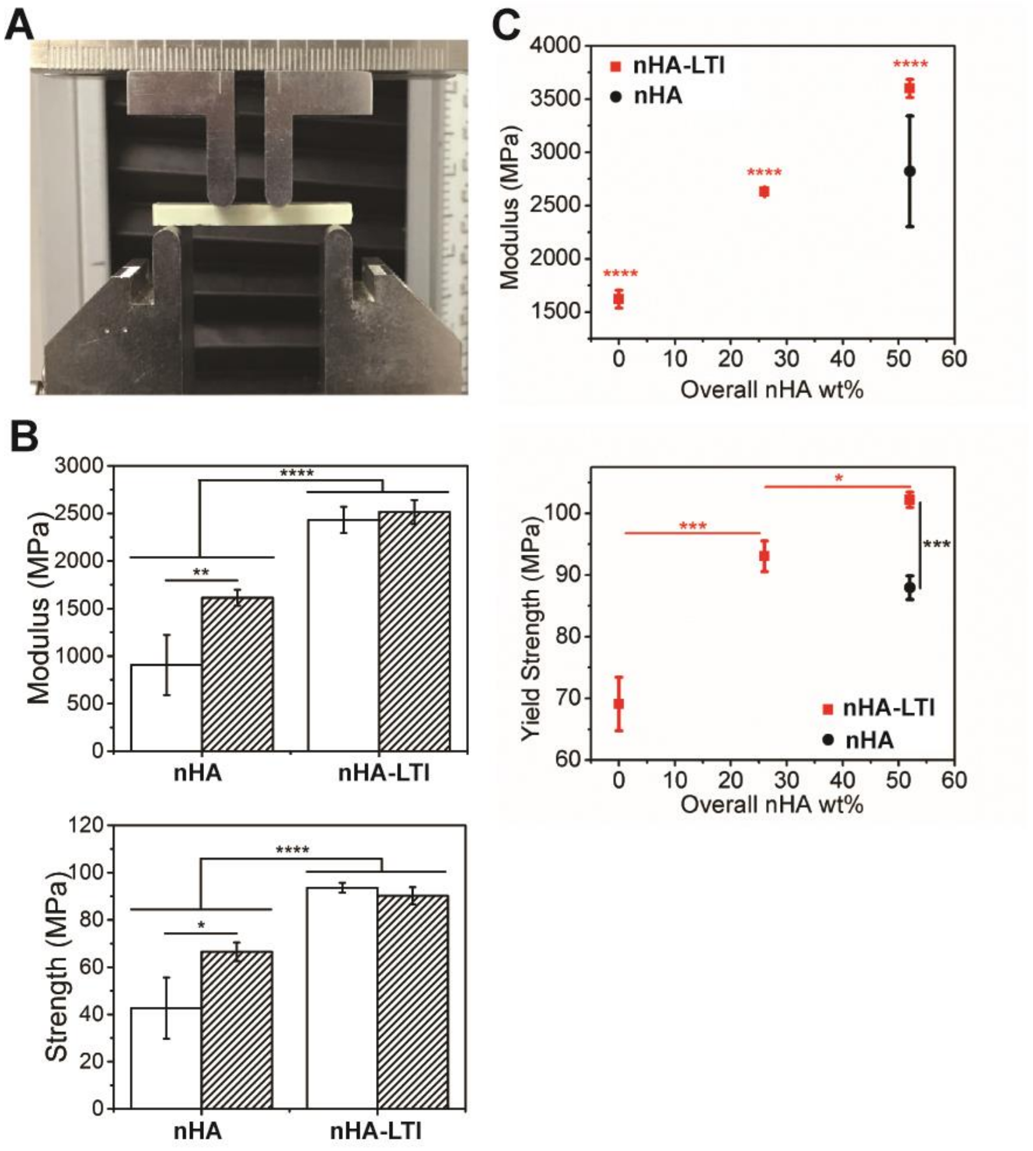

Figure 3.5 Mechanical properties of nHA/PEUR nanocomposites. (A) Experimental setup for the four-point bending test. (B) Four-point bending modulus and strength of nHA-LTI nanocomposites were

significantly higher than that of nHA nanocomposites at index 115 (white) and 140 (hatched). (C) Compression modulus and strength of nHA-LTI nanocomposites (red) increased with nHA loading and were significantly higher than that of nHA nanocomposites (black).

Four-point bending properties of nHA and nHA-LTI nanocomposites were measured using the apparatus described in ISO 5833 (**Figure 3.5A**), the international standard for PMMA, at Index 115 and 140.[3, 4] The effects of the isocyanate index on bending strength and modulus were significant for nHA but not nHA-LTI nanocomposites. Surface grafting significantly increased nanocomposite bending modulus and strength 20 - 50% at both indices compared to no grafting (**Figure 3.5B**). For quasi-static compression testing, nanocomposites were cured in 6-mm cylindrical tubes, cut to 12 mm, and soaked in PBS at 37 °C for 24 hours prior to testing. The yield strength of nHA-LTI nanocomposite increased with nHA-LTI loading up to 52 wt% (65 wt% nHA-LTI in nHA-LTI/LTI prepolymer) (**Figure 3.5C**). Furthermore, nHA-LTI nanocomposites with > 26 wt% nHA exhibited higher compressive strength than nHA nanocomposites with 52 wt% nHA. Similar trends were observed for Young's modulus. The mechanical properties of nHA-LTI nanocomposite exceeded the standard requirements for non-resorbable PMMA, including compressive strength of 70 – 90 MPa, compressive modulus of 2000 – 3000 MPa, and bending strength >80 MPa.[3, 4]

Protein adsorption on nHA/PEUR composites

To evaluate the effect of nHA-LTI grafting on the biological properties of the nanocomposites, water contact angle (Figure **3.6A**) and adsorption of fibronectin and vitronectin (**Figure 3.6B, C**) were measured. LTI-poly(ester urethane) (LTI-PEUR) without nHA had a contact angle $\theta = 50^o$. With 30 vol% (52 wt%) nHA loading, nHA-LTI nanocomposite ($\theta = 25.2° \pm 4.9°$) was more hydrophilic than nHA nanocomposite ($\theta = 32.2° \pm 5.8°$), suggesting that that the more homogenous dispersion of nHA-LTI rendered the surface more like HA (θ=10^o).[56] Specimens were also incubated in 5 μg/ml fibronectin or vitronectin solutions at 37°C and protein adsorption measured using a Pierce BCA kit. The nanocomposites exhibited a two-fold increase in fibronectin and vitronectin adsorption compared to the LTI-PEUR control. Fibronectin adsorption was comparable to that reported for pure HA with similar grain size, while vitronectin adsorption was lower than that reported for HA.[57]

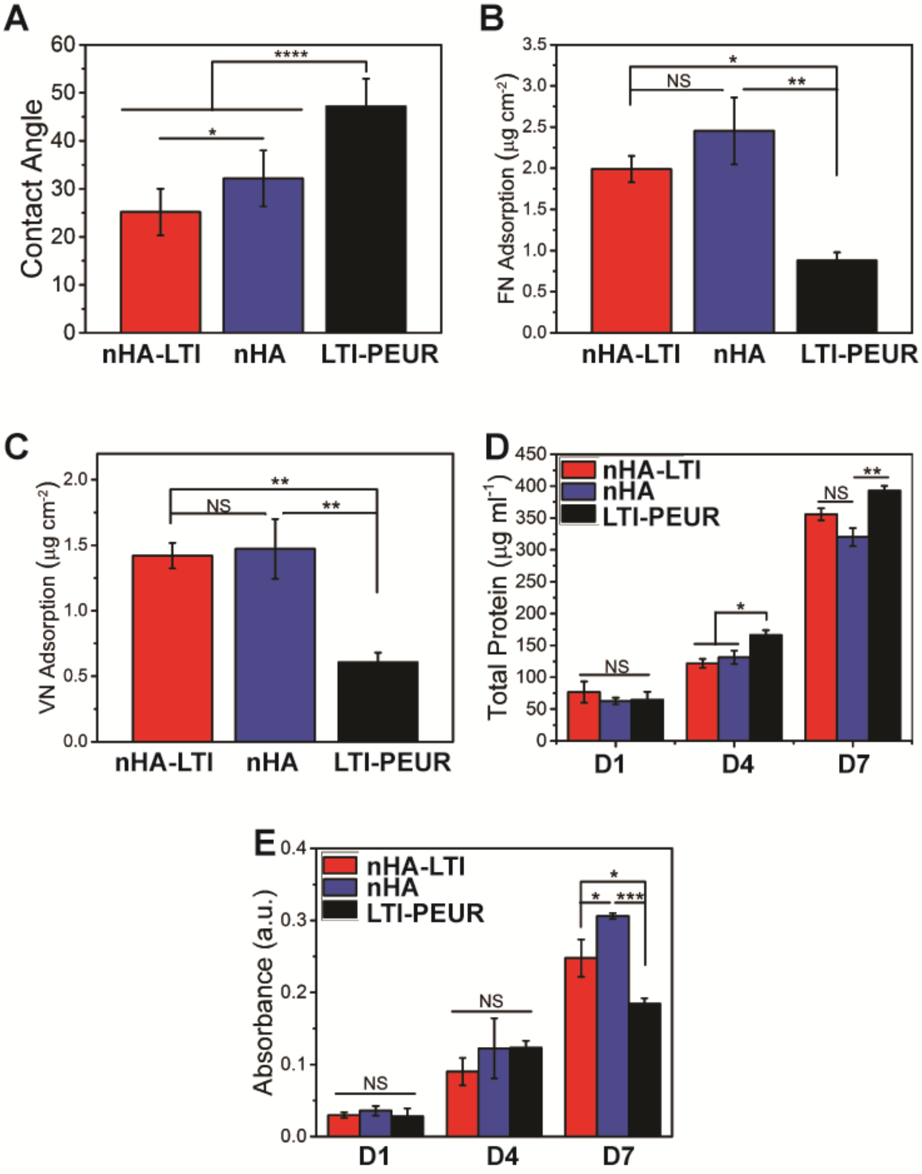

Figure 3.6 Protein adsorption and osteoblast proliferation on nHA/PEUR nanocomposites. (A) Water contact angle measured for nHA-LTI and nHA nanocomposites and LTI-PEUR control. (B-C) Protein adsorption of (B) fibronectin and (C) vitronectin on nHA-LTI and nHA nanocomposites were significantly higher than that on LTI-PEUR. (D) Total protein measurement at day 1, 4 and 7 showed insignificant differences in proliferation of MC3T3 pre-osteoblast cells between nHA and nHA-LTI

nanocomposites. Total protein was significantly higher on LTI-PEUR controls on days 4 and 7. (E) MTS assay showed significant differences between groups on day 7.

Cell proliferation and osteoblast mineralization on nHA/PEUR nanocomposites

Cell viability, proliferation, and differentiation of osteoblasts on the nanocomposites were also assessed. Mouse MC3T3 cells were suspended in complete medium and seeded onto the substrates. Total protein increased from Day 1 to 7 for all groups, thereby indicating that cells proliferated on the surface (**Figure 3.6D**). Proliferation was significantly higher on the LTI-PEUR control compared to the nanocomposites, but differences in proliferation between the nHA and nHA-LTI groups were insignificant. This observed reduction in proliferation on nHA and nHA-LTI is consistent with increased differentiation and mineralization of hMSCs on these surfaces compared to the nHA-PEUR control (**Figure 3.7**), since induction of osteoblast gene induction is linked to down-regulation of proliferation.[58] Cell proliferation assessed by the MTS assay showed significant differences between groups on day 7, with the highest cell numbers on the nHA nanocomposite (**Figure 3.6E**).

Mineralization of human mesenchymal stem cells (hMSCs) cultured on the nanocomposites was assessed by Alizarin Red staining and SEM to assess the effects of surface grafting on nHA activity. Human MSCs were cultured in osteogenic medium, and mineralization was assessed by Alizarin Red staining on day 7 (**Figure 3.7A**). Staining was quantified by extraction of Alizarin Red from the substrates and also by measuring the area% of stained surface (**Figure 3.7B, C**). On day 7, the LTI-PEUR control showed minimal staining. In contrast, nHA-LTI showed significantly higher absorption and area% stained compared to nHA, while SEM images reveal further evidence of mineralized matrix on the nanocomposites on day 7 (**Figure 3.7D**).

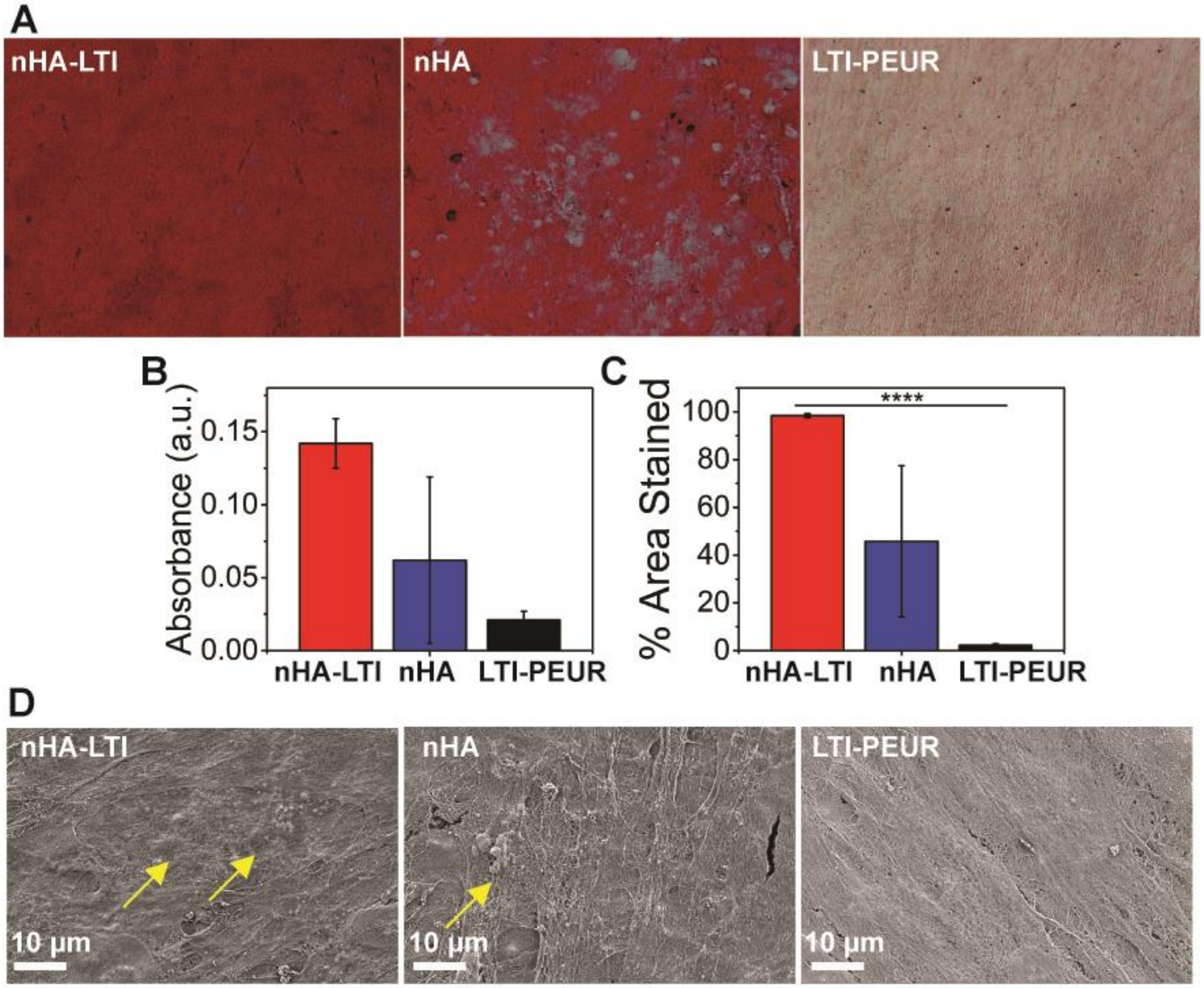

Figure 3.7 Osteoblast mineralization on nHA/PEUR nanocomposites. (A) Alizarin red staining of human mesenchymal stem cells (hMSCs) cultured on nHA-LTI, nHA and LTI-PEUR. Substrates were stained on day 7. Mineralization (red staining) was observed as early as day 7 on nHA and nHA-LTI nanocomposites but not on LTI-PEUR controls. (B-C) Quantification of alizarin red staining (day 7) by (B) extraction of the dye and (C) area % stained using ImageJ showed that mineralization was most extensive on nHA-LTI nanocomposites. (D) SEM images of the substrates after 7 days of culture with hMSCs. Mineralized nodules (yellow arrows) were observed on nHA-LTI and nHA but not on LTI-PEUR.

Osteoclast-mediated resorption of nHA/PEUR nanocomposites

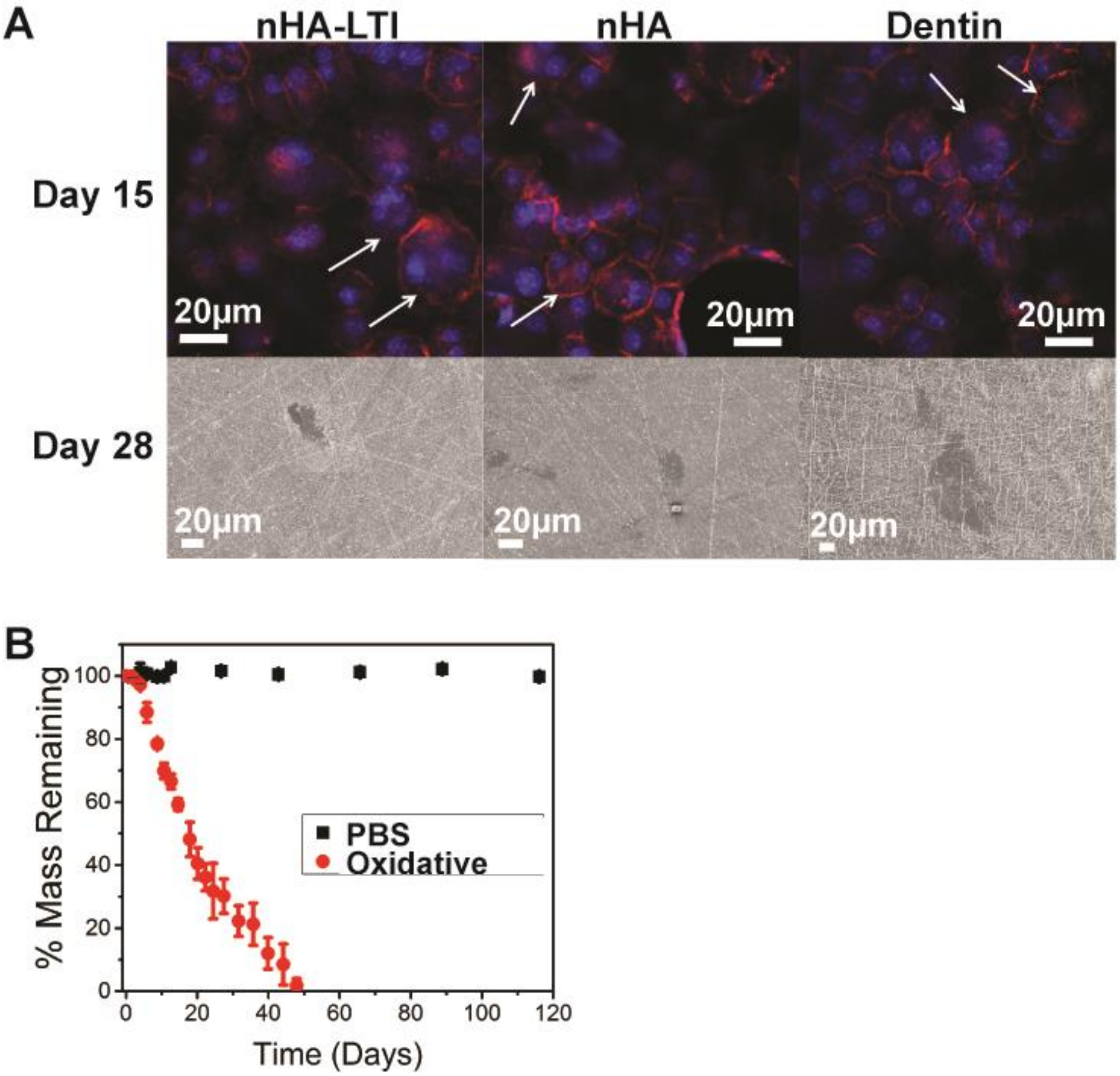

Figure 3.8 Osteoclast-mediated resorption of nHA-PEUR nanocomposites. (A) Actin (red)/nuclear (blue) staining of osteoclasts (white arrows) on day 15 (top row). Resorption pits formed on nHA and nHA-LTI nanocomposites and the dentin control at day 28 (bottom row). Osteoclasts did not form on PEUR controls. (B) nHA-LTI nanocomposites were hydrolytically stable but degraded in oxidative (20% H_2O_2 + $CoCl_2$) medium.

To evaluate osteoclast-mediated resorption of the nanocomposites, MC3T3 cells were co-cultured with RAW 264.7 cells in osteogenic medium supplemented with 10 nM Vitamin D 3 to stimulate their differentiation to osteoclasts. Actin (red)/DAPI (blue nucleus) staining was performed on day 15. Osteoclasts were identified as multi-nucleated cells with an actin ring (**Figure 3.8A**, top row). Resorption pits on the surface of nHA and nHA-LTI nanocomposites as well as the dentin control were observed by SEM on day 28 (**Figure 3.8A**, bottom row). No evidence of osteoclasts or resorption was observed for LTI-PEUR. The *in vitro* degradation rate of the nHA-LTI nanocomposite was assessed by immersion in PBS or oxidative medium (20% H_2O_2 + $CoCl_2$) at 37°C. While the nHA-LTI nanocomposite was hydrolytically stable in PBS, it exhibited >35% mass loss in oxidative medium after 21 days and fully degraded within 48 days (**Figure 3.8B**).

Discussion

Grain sizes less than 100 nm enhance osteogenic differentiation compared to micron-scale HA.[23] However, the effects of surface grafting on nHA activity have not been extensively investigated. The observed enhanced mineralization of hMSCs on nHA-LTI substrates is attributed to the improved dispersion of nHA, which is consistent with the notion that grain sizes less than 100 nm enhance osteogenic differentiation compared to micron-scale HA.[23] Similarly, a recent study has reported that grafting L-lactic acid oligomer to nHA enhanced mineralization and bone healing of scaffolds fabricated from nHA/poly(lactic-*co*-glycolic acid) blends.[37] Taken together, these findings suggest that surface grafting organic molecules to nHA enhances its dispersion in polymeric nanocomposites, thereby preserving its <100 nm feature size and enhancing mineralization.

The findings that nHA-PEUR nanocomposites were hydrolytically stable but degraded rapidly in oxidative environment are consistent with another study reporting that the LTI-PEUR polymer showed minimal (< 5%) degradation in PBS after 8 months. In oxidative medium, the nHA-LTI nanocomposite degraded faster than the LTI-PEUR polymer, which degraded <10% after 21 days.[59, 60] The faster rate of degradation in oxidative compared to hydrolytic medium is consistent with the observed resorption of nHA-LTI by osteoclasts, which secrete reactive oxygen species (ROS) during bone remodeling.[61-64] The combination of enhanced mineralization by osteoblasts and osteoclast-mediated resorption is anticipated to minimize resorption and fibrous scar formation *in vivo* by aligning the rates of new bone formation and graft resorption.[12, 65]

Injectable and settable bone grafts may present potentially harmful effects on host tissue, such as heat released from chemical exotherms and reaction of monomers with host tissue.[66] Non-lysine-derived polyisocyanates have shown cytotoxic effects on cells, including fibroblasts and lymphocytes.[67-69] While we did not investigate the biocompatibility of injectable nHA-PEUR nanocomposites in this study, previous work from our group and others' has reported that reactive lysine-derived polyurethanes do not release cytotoxic components or large amount of heat that do harm to cells and host tissue and stimulate healing in preclinical models of tissue regeneration.[48, 60, 70-74]

Conclusion

This study highlights the potential of nHA-PEUR nanocomposites as a new approach for promoting bone healing at weight-bearing sites. These materials set within 5 – 10 minutes after injection, exhibit strength comparable to non-resorbable PMMA bone cement, stimulate osteogenic differentiation of endogenous cells, and resorb at a rate aligned with patient biology. This ideal combination of properties, which is essential for treating weight-bearing bone defects, cannot be achieved using other biomaterials. Surface grafting of LTI to nHA enhanced the dispersion of nHA in the nanocomposite, resulting in compression and bending strengths exceeding that of PMMA (the only biomaterial indicated for structural repair of bone) as well as enhanced mineralization of osteoprogenitor cells. While nHA-PEUR nanocomposites were hydrolytically stable, they degraded in response to ROS and osteoclasts, which are associated with physiological bone remodelling.[61-64] These proof-of-concept findings highlight the potential of nHA-PEUR nanocomposites for repair and restoration of bone defects at weight-bearing sites.

References

1. Ramakrishna, S., et al., *Biomedical applications of polymer-composite materials: a review.* Composites Science and Technology, 2001. **61**(9): p. 1189- 1224.
2. Bohner, M., *Design of Ceramic-Based Cements and Putties for Bone Graft Substitution.* European Cells & Materials, 2010. **20**: p. 1-12.
3. ISO, *International Standard 5833*: *Implants for Surgery - Arylic Resin Cements*. 2002.
4. Kuehn, K.-D., *Bone Cements*. 2000, Berlin: Springer.
5. Aamodt, A., et al., *Documentation of hip prostheses used in Norway - A critical review of the literature from 1996-2000.* Acta Orthopaedica Scandinavica, 2004. **75**(6): p. 663-676.
6. Bettencourt, A., et al., *Surface studies on acrylic bone cement.* International Journal of Pharmaceutics, 2004. **278**(1): p. 181-186.
7. Savarino, L., et al., *Microstructural Investigation of Bone-Cement Interface.* Journal of Biomedical Materials Research, 1995. **29**(6): p. 701-705.
8. Berry, D.J., et al., *Twenty-five-year survivorship of two thousand consecutive primary Charnley total hip replacements - Factors affecting survivorship of acetabular and femoral components.* Journal of Bone and Joint Surgery-American Volume, 2002. **84A**(2): p. 171-177.
9. Jasty, M., et al., *The Initiation of Failure in Cemented Femoral Components of Hip Arthroplasties.* Journal of Bone and Joint Surgery-British Volume, 1991. **73**(4): p. 551-558.
10. Frankenburg, E.P., et al., *Biomechanical and histological evaluation of a calcium phosphate cement.* Journal of Bone and Joint Surgery-American Volume, 1998. **80A**(8): p. 1112-1124.
11. Harmata, A.J., et al., *Compressive fatigue and fracture toughness behavior of injectable, settable bone cements.* Journal of the Mechanical Behavior of Biomedical Materials, 2015. **51**: p. 345-355.
12. Dumas, J.E., et al., *Balancing the rates of new bone formation and polymer degradation enhances healing of weight-bearing allograft/polyurethane composites in rabbit femoral defects.* Tissue Eng Part A, 2014. **20**(1-2): p. 115-29.
13. Gay, S., S. Arostegui, and J. Lemaitre, *Preparation and characterization of dense nanohydroxyapatite/PLLA composites.* Materials Science & Engineering C-Biomimetic and Supramolecular Systems, 2009. **29**(1): p. 172-177.
14. Dumas, J.E., et al., *Synthesis of Allograft Bone/Polymer Composites and Evaluation of Remodeling in a Rabbit Femoral Condyle Model.* Acta Biomaterialia, **2010**. **6**: p. 2394–2406.
15. Kruger, R. and J. Groll, *Fiber reinforced calcium phosphate cements -- on the way to degradable load bearing bone substitutes?* Biomaterials, 2012. **33**(25): p. 5887-900.
16. Kruger, R., et al., *Strong and tough magnesium wire reinforced phosphate cement composites for load-bearing bone replacement.* J Mech Behav Biomed Mater, 2013. **20**: p. 36-44.
17. Mahony, O., et al., *Silica-Gelatin Hybrids with Tailorable Degradation and Mechanical Properties for Tissue Regeneration.* Advanced Functional Materials, 2010. **20**(22): p. 3835-3845.
18. Valliant, E.M., et al., *Bioactivity in silica/poly(gamma-glutamic acid) sol-gel hybrids through calcium chelation.* Acta Biomaterialia, 2013. **9**(8): p. 7662-7671.
19. Yu, B.B., et al., *Effect of Calcium Source on Structure and Properties of Sol-Gel Derived Bioactive Glasses.* Langmuir, 2012. **28**(50): p. 17465-17476.
20. Valliant, E.M. and J.R. Jones, *Softening bioactive glass for bone regeneration: sol-gel hybrid materials.* Soft Matter, 2011. **7**(11): p. 5083-5095.
21. Poologasundarampillai, G., et al., *Poly(gamma-glutamic acid)/Silica Hybrids with Calcium Incorporated in the Silica Network by Use of a Calcium Alkoxide Precursor.* Chemistry-a European Journal, 2014. **20**(26): p. 8149-8160.
22. Mahony, O., et al., *Silica-gelatin hybrids for tissue regeneration: inter-relationships between the process variables.* Journal of Sol-Gel Science and Technology, 2014. **69**(2): p. 288-298.
23. Webster, T.J., et al., *Enhanced functions of osteoblasts on nanophase ceramics.* Biomaterials, 2000. **21**(17): p. 1803-1810.

24. Laurencin, C.T., S.G. Kumbar, and S.P. Nukavarapu, *Nanotechnology and orthopedics: a personal perspective.* Wiley Interdisciplinary Reviews-Nanomedicine and Nanobiotechnology, 2009. **1**(1): p. 6-10.
25. Sun, F., H. Zhou, and J. Lee, *Various preparation methods of highly porous hydroxyapatite/polymer nanoscale biocomposites for bone regeneration.* Acta Biomaterialia, 2011. **7**(11): p. 3813-3828.
26. Ngiam, M., et al., *The fabrication of nano-hydroxyapatite on PLGA and PLGA/collagen nanofibrous composite scaffolds and their effects in osteoblastic behavior for bone tissue engineering.* Bone, 2009. **45**(1): p. 4-16.
27. Sato, M. and T.J. Webster, *Nanobiotechnology: implications for the future of nanotechnology in orthopedic applications.* Expert Review of Medical Devices, 2004. **1**(1): p. 105-114.
28. Tran, P.A., et al., *Opportunities for nanotechnology-enabled bioactive bone implants.* Journal of Materials Chemistry, 2009. **19**(18): p. 2653-2659.
29. Meirelles, L., et al., *Effect of Hydroxyapatite and Titania Nanostructures on Early In Vivo Bone Response.* Clinical Implant Dentistry and Related Research, 2008. **10**(4): p. 245-254.
30. Meirelles, L., et al., *Nano hydroxyapatite structures influence early bone formation.* Journal of Biomedical Materials Research Part A, 2008. **87A**(2): p. 299-307.
31. MacMillan, A.K., et al., *Similar healthy osteoclast and osteoblast activity on nanocrystalline hydroxyapatite and nanoparticles of tri-calcium phosphate compared to natural bone.* International Journal of Nanomedicine, 2014. **9**: p. 5627-5637.
32. Webster, T.J., et al., *Enhanced osteoclast-like cell functions on nanophase ceramics.* Biomaterials, 2001. **22**(11): p. 1327-1333.
33. Harmata, A.J., et al., *Investigating the effects of surface-initiated polymerization of epsilon-caprolactone to bioactive glass particles on the mechanical properties of settable polymer/ceramic composites.* Journal of Materials Research, 2014. **29**(20): p. 2398-2407.
34. Supova, M., *Problem of hydroxyapatite dispersion in polymer matrices: a review.* J Mater Sci Mater Med, 2009. **20**: p. 1201-1213.
35. Tanaka, H., et al., *Surface Structure and Properties of Calcium Hydroxyapatite Modified by Hexamethyldisilazane.* J Coll Interfac Sci, 1998. **206**: p. 205-211.
36. Liu, Q., et al., *Surface modification of nano-apatite by grafting organic polymer.* Biomaterials, 1998. **19**: p. 1067-72.
37. Wang, Z.L., et al., *Enhanced in Vitro Mineralization and in Vivo Osteogenesis of Composite Scaffolds through Controlled Surface Grafting of L-Lactic Acid Oligomer on Nanohydroxyapatite.* Biomacromolecules, 2016. **17**(3): p. 818-829.
38. Dong, G.C., et al., *A study on grafting and characterization of HMDI-modified calcium hydrogenphosphate.* Biomaterials, 2001. **22**(23): p. 3179-3189.
39. Lee, H.J., et al., *The effect of surface-modified nano-hydroxyapatite on biocompatibility of poly(epsilon-caprolactone)/hydroxyapatite nanocomposites.* European Polymer Journal, 2007. **43**(5): p. 1602-1608.
40. Jiang, L.Y., et al., *Effect of l-lysine-assisted surface grafting for nano-hydroxyapatite on mechanical properties and invitro bioactivity of poly(lactic acid-co-glycolic acid).* Journal of Biomaterials Applications, 2016. **30**(6): p. 750-758.
41. Dong, S.J., et al., *Preparation, Surface Properties and Biological Activity of the Composite of Poly (lactide-co-glycolide) and Bioglass Nanoparticles Surface Grafted with Poly(L-lactide).* Chemical Journal of Chinese Universities-Chinese, 2009. **30**(5): p. 1018-1023.
42. Fan, R.R., et al., *Preparation and properties of g-TTCP/PBS nanocomposites and its in vitro biocompatibility assay.* International Journal of Biological Macromolecules, 2013. **59**: p. 227-234.
43. Jiang, L.Y., et al., *Effect of n-HA with different surface-modified on the properties of n-HA/PLGA composite.* Applied Surface Science, 2012. **259**: p. 72-78.

44. Jiang, L.X., et al., *Effect of a new surface-grafting method for nano-hydroxyapatite on the dispersion and the mechanical enhancement for poly(lactide-co-glycolide).* Express Polymer Letters, 2014. **8**(2): p. 133-141.
45. Qiu, X.Y., et al., *Surface-modified hydroxyapatite linked by L-lactic acid oligomer in the absence of catalyst.* Journal of Polymer Science Part a-Polymer Chemistry, 2005. **43**(21): p. 5177-5185.
46. Hafeman, A.E., et al., *Characterization of the degradation mechanisms of lysine-derived aliphatic poly(ester urethane) scaffolds.* Biomaterials, 2011. **32**(2): p. 419-429.
47. Martin, J.R., et al., *A porous tissue engineering scaffold selectively degraded by cell-generated reactive oxygen species.* Biomaterials, 2014. **35**(12): p. 3766-3776.
48. Page, J.M., et al., *Biocompatibility and chemical reaction kinetics of injectable, settable polyurethane/allograft bone biocomposites.* Acta Biomaterialia, 2012. **8**(12): p. 4405-4416.
49. *ASTM D2572-97: Standard Test Method for Isocyanate Groups in Urethane Materials for Prepolymers*. 2010, ASTM International: West Conshohocken, PA.
50. John F. Moulder, W.F.S., Peter E. Sobol, Kenneth D. Bomben, *Handbook of X-ray photoelectron spectroscopy*, ed. R.C.K. Jill Chastain, Jr. 1995, Chanhassen, Minnesota: Physical Electronics USA, Inc.
51. Yubao, L., et al., *Shape change and phase transition of needle-like non-stoichiometric apatite crystals.* Journal of Materials Science-Materials in Medicine, 1994. **5**: p. 263-268.
52. *ASTM D6272-10: Standard Test Method for Flexural Properties of Unreinforced and Reinforced Plastics and Electrical Insulating Materials by Four-Point Bending*. 2010: West Conshohocken, PA.
53. Sidqui, M., et al., *Osteoblast Adherence and Resorption Activity of Isolated Osteoclasts on Calcium-Sulfate Hemihydrate*. Biomaterials, 1995. **16**(17): p. 1327-1332.
54. Schilling, A.F., et al., *Resorbability of bone substitute biomaterials by human osteoclasts.* Biomaterials, 2004. **25**(18): p. 3963-3972.
55. Kopusov, L.I. and V.V. Zharkov, *Spectral Studies On the Structure of Polyurethane Elastomers.* Journal of Applied Spectroscopy, 1966. **5**(1): p. 95-97.
56. Aronov, D., et al., *Tunable hydroxyapatite wettability: Effect on adhesion of biological molecules.* Process Biochemistry, 2006. **41**(12): p. 2367-2372.
57. Webster, T.J., et al., *Specific proteins mediate enhanced osteoblast adhesion on nanophase ceramics.* Journal of Biomedical Materials Research, 2000. **51**(3): p. 475-483.
58. G. S. Stein, J.B.L., J. L. Stein, A. J. Van Wijnen, B. Frenkel, M. Montecino, *Mechanisms Regulating Osteoblast Proliferation and Differentiation*, in *Principles of Bone Biology*, L.G.R. John P. Bilezikian, Gideon A. Rodan, Editor. 1996, Academic Press: New York. p. 71.
59. Guelcher, S.A., et al., *Synthesis, mechanical properties, biocompatibility, and biodegradation of polyurethane networks from lysine polyisocyanates.* Biomaterials, 2008. **29**(12): p. 1762-1775.
60. McEnery, M.A.P., et al., *Oxidatively Degradable Poly(thioketal urethane)/Ceramic Composite Bone Cements with Bone-like Strength.* RSC Advances, 2016. **6**(111): p. 109414-109424.
61. Sheweita, S.A., K.I. Khoshhal, and H. Baghdadi, *Osteoporosis and Oxidative Stress - Role of Antioxidants*, in *Systems Biology of Free Radicals and Antioxidants*, I. Laher, Editor. 2014, Springer: Verlag Berlin Heidelberg. p. 2973-2995.
62. Garrett, I.R., et al., *Oxygen-Derived Free-Radicals Stimulate Osteoclastic Bone-Resorption in Rodent Bone Invitro and Invivo.* Journal of Clinical Investigation, 1990. **85**(3): p. 632-639.
63. Key, L.L., et al., *SUPEROXIDE AND BONE-RESORPTION.* Bone, 1994. **15**(4): p. 431-436.
64. Banfi, G., E.L. Iorio, and M.M. Corsi, *Oxidative stress, free radicals and bone remodeling.* Clinical Chemistry and Laboratory Medicine, 2008. **46**(11): p. 1550-1555.
65. Lorden, E.R., et al., *Mitigation of hypertrophic scar contraction via an elastomeric biodegradable scaffold.* Biomaterials, 2015. **43**: p. 61-70.
66. Guelcher, S.A., *Biocompatibility of Injectable Materials*, in *Injectable Biomaterials: Science and Applications*, B. Vernon, Editor. 2011, Woodhead Publishing: Philadelphia.

67. Ertel, S.I., et al., *In-Vitro Study of The Intrinsic Toxicity of Synthetic Surfaces to Cells.* Journal of Biomedical Materials Research, 1994. **28**(6): p. 667-675.
68. Pons, F., et al., *Effect of toluene diisocyanate and its corresponding amines on viability and growth of human lung fibroblasts in culture.* Cell Biology and Toxicology, 1999. **15**(5): p. 333-340.
69. Mishra, P.K., et al., *Isocyanates Induces DNA Damage, Apoptosis, Oxidative Stress, and Inflammation in Cultured Human Lymphocytes.* Journal of Biochemical and Molecular Toxicology, 2008. **22**(6): p. 429-440.
70. Hafeman, A.E., et al., *Injectable biodegradable polyurethane scaffolds with release of platelet-derived growth factor for tissue repair and regeneration.* Pharmaceutical Research, 2008. **25**(10): p. 2387-2399.
71. Adhikari, R., et al., *Biodegradable injectable polyurethanes: Synthesis and evaluation for orthopaedic applications.* Biomaterials, 2008. **29**(28): p. 3762-3770.
72. Buckley, M.J. and E.J. Beckman, *Adhesive Use in Oral and Maxillofacial Surgery.* Oral and Maxillofacial Surgery Clinics of North America, 2010. **22**(1): p. 195-199.
73. Zhang, J.Y., et al., *Synthesis, biodegradability, and biocompatibility of lysine diisocyanate-glucose polymers.* Tissue Engineering, 2002. **8**(5): p. 771-785.
74. Bennett, S., et al., *Initial biocompatibility studies of a novel degradable polymeric bone substitute that hardens in situ.* Bone, 1996. **19**(1): p. S101-S107.

CHAPTER 4 - CHARACTERIZATION OF NANOCRYSTALLINE HYDROXYAPATITE-LYSINE TRIISOCYANATE GRAFTING REACTION AND EQUIVALENT WEIGHT OF NANOCRYSTALLINE HYDROXYAPATITE

Introduction

Nanocrystalline hydroxyapatite (nHA) is widely used in bone-mimetic biomaterials due to its chemical similarity to natural bone apatite, which accounts for up to 60%-70% of dry bone mass.[1] The nanoscale grain size of nHA has been reported to enhance osteogenic differentiation, new bone formation, and osteoclast differentiation and activity compared to micron-scale HA.[2-4] Thus, nHA has been widely incorporated in polymer composites for bone repair and restoration. However, nHA nanocrystals tend to aggregate when dispersed in polymers due to the potential incompatibility of the two components and high surface energy of the nHA nanoparticles, resulting in poor mechanical properties.[5]

Surface grafting organic molecules to nHA can enhance the dispersion of nHA in the polymer matrix. The hydroxyl groups on surface of nHA can be used to graft organic molecules, such as polyesters and polyisocyanates.[6-11] Surface grafting organic molecules to nHA enhances their dispersion in the organic polymer matrix, as well as interfacial binding between the polymer and nHA ceramic phase, resulting in improved mechanical properties as well as biological properties in terms of stimulation of cell attachment, proliferation and differentiation.[10, 12-18]

In our recent study described in Chapter III, we have shown that surface grafting lysine-triisocyanate (LTI) to nHA enhanced the dispersion of the LTI grafted nHA particles (nHA-LTI) in the nHA-PEUR nanocomposite, resulting in enhanced mechanical and biological properties. To make the nHA-PEUR nanocomposite, a viscous nHA-LTI/LTI prepolymer was first made by mixing nHA with LTI in the presence of FeAA catalyst to graft LTI to surface of nHA. The nHA-LTI/LTI prepolymer was further crosslinked with a polyester triol by injection through a double-syringe static mixer to yield the final nHA-PEUR nanocomposite. The injectability of the nHA-LTI/LTI prepolymer and the mechanical properties of the final nHA-PEUR nanocomposite are highly dependent on the stability of the nHA-

LTI/LTI prepolymer. In Chapter III, the typical conversion of surface hydroxyl groups of nHA particles after the grafting reaction was 40%, and the remaining surface hydroxyl groups can continue to react with free LTI in the prepolymer overtime, resulting in gelation of the prepolymer and decrease in the amount of reactive isocyanate groups in the prepolymer, which further leads to low conversion of the crosslinking reaction between prepolymer and the polyester triol, and causes poor mechanical properties of the final nHA-PEUR nanocomposite.

To solve this problem, the conversion of the surface hydroxyl groups of nHA in the grafting reaction needs to reach nearly 100% to avoid undesired reaction during storage. In order to cap all the hydroxyl groups on the surface of nHA, two questions need to be answered: 1) how many reactive hydroxyl groups are there on the surface of nHA particles; 2) how to minimize side reaction.

In this chapter, the grafting reaction was conducted under different conditions. The change in %NCO of the prepolymer (i.e., the wt% of reactive isocyanate groups) was used as a marker for the extent of the reaction. When %NCO was stable, we assumed the reaction reached 100% conversion, and several methods for calculating the equivalent weight of nHA (i.e., the mass of nHA that corresponds to one mole of reactive surface hydroxyl group) were discussed.

Experimental

Materials

Lysine triisocyanate (LTI) was purchased from Jinan Haohua Industry Co., Ltd (Jinan, China), and was purified by refluxing with decolorizing carbon (Fisher Scientific) in *t*-butyl methyl ether (TBME, Acros-Organic) at 63°C for 22 hours before use. nHA (< 200 nm) particles were purchased from Sigma, and dried under vacuum at 80 °C for 48 hours before use. Nanostim (NS) paste was supplied by Medtronic (Memphis, TN), and was dewatered before use. Briefly, NS paste was resuspended in 2-propanol and centrifuged to yield NS pellet. This process was repeated with fresh 2-propanol for 3 times and the NS pellet was then dried at 80 °C under vacuum to yield NS particles. Catalyst solution (5 wt%) was prepared by dissolving iron acetylacetonate (FeAA, Sigma-Aldrich) in ε-caprolactone (Across-Organic), which was dried with magnesium sulfate (Thermofisher Scientific) before use.

Grafting reaction

For catalyzed reaction, nHA (40 wt%) was mixed with LTI (60 wt%) and FeAA catalyst (0.027 wt%) using a SpeedMixer (FlackTek, Inc., Landrum, SC) for 1 min. The reactive mixture was then transferred into a flask and reacted under stirring at room temperature under argon flow, which was dried in a drierite tube prior to entering the flask.

For uncatalyzed reaction, nHA was first mixed with LTI and FeAA catalyst (0.027 wt%) using the SpeedMixer for 10 min. The resulting mixture was immediately dissolved in TBME and centrifuged to recover nHA particles. After vacuum dried overnight, the recovered nHA (40 wt%) particles were redispersed in LTI (60 wt%) without FeAA catalyst, and the re-dispersed mixture was transferred into a flask and reacted under stirring at room temperature under argon flow, which was dried in a drierite tube prior to entering the flask.

For uncatalyzed reaction protected from water, nHA particles (45 wt%) were placed in a flask, heated to 80 °C under vacuum overnight and cooled to 40 °C under vacuum. The flask was then sealed with rubber septa and capped with an argon filled balloon to protect the reaction mixture from atmosphere. LTI (55 wt%) was added into the flask using syringe with needle through rubber septa. The uncatalyzed mixture was allowed to react under stirring at 40 °C for 16 hours and the resulting mixture was allowed to age at room temperature.

Samples were taken over the course of the reactions. The %NCO of the reaction mixture was measured by titration, and surface Nitrogen/Phosphorous (N/P) ratio of the recovered particles was measured by XPS.

FTIR

Dewatered NS particles (20 wt%) were mixed with LTI (80 wt%) and FeAA catalyst (0.027 wt%) using a SpeedMixer (FlackTek, Inc., Landrum, SC) for 1 min. The reactive mixture was then transferred into a flask and reacted under stirring at 40 °C under argon flow. Grafted NS particles were recovered from the reaction mixture after 123 hours, mixed with KBr (2 wt% grafted NS in KBr), and pressed into a pellet (100 mg) using a 13 mm KBr die set (International Crystal Laboratories, Garfield, NJ) under pressure of 7 tons and under vacuum. FTIR was preformed using a Tensor 27 FTIR (Bruker).

Results

Catalyzed reaction

%NCO of the catalyzed reaction mixture dropped over time (**Figure 4.1**). The catalyzed reaction mixture gelled after 120 hours, and %NCO could not be measured. The gel could be broken with chloroform and the particles were recovered for XPS measurement. The surface Nitrogen/Phosphorous (N/P) ratio of recovered nHA particles fluctuated, possibly due to the deviation of XPS measurement (**Figure 4.1**). While %NCO of the catalyzed reactive mixture decreased significantly over time, the surface N/P ratio of nHA particles didn't increase at later time points, suggesting the cause of gel formation was likely due to a reaction in the bulk.

FTIR analysis was conducted for recovered particles to characterize the reactions. A different source of nHA, Nanostim particles (NS) were used for FTIR. Although the shape and surface area are different for NS and nHA, the surface hydroxyl groups should reaction with LTI in the same way.

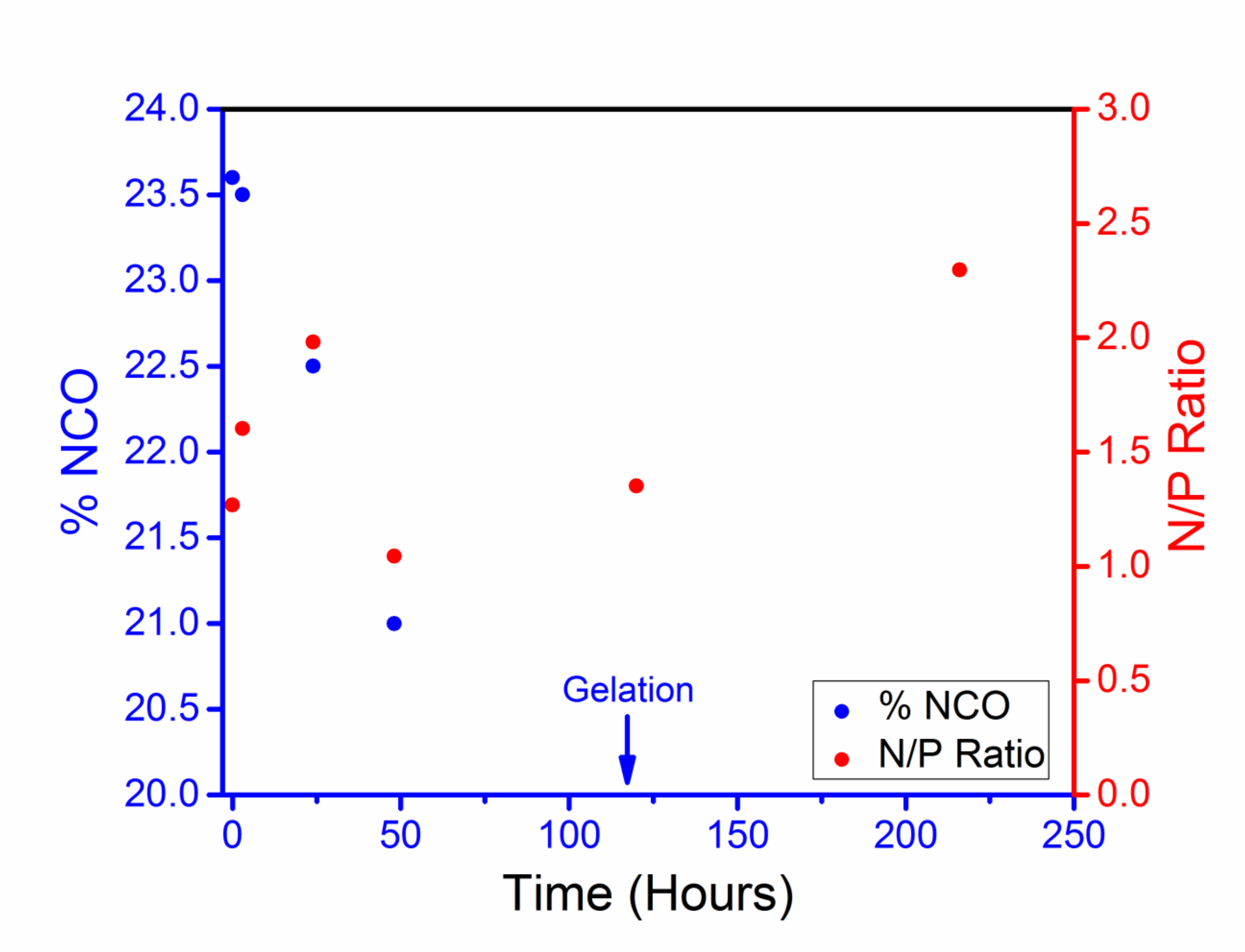

Figure 4.1 %NCO and N/P ratio for the catalyzed reaction mixture over time

FTIR spectra of grafted NS particles (**Figure 4.2**) showed N=C=O peak at 2260 cm^{-1} and P-O-C peak at around 1040 cm^{-1}, which overlapped with PO_4^{3-} of NS. These peaks indicate that LTI molecules were successfully grafted to NS through a urethane reaction. The broad peak near 3400 cm^{-1} correlates to N-H stretching of urethane. Multiple C=O peaks were observed for the grafted particles. The high frequency component at 1740 cm^{-1} is characteristic for urethane carbonyl stretching or ester C=O stretching (from LTI), while the low frequency component at around 1654 cm^{-1} overlaps with urea C=O stretching. The FTIR results indicate that the reaction between isocyanate group and water, which results in a di-substituted urea, is likely to be the reaction that caused the gelation.

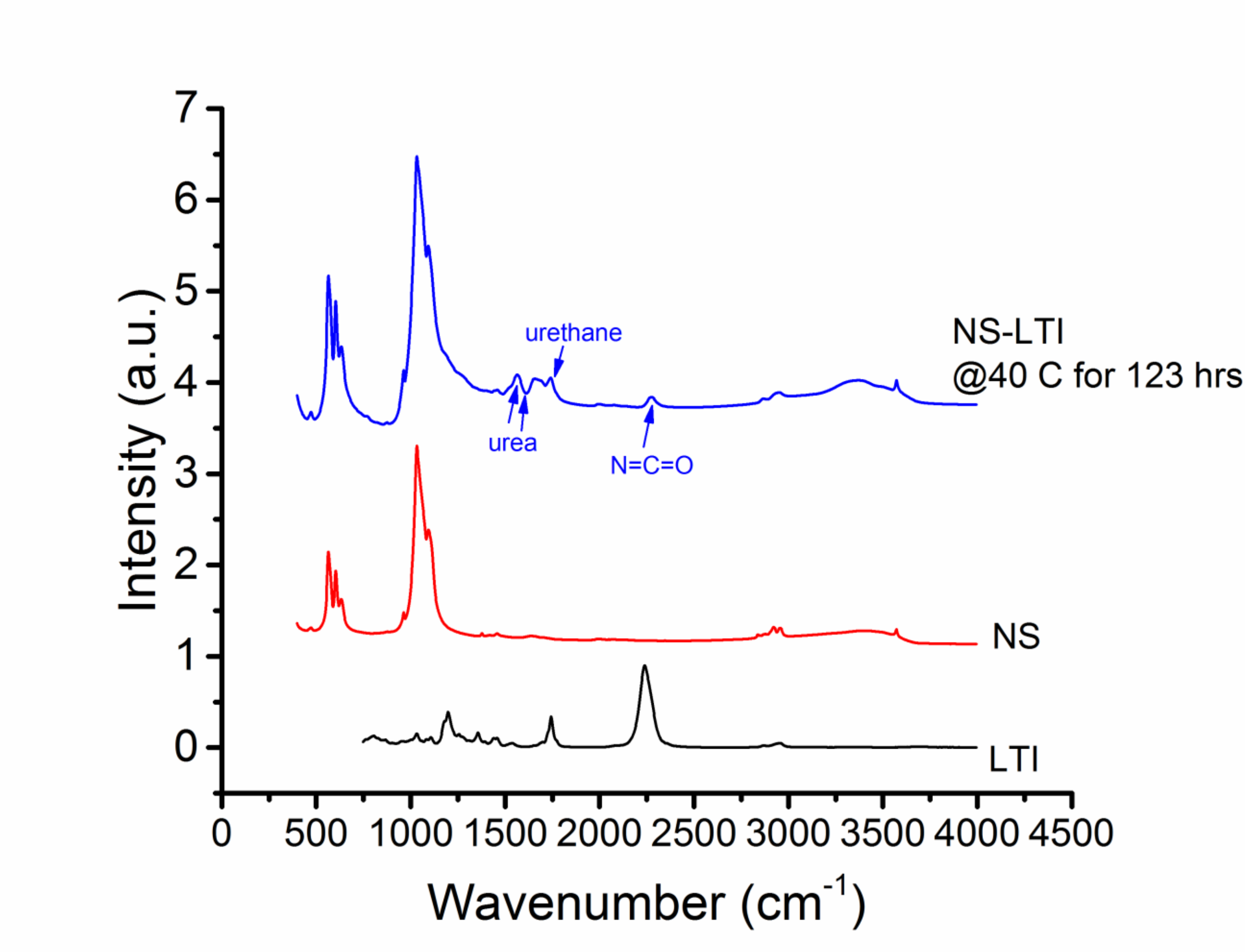

Figure 4.2 FTIR spectra of NS-LTI grafted particles show peaks associated with urea bonds.

Uncatalyzed reaction

Similar to the catalyzed reaction mixture, %NCO of the uncatalyzed reaction mixture also dropped over time, but at a relatively low rate compared to catalyzed mixture. While the uncatalyzed mixture did not gel, it showed a significant viscosity increase after 24 days of reaction.

From 48-216 h, the N/P ratio varied over the range 2.3 – 3.0. Since 3.0 is the theoretical maximum value (one grafted LTI molecule per P-OH, resulting in N/P = 3), the grafting reaction likely attained nearly complete conversion at 120 h. However, %NCO continued to decrease, suggesting that a bulk reaction (e.g., the water reaction) was continuing to consume NCO equivalents.

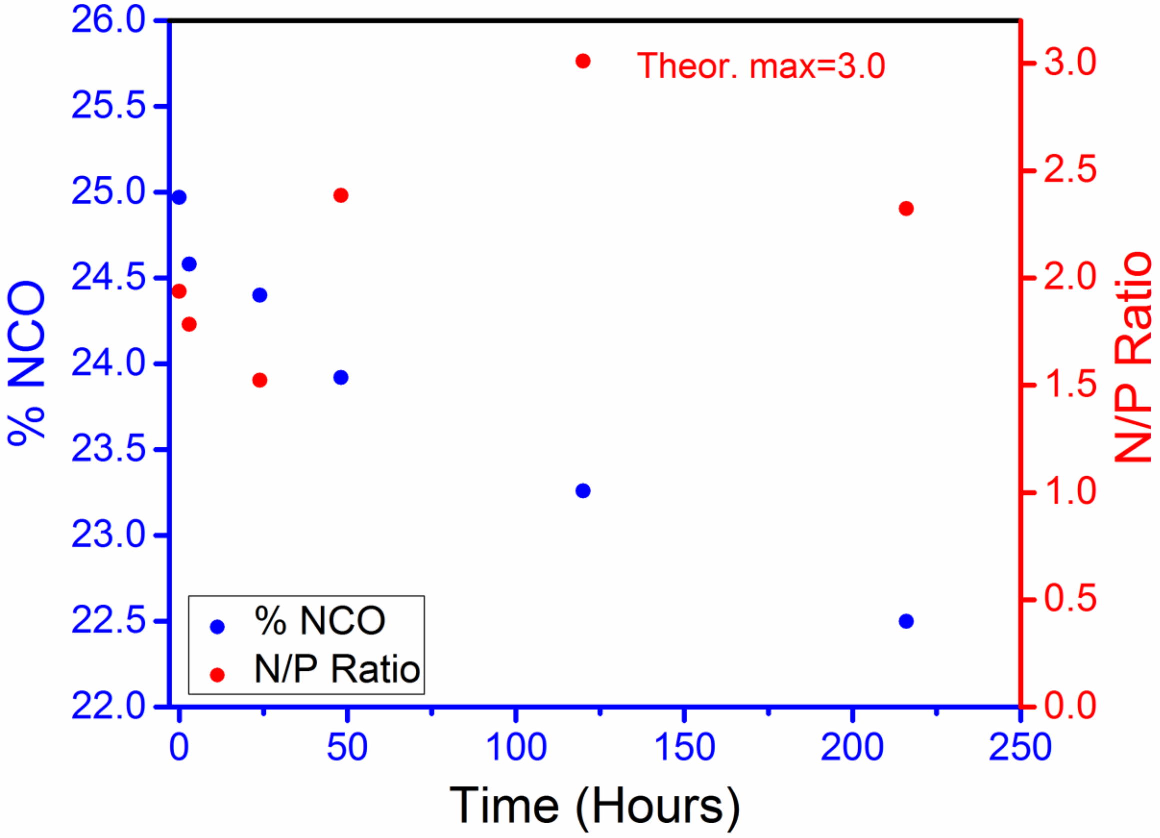

Figure 4.3 %NCO and N/P ratio of uncatalyzed reaction mixture over time

Uncatalyzed reaction protected from water

The results presented above revealed that water reaction in the bulk caused the gelation of the reaction mixture with and without catalyst. Although nHA particles were dried before use and the reaction was conducted under argon flow which was dried in a drierite tube prior to entering the flask, it is possible that the reaction mixture absorbed water while being transferred to the flask or that the drierite did not sufficiently remove water, resulting in accumulation of water in the flask over time. Therefore, we modified the protocol to avoid exposure of nHA to the atmosphere and used argon filled balloon to cap the flask instead of flowing argon continuously. The %NCO of the reaction mixture was measured over time (**Figure 4.4**).

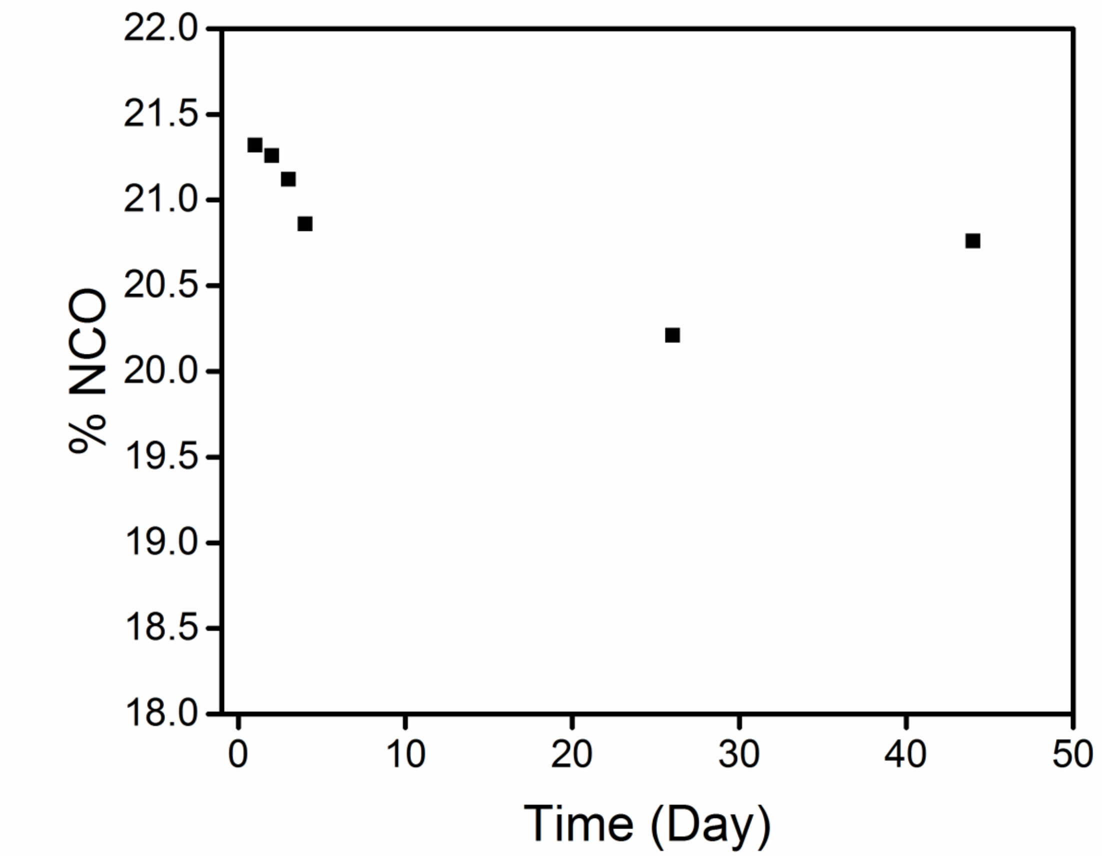

Figure 4.4 %NCO of the uncatalyzed reaction mixture protected from water

The %NCO of the uncatalyzed reaction mixture protected from water dropped initially during the first 4 days, reaching a plateau which was stable for up to 44 days, which suggests that the grafting reaction was complete at day 4 and no NCO equivalents were consumed after that.

Equivalent weight calculation from titration result

The results from uncatalyzed reaction protected from water suggest that water reaction was successfully prevented, and the mixture was stable. The final %NCO of the mixture was used to calculate the equivalent weight of nHA.

If there were no reaction between isocyanate and hydroxyl groups, the %NCO of the reaction mixture could be calculated based on dilution effect of nHA. For reaction mixture consisting of 45 wt% nHA:

$$\text{Equivalent weight of LTI}=\frac{42}{\text{NCO\% of LTI}}=\frac{42}{42.247\%}=99.415\ \text{g LTI}/\text{eq NCO} \qquad (4.1)$$

$$\text{\%NCO}=\frac{\text{mass due to unreacted NCO}}{\text{total mass}}=\frac{\dfrac{55\ \text{g LTI}}{99.415\ \text{g LTI/eq NCO}}\times 42\ \text{g/eq NCO}}{100\ \text{g}}=23.24\% \qquad (4.2)$$

The actual %NCO of the uncatalyzed mixture protected from water after 44 days was 20.76%. Thus, 2.48 g NCO was consumed during the grafting reaction, which is

$$\frac{2.48\ \text{g NCO}}{\dfrac{42\ \text{g NCO}}{\text{eq NCO}}}=0.05905\ \text{eq NCO} \qquad (4.3)$$

Since the mixture remained stable, it is appropriate to assume that conversion of surface hydroxyl group of nHA reached 100%. In the urethane reaction, one equivalent of NCO reacts with one equivalent of OH (hydroxyl group). Therefore, there is 0.05905 eq OH on the surface of 45 g nHA.

$$\text{nHA equivalent weight}=\frac{45\ \text{g nHA}}{0.05905\ \text{eq OH}}=762.07\ \text{g nHA/eq OH} \qquad (4.4)$$

To verify the nHA equivalent weight result, the theoretical value of %NCO of the prepolymer after the grafting reaction could be calculated back:

Mixing 1 equivalent each of OH and NCO will result in a 0%NCO prepolymer, i.e., mixing 762.07 g nHA and 99.415 g LTI will result in a 0%NCO prepolymer. In order to achieve 45 wt% nHA in mixture, 832.00 g of additional LTI needs to be added.

$$\%NCO = \frac{\text{Mass due to unreacted NCO}}{\text{Total mass}} = \frac{\dfrac{832.00\text{ g LTI}}{99.415\text{ g LTI/eq NCO}} \times \dfrac{42\text{ g}}{\text{eqNCO}}}{(832.00 + 762.07 + 99.415)\text{ g}} = 20.76\% \qquad (4.5)$$

This value is the same as experimental result.

Equivalent weight calculation from XPS result

XPS measures the surface N/P ratio. Since the water reaction occurred mainly in the bulk, the surface N/P remained stable and could be used to calculate equivalent weight of nHA as well.

From XPS data, the averaged surface N/P ratio =2 (*e.g.*, 2 mol N:mol P on the surface. The P-OH conversion is

$$\xi_{OH} = 2\frac{\text{mol N}}{\text{mol P}} \times 1\frac{\text{mol P}}{\text{mol OH}} \times 1\frac{\text{mol OH}}{\text{mol NCO}} \times (1\text{ or }2)\frac{\text{mol NCO}}{\text{mol LTI}} \times \frac{\text{mol LTI}}{3\text{ mol N}} = 0.67\text{ or }1.33 \qquad (4.6)$$

The two results correlate with two situations. If one of the two primary NCO groups of one LTI molecule reacted, ξ_{OH} would be 0.67, and if both of the primary NCO groups from the same LTI molecule reacted, the ξ_{OH} would be 1.33. The reactivity of secondary NCO group is lower than that of primary NCO, thus is not expected to react under room temperature without catalyst. The value greater than 1 suggests that one surface OH group reacted with more than one NCO group, possibly due to other side reactions or water reaction of the other isocyanate groups of grafted LTI molecule, which adds up the number of LTI molecule bond to the same surface OH group.

From previous results, if no reaction occurred, the theoretical %NCO calculated from dilution would be 23.24% NCO, and the actual %NCO after the reaction was 20.76%. The conversion of NCO was

$$\xi_{NCO} = \frac{23.24 - 20.76}{23.24} = 10.67\% \tag{4.7}$$

Equivalents of NCO that reacted:

$$q_{NCO} = 55 \text{ g LTI} \times \frac{\text{eq NCO}}{99.415 \text{ g LTI}} \times \xi_{NCO} = 0.0590 \text{ eq NCO} \tag{4.8}$$

Equivalents of surface OH of nHA:

$$q_{OH} = \frac{0.0590 \text{ eq NCO reacted}}{(0.67 \text{ or } 1.33) \text{ eq OH reacted/eq OH}} = 0.0881 \text{ or } 0.0444 \text{ eq OH} \tag{4.9}$$

$$\text{nHA equivalent weight} = \frac{45 \text{ g nHA}}{(0.0881 \text{ or } 0.0444) \text{ eq OH}} = 510.8 \text{ or } 1013 \ \frac{\text{g nHA}}{\text{eq OH}} \tag{4.10}$$

If one of the two primary NCO groups of a LTI molecule reacted, nHA equivalent weight would be 510.8 g/eq OH, and if both primary NCO groups from the same LTI molecule reacted, nHA equivalent weight would be 1013 g/eq OH.

Discussion

Figure 4.5 demonstrates the possible chemical reactions associated with nHA-LTI grafting. Allophonate reaction between urethane and isocyanate group must occur at the surface of nHA, which is inconsistent with XPS data. Furthermore, allophonate reaction requires high temperature greater than 110 °C, thus is not expected to occur at room temperature.[19] Water reaction involves two isocyanate groups and can happen at the surface of nHA as well as in the bulk. Since LTI was in large excess in the reaction mixture, it is expected that water reaction occurred mainly in the bulk, which is in consistent with the XPS data and titration data. FTIR spectra proved the formation of urea bond. Taken together, water reaction is likely to be the main side reaction associated with nHA-LTI grafting.

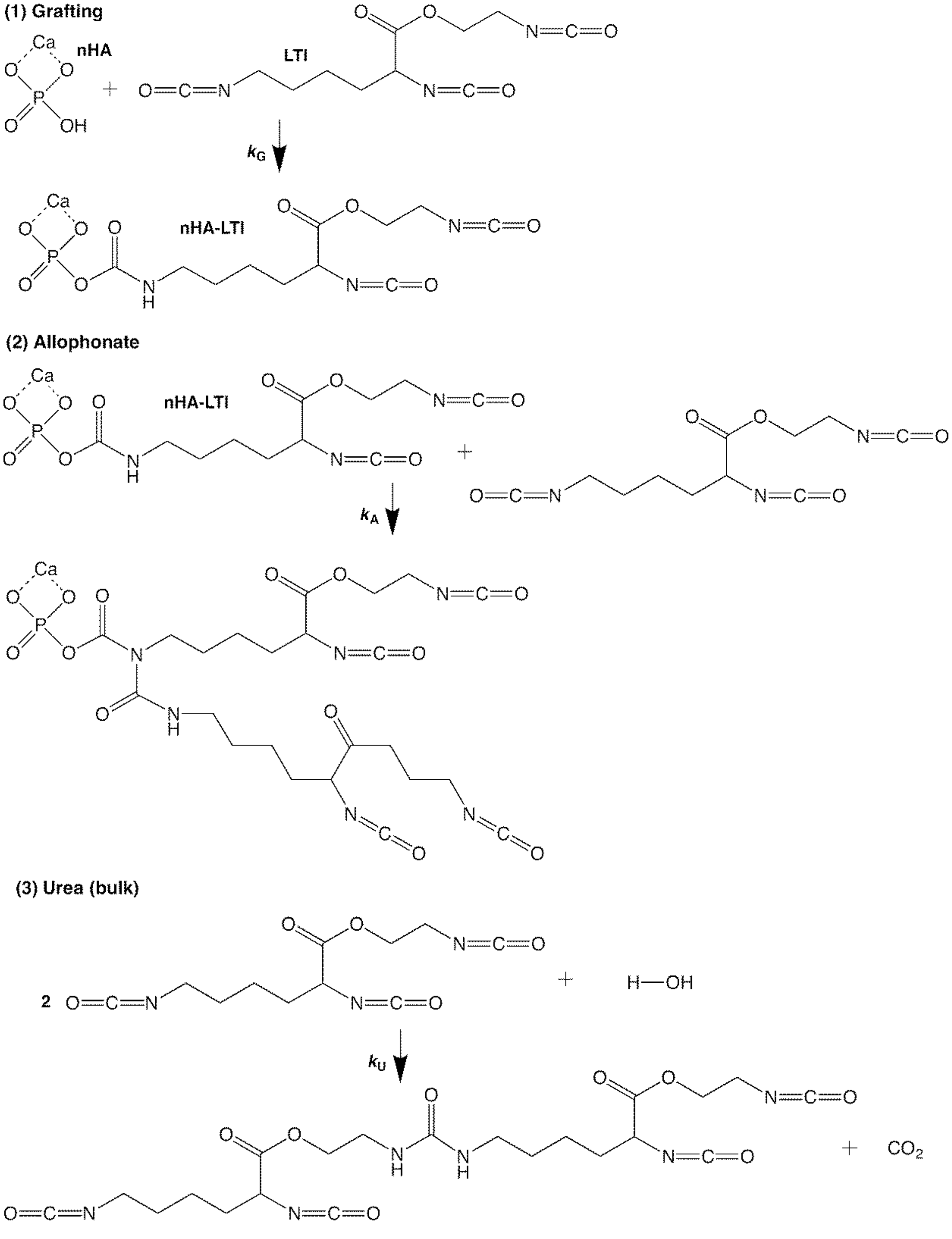

Figure 4.5 Possible chemical reactions associated with nHA-LTI grafting reaction.

The direct way to measure nHA equivalent weight is to measure the OH number of nHA by titration. However, since the reaction involves liquid and solid phase, titration for OH number doesn't work well. We found %NCO measurement of the nHA-LTI/LTI prepolymer provided consistent and reliable results, thus we used it to calculate back the equivalent weight of nHA.

The equivalent weight calculation from titration result is based on the assumption that ξ_{OH} has reached 100%, which is validated by the fact that the %NCO of the mixture remained stable for 44 days. The equivalent weight calculated from titration result falls in the same range as that calculated from XPS results, indicating that the assumption is valid. It also falls between the two values calculated from XPS results under different situations (510.8<762.07<1013), suggesting that in the reaction, some LTI molecules had one primary NCO group reacted, and some had both primary NCO groups reacted. XPS calculation doesn't require the assumption of 100% conversion, but the deviation in measurement seems to be large, thus is not recommended to be used alone for calculation of equivalent weight, but is a good marker for indicating if the conversion has reached 100% or the mixture remains stable.

One limitation of this method is that the calculation is based on only one data point, which can introduce error. Alternatively, equivalent weight could be extrapolated by measuring %NCO at 100% conversion at different nHA loadings. The calculation method is as follows:

Let H = equivalent weight of nHA, and I = equivalent weight of LTI. When H grams of nHA react with I grams of LTI, all the reactive groups react, and the % NCO of the mixture=0. At this point, assume Z grams of additional LTI was added to the system, thus the % NCO of the mixture is

$$\%\text{NCO}=\frac{\text{Mass due to unreacted NCO}}{\text{Total mass}}=\frac{\dfrac{\text{Z g of additional LTI}}{\text{I g LTI/eq NCO}}\times 42\text{ g/eq NCO}}{(H+I+Z)g} \tag{4.11}$$

The nHA wt% in the reaction mixture is

$$\text{w=nHA wt\%=}\frac{H}{H+I+Z} \tag{4.12}$$

Substituting (12) into (11), the % NCO of nHA-LTI/LTI mixture is

$$\%NCO = -\frac{42(H+I)}{H \times I} w + \frac{42}{I} \tag{4.13}$$

Since H and I are both constants, %NCO as a function of nHA wt% should fit a straight line, and the equivalent weights of nHA and LTI can both be calculated using the slope and intercept from the straight line.

The other limitation of this method is that both primary NCO groups of the same LTI molecule can react with surface OH groups of nHA. The nHA equivalent weight calculation from XPS and titration results suggests that both primary NCO groups can react. To simplify the calculation, linear monoisocyanates with low steric hindrance could be used to graft nHA particles to verify the equivalent weight calculation presented in this chapter.

The equivalent weight of nHA could also be calculated from the %NCO of the grafted nHA particles. A linear diisocyanate with low steric hindrance is recommended to react with nHA for this method. When the conversion of the grafting reaction reaches 100%, particles recovered from the reaction mixture could be titrated to measure %NCO. Assume one NCO group of the diisocyanate is grafted and the other one is unreacted.

$$\text{\%NCO of grafted particles} = \frac{\text{Mass due to unreacted NCO}}{\text{Total mass}} = \frac{42\text{ g}}{\mathrm{w}_{\mathrm{OH}} + 2 \times \mathrm{w}_{\mathrm{NCO}}} \tag{4.14}$$

In **Equation 14**, $\mathrm{w}_{\mathrm{NCO}}$ is the equivalent weight of the diisocyanate, which could be calculated from the molecular structure of the diisocyanate, and w_{OH} is the equivalent weight of nHA.

$$\mathrm{w}_{\mathrm{OH}} = \frac{42\text{ g}}{\text{\%NCO of grafted particles}} - 2 \times \mathrm{w}_{\mathrm{NCO}} \tag{4.15}$$

Since titration of solid particles is difficult, the %NCO of the grafted particles could be measured by re-dispersing grafted particles into fresh isocyanate and titrating the %NCO of the redispersed mixture.

Since all of the surface hydroxyl groups of grafted particles should have already reacted, the %NCO of grafted particles could be calculated based on the dilution effect.

$$\begin{aligned}
&\text{\%NCO of redispersed mixture}=\frac{\text{Mass due to unreacted NCO}}{\text{Total mass}}\\
&=\frac{\text{Mass due to unreacted NCO of isocyanate+mass due to unreacted NCO of grafted particles}}{\text{Total mass}} \qquad (4.16)\\
&=\frac{42\text{ g/eq NCO}\times\dfrac{\text{Isocyanate mass}}{\text{Isocyanate equivalent weight}}+\text{mass due to unreacted NCO of grafted particles}}{\text{Total mass}}
\end{aligned}$$

From **Equation 16**, the mass due to unreacted NCO of the grafted particles could be calculated, and %NCO of grafted particles could be calculated using the following equation:

$$\text{\%NCO of grafted particles}=\frac{\text{Mass due to unreacted NCO of grafted particles}}{\text{Total mass of grafted particles}} \qquad (4.17)$$

If the equivalent weight of nHA is known, the %NCO of the nHA-LTI/LTI prepolymer with different nHA wt% can be predicted, which further determines the amount of nHA-LTI/LTI needed for the crosslinking reaction with the polyester component to fabricate the final nHA-PEUR nanocomposite. This approach allows for manipulation of nHA wt% in the nHA-LTI/LTI prepolymer to satisfy other requirements in manufacturing process, such as requirements for viscosity and volume ratio of the prepolymer and the polyester component in the crosslinking reaction.

Conclusions

This study reveals that the urethane reaction between surface hydroxyl groups of nHA and LTI competes with the urea reaction between LTI and water in the bulk. The nHA-LTI grafting reaction must be performed under dry conditions to prevent urea reaction. When the grafting reaction is performed under dry condition without catalyst, the %NCO of the reactive mixture dropped initially and reached steady state after a few days, suggesting the grafting reaction was complete and the resulting nHA-LTI/LTI prepolymer was stable. The equivalent weight of nHA is 762.07 g nHA/eq OH. This information will aid in the manufacture of nHA-LTI/LTI prepolymer and nHA-PEUR nanocomposites for bone repair.

References

1. Alves, N.M., et al., *Designing biomaterials based on biomineralization of bone.* Journal of Materials Chemistry, 2010. **20**(15): p. 2911-2921.
2. Webster, T.J., et al., *Specific proteins mediate enhanced osteoblast adhesion on nanophase ceramics.* Journal of Biomedical Materials Research, 2000. **51**(3): p. 475-483.
3. Webster, T.J., et al., *Enhanced functions of osteoblasts on nanophase ceramics.* Biomaterials, 2000. **21**(17): p. 1803-1810.
4. Webster, T.J., et al., *Enhanced osteoclast-like cell functions on nanophase ceramics.* Biomaterials, 2001. **22**(11): p. 1327-1333.
5. Goonaseker, C.S., et al., *Attachment of poly(acrylic acid) to 3-aminopropyltriethoxysilane hydroxyapatite.* Journal of Materials Chemistry B, 2013. **1**(42): p. 5842-5852.
6. Harmata, A.J., et al., *Investigating the effects of surface-initiated polymerization of epsilon-caprolactone to bioactive glass particles on the mechanical properties of settable polymer/ceramic composites.* Journal of Materials Research, 2014. **29**(20): p. 2398-2407.
7. Supova, M., *Problem of hydroxyapatite dispersion in polymer matrices: a review.* J Mater Sci Mater Med, 2009. **20**: p. 1201-1213.
8. Tanaka, H., et al., *Surface Structure and Properties of Calcium Hydroxyapatite Modified by Hexamethyldisilazane.* J Coll Interfac Sci, 1998. **206**: p. 205-211.
9. Liu, Q., et al., *Surface modification of nano-apatite by grafting organic polymer.* Biomaterials, 1998. **19**: p. 1067-72.
10. Wang, Z.L., et al., *Enhanced in Vitro Mineralization and in Vivo Osteogenesis of Composite Scaffolds through Controlled Surface Grafting of L-Lactic Acid Oligomer on Nanohydroxyapatite.* Biomacromolecules, 2016. **17**(3): p. 818-829.
11. Dong, G.C., et al., *A study on grafting and characterization of HMDI-modified calcium hydrogenphosphate.* Biomaterials, 2001. **22**(23): p. 3179-3189.
12. Lee, H.J., et al., *The effect of surface-modified nano-hydroxyapatite on biocompatibility of poly(epsilon-caprolactone)/hydroxyapatite nanocomposites.* European Polymer Journal, 2007. **43**(5): p. 1602-1608.
13. Jiang, L.Y., et al., *Effect of l-lysine-assisted surface grafting for nano-hydroxyapatite on mechanical properties and invitro bioactivity of poly(lactic acid-co-glycolic acid).* Journal of Biomaterials Applications, 2016. **30**(6): p. 750-758.
14. Dong, S.J., et al., *Preparation, Surface Properties and Biological Activity of the Composite of Poly (lactide-co-glycolide) and Bioglass Nanoparticles Surface Grafted with Poly(L-lactide).* Chemical Journal of Chinese Universities-Chinese, 2009. **30**(5): p. 1018-1023.
15. Fan, R.R., et al., *Preparation and properties of g-TTCP/PBS nanocomposites and its in vitro biocompatibility assay.* International Journal of Biological Macromolecules, 2013. **59**: p. 227-234.
16. Jiang, L.Y., et al., *Effect of n-HA with different surface-modified on the properties of n-HA/PLGA composite.* Applied Surface Science, 2012. **259**: p. 72-78.
17. Jiang, L.X., et al., *Effect of a new surface-grafting method for nano-hydroxyapatite on the dispersion and the mechanical enhancement for poly(lactide-co-glycolide).* Express Polymer Letters, 2014. **8**(2): p. 133-141.
18. Qiu, X.Y., et al., *Surface-modified hydroxyapatite linked by L-lactic acid oligomer in the absence of catalyst.* Journal of Polymer Science Part a-Polymer Chemistry, 2005. **43**(21): p. 5177-5185.
19. Zharkov, L.I.K.a.V.V., *Spectral Studies On the Structure of Polyurethane Elastomers.* Journal of Applied Spectroscopy, 1966. **5**(1): p. 95-97.

CHAPTER 5 - SETTABLE POLYMER/CERAMIC COMPOSITE BONE GRAFTS STABILIZE WEIGHT-BEARING TIBIAL PLATEAU SLOT DEFECTS AND INTEGRATE WITH HOST BONE IN AN OVINE MODEL

Introduction

Intra-articular fractures involve a weight-bearing joint and are challenging to treat. Specifically, the fracture is subjected to repetitive, dynamic physiological loading from daily activities, thus articular congruency may be difficult to be achieved and maintained.[1] Maintain articular congruency requires extensive open reduction and internal fixation approaches along with subchondral grafting, which is associated with high rates of complications.

An ideal grafting material for treatment of these fractures rapidly sets after implantation, provides bone-like strength that helps to stabilize and maintain the articular congruency of the fracture without the need for fixation systems, stimulates osteogenic differentiation and new bone formation, and resorbs at a rate aligned with patient biology to maintain osseous integrity as the graft is gradually replaced by bone. However, biomaterials that both stabilize and promote healing of intra-articular fractures are not currently available. Poly(methyl methacrylate) (PMMA) bone cements exhibit mechanical properties greater than those of trabecular bone, providing adequate strength to stabilize the fractures.[2, 3] However, PMMA cements are biologically inert and do not integrate with host bone, which causes long-term problems.[4-8] Calcium phosphate cements (CPCs) have been shown to be osteoconductive, and are resorbable *in vivo*.[9-15] However, in highly loaded sheep tibial plateau defects, CPC cements reveal cracks within the cement and gaps between the host bone and the implants, thus are suggested to be used only as filler material or be stabilized with extra hardware.[16] Biphasic CPCs reinforced with polymeric or metallic materials show enhanced mechanical properties, but there are limited studies evaluating remodeling of biphasic CPCs in bony defects.[17-21]

Injectable, settable and biodegradable poly(ester-urethane) (PEUR)/ceramic composite bone grafts incorporating allograft bone or ceramic particles have been reported to set *in situ* comparable to CPCs, support bone remodeling and degrade to nontoxic compounds.[22-26] However, the mechanical properties of the ceramic/polymer composites decrease with increasing ceramic content, and PEUR undergo autocatalytic hydrolytic degradation that makes it difficult to match the rate of graft resorption to bone formation and remodeling.[27, 28] We have previously reported that surface-initiated polymerization of ε-caprolactone to bioactive glass (BG) particles enhances the compressive strength of the lysine triisocyanate (LTI)-derived PEUR/BG composites up to 10 folds, and torsional strength of resulting PEUR/BG composites exceeds that of human trabecular bone. The resulting PEUR/BG composites support cellular infiltration and remodeling.[29] In another study, surface grafting LTI to nanocrystalline hydroxyapatite particles (nHA-LTI) enhances the dispersion of nHA in the PEUR matrix, resulting in enhanced compressive strength and four-point bending strength, which are comparable to that of PMMA cements. Moreover, the nHA-PEUR composites enhance osteoblast mineralization, and undergo osteoclast-mediated resorption *in vitro*.[30]

In this study, we incorporated ε-caprolactone polymerized BG particles with nHA-PEUR nanocomposites together with ceramic mini-granules (MASTERGRAFT®, MG, 85% β-tricalcium phosphate and 15% hydroxyapatite) to make settable, resorbable polymer/ceramic composite bone grafts, and tested them in two models: stringent weight-bearing sheep tibial plateau defects and non-weight-bearing femoral plug defects, adapted from previous studies.[16] Two questions are to be investigated: 1) do the grafts maintain mechanical stability while being resorbed and incorporated with host bone, and 2) how does mechanical loading affect graft remodeling.

Experimental

Materials

Lysine triisocyanate (LTI) was purchased from Jinan Haohua Industry Co., Ltd (Jinan, China), and was purified by refluxing with decolorizing carbon (Fisher Scientific) in tert-butyl methyl ether (TBME, Across-Organic) at 63°C for 22 hours before use. Polycaprolactone triol (Mn = 300 Da) and nHA particles were purchased from Sigma-Aldrich, and were dried under vacuum at 80°C for 48 hours before use. Iron acetylacetonate (FeAA) catalyst, 3-amino-propyl-triethoxysilane (APTES), and ε-caprolactone were purchased from Sigma-Aldrich and used as received. Magnesium sulfate and stannous octoate ($Sn(Oct)_2$) were purchased from Thermo Fisher Scientific. Melt-derived 45S5 bioactive glass (BG) was purchased from Mo-Sci Corporation (Rolla, MO). MasterGraft particles (MG) were supplied by Medtronic (Memphis, TN), and were ground to 100-300 µm diameter using a mortar and pestle. BG and MG particles were cleaned by sonicating with 95% acetone for 5 minutes, triple rinsed with DI water, and vacuum dried before use.

Surface-initiated polymerization of ε-caprolactone on BG

The method for surface-initiated polymerization of ε-caprolactone on BG is described elsewhere.[29] Briefly, clean BG particles were stirred in APTES solution (2 µM in 9:1 (v/v) ethanol:DI water) for 5 hours at room temperature, followed by annealing at 100°C for 1 hour. Before polymerization, ε-caprolactone was dried in the presence of magnesium sulfate. Silanized BG particles were reacted with a mixture comprising 0.001M $Sn(Oct)_2$ in dried ε-caprolactone at weight ratio of 1:3.679 at 110°C for 24 hours. The PCL grafted BG particles were extracted and washed with chloroform and dried at 40°C under vacuum.

Synthesis of nHA-LTI prepolymer

nHA-LTI prepolymer was synthesized by mixing nHA particles (65 wt%) with LTI (35 wt%) in the presence of FeAA catalyst (5% solution in ε-caprolactone) at weight ratio of 1:0.0055 for 10 minutes and kept at 50°C for 3 hours to yield a viscous liquid.[30]

Synthesis of polymer/ceramic composite bone grafts

Polymer/ceramic composite bone grafts were made by first mixing polycaprolactone triol (PCL 300, Mn = 300Da) with FeAA catalyst (the overall FeAA catalyst concentration was 0.5 pphp in PCL 300, taking the amount of FeAA in nHA-LTI prepolymer into account) until homogenous. The PCL 300/FeAA mixture was then mixed with MG (55 wt%) or a blend of BG (37.5 wt%) and MG (22.5 wt%) particles until the surface of the particles was uniformly covered by PCL 300/FeAA. Finally, this mixture was mixed with nHA-LTI prepolymer by hand for another 30 seconds. The ratio of NCO:OH was 140:100. The resulting composite bone grafts were denoted as MG/nHA-PEUR grafts and BGMG/nHA-PEUR grafts, respectively.

In vitro characterization of polymer/ceramic composite bone grafts

After 30 seconds of final mixing the resulting graft is a moldable putty that can be molded to the defect space prior to *in situ* cure. Working time is defined as the time at which the grafts become difficult to mold and was measured by hand. Tack-free time was measured by poking the grafts with a spatula and defined as the time at which the grafts no longer stuck to it. The tack-free time approximates the setting time for bone cements.[31]

Compressive Mechanical Properties

Cylindrical specimens (n=3) were used for all mechanical testing. Composites were mixed as described above and cured in a 6 mm diameter tube under a 0.96 kg weight for 24 hours. Crosslinked composites were then cut to a height of 12 mm using a Buehler IsoMet Low Speed Saw ensuring to maintain flat, parallel surfaces. Specimens for quasi-static compressive testing were hydrated in water for 24 hours at 37 °C prior to testing to emulate *in vivo* conditions. Wet specimens were compressed at a rate of 25 mm min^{-1} using an MTS 858 Bionix Servohydraulic Test System. Compressive modulus, yield strength, and yield strain were calculated from the resulting engineering stress-strain curve.

Fatigue testing was performed as described previously.[32] The MTS was equipped with cylindrical platens having a diameter only slightly larger than the specimen. After loading the hydrated specimen and compressing the platens to ~0 N force, an MTS extensometer (634.31F-24) was attached to both platens by affixing the knife edges of the extensometer using tightly fitted O-rings (**Figure 5.2A**). Hydration was maintained throughout the testing by a constant drip supplied from a water bath heated to 37 °C. Specimens were wrapped in gauze to disperse water and ensure the entire sample stayed wet.

Fatigue properties were investigated by cyclically loading specimens to a maximum stress of 5 MPa (minimum ~0.3 MPa to maintain contact) at a frequency of 5 Hz (**Figure 5.2B**). Each group was tuned to ensure the desired load was reached consistently throughout testing. The same proportional and integral terms were used for the entire group. Force and strain were recorded for every 500th cycle at an acquisition frequency of 200 Hz. Testing was stopped when runout or greater than 3.5% strain was reached. Runout was considered to be 10^6 cycles for this study. Compressive fatigue failure was defined by either of two principles: 1) 1% creep deformation or 2) 3% increase in strain. Creep deformation was measured by comparing the minimum strain value of each cycle to that of the initial cycle recorded.

In vivo sheep study

Eight sheep weighing 57-62 kg were used for *in vivo* animal study. Two kinds of bony defects were prepared in each posterior extremity. Two non-weight-bearing femoral plug defects with 8 mm diameter by 16 mm depth were created on the medial and lateral distal femoral condyles of each posterior extremity. For weight-bearing tibial plateau defect, a single slot defect was created proximal to the patella tendon underneath the tibial plateau. The tibial plateau defects were 6 mm high and to a depth of approximately 50% of the total anterior to posterior tibial depth. Each of the defects was filled with one of the two grafts, BGMG/nHA-PEUR or MG/nHA-PEUR, which were prepared separately as described previously. Each sheep received both grafts in separate extremities, and the placement of grafts was alternated. For example, one sheep had BGMG/nHA-PEUR grafts in the left posterior extremity and MG/nHA-PEUR grafts in the right posterior extremity, and the other one had BGMG/nHA-PEUR in the right and MG/nHA-PEUR in the left. The animals remained in a sling for 3 days post operatively before transitioned to weight bearing as tolerated.

Animals were euthanized at 16 weeks and femurs and tibias were harvested. Micro-computed tomography (µCT) was performed with voxel size of 24.2 µm and analyzed at a threshold of 237. Sheep femurs and tibias were fixed in 10% formalin for 2 weeks, dehydrated in a series of ethanol solutions, and embedded in poly(methyl methacrylate). An Exakt band saw was used to cut 200-µm sagittal sections from the center of the defects that were then ground (40-70 µm) and polished using an Exakt grinding system. The resulting sections were stained with Sanderson's Rapid Bone stain, counterstained with van Gieson, and imaged under a light microscope. For histomorphometry analysis, the defects were divided into eight rectangular regions with 1 mm height and widths one-half of the total depths of the defects **(Figure 5.8A)**. The regions were numbered from the center of the defects, indicating their distance from the central line. For tibial plateau defects, negative numbers indicate regions above the central line and positive numbers indicate regions below the central line. Only bottom regions of the early tibial plateau samples were analyzed due to fracturing of the upper region. Area Bone%, MG%, nHA-PEUR% and BG% were measured for each region at early and late time points using Metamorph$^{®}$ software. Specifically, for MG%

and nHA-PEUR% measurement, overexposed images were taken in order to distinguish them from the graft bulk.

Dynamic Histomorphometry

The animals received different fluorochromes at the following time points: calcein green at 4 weeks, xylenol orange at 8 weeks, and oxytetracycline at 15 weeks. Sections were prepared as described above and imaged under fluorescent microscope using a DAPI/FITC/Texas Red filter (Chroma, Bellows Falls, VT).

Statistical analysis

Student t test was applied to determine if there was significant difference in mechanical properties between the groups. For histomorphometry analysis, paired t test was applied to determine if there was significant difference between femur and tibia.

Results

In vitro characterization of polymer/ceramic composite bone grafts

The working time for MG/nHA-PEUR grafts and BGMG/nHA-PEUR grafts was 2.08±0.07 minutes and 2.26±0.11 minutes, respectively (**Table 5.1**). Both groups of grafts became tack-free instantly after working time. The particles prevented the material from sticking to the spatula. Both groups of grafts rapidly hardened within 20 seconds after working time, resulting in rigid bulk solid.

Table 5.1 Study design and handling properties of settable bone grafts

Treatment Group	Ceramic	Working time (min)	Setting time (min)	16 weeks	
				Tibia	Femur
BG/MG	50 vol%BG/50 vol% MG	2.26±0.11	2.26±0.11	8	8
MG	MG	2.08±0.07	2.08±0.07	8	8

Mechanical samples were prepared by the same procedure and cured in cylindrical tubes for testing. The results of all mechanical testing are presented in **Table 5.2**. The modulus, yield strength, and strain at yield were not significantly different between the 2 groups (**Figure 5.1**). All specimens went to runout when cyclically loaded to 5 MPa. **Figure 5.2C-D** show representative hysteresis loops for the first (black) and last (gray) recorded cycle (N= cycle number) for MG/nHA-PEUR (**Figure 5.2C**) and BGMG/nHA-PEUR (**Figure 5.2D**) grafts. Creep strain (minimum strain of cycle – minimum strain of first recorded cycle) experienced by the grafts increased drastically the first 50,000 cycles, but reached somewhat of a plateau as the tests went on (**Figure 5.2E-F**). Neither group experienced greater than 0.20% creep after 1,000,000 cycles. These data verify that the specimens did not fail before runout was reached.

Table 5.2 Static and dynamic mechanical properties of settable bone grafts

Group	Static Compressive Properties	Compressive Fatigue Life

	Modulus (MPa)	Yield Strength (MPa)	Yield Strain (%)	1% Creep Deformation	3% Strain
MG	1330 ± 130.0	81.6 ± 5.72	8.37 ± 0.546	Runout	Runout
MG/BG	1520 ± 92.2	74.0 ± 3.56	7.17 ± 0.548	Runout	Runout

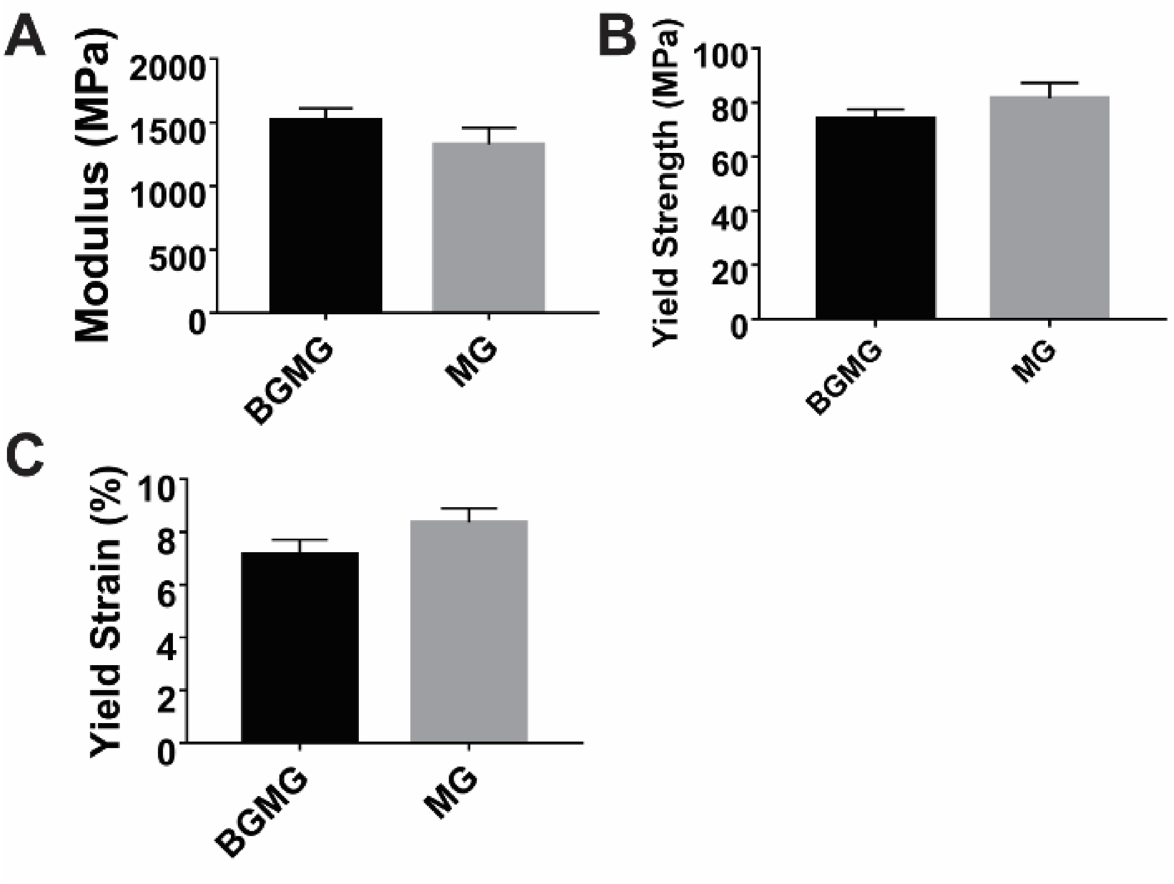

Figure 5.1 Compression properties were not significantly different between the two grafts. (A) Modulus, (B) Yield strength, (C) Strain at yield. Error bars stand for standard deviation.

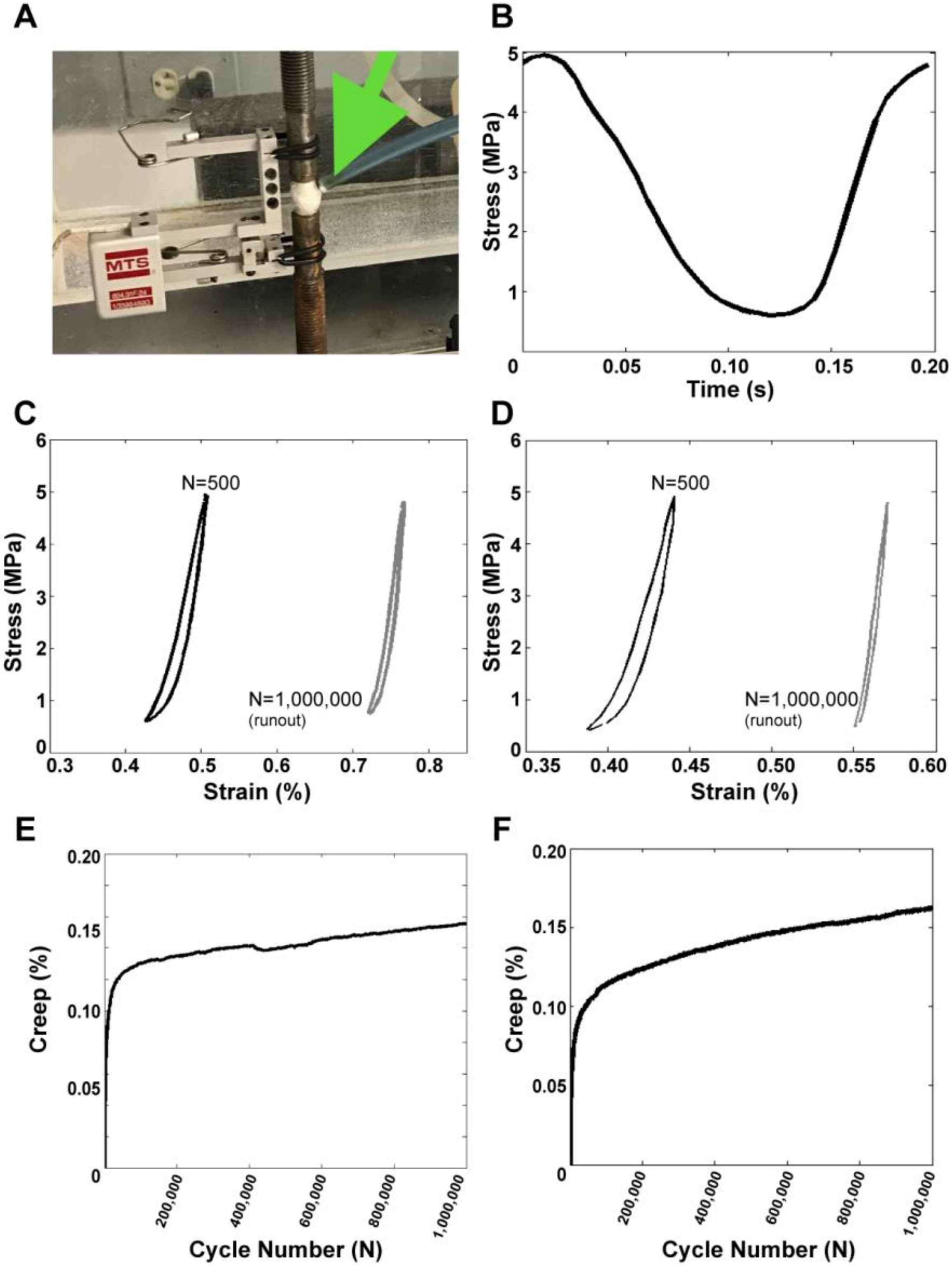

Figure 5.2 Dynamic fatigue properties at 5 MPa applied stress. (A) experimental setup for fatigue testing. Arrow points to water drip to keep the sample wet. (B) samples were cyclically loaded to a maximum

stress of 5 MPa (minimum ~0.3 MPa to maintain contact) at a frequency of 5 Hz. (C-D) representative hysteresis loops for the first (black) and last (gray) recorded cycle (N= cycle number) for MG (C) and MGBG (D) composites. (E-F) Creep strain experienced by the composites increased drastically the first 50,000 cycles, but reached somewhat of a plateau as the tests went on.

Clinical outcomes

CT images were taken immediately following the surgery to reveal the fill of the defects. Both groups completely filled the tibial plateau and femoral plug defects without gaps or voids (**Figure 5.3**). Four of the eight sheep survived to 16 weeks. Two sheep showed shelf fracture above the tibial plateau defect on the BGMG/nHA-PEUR side at 6 and 11 days. Another two sheep presented fractured tibial shelves on the MG/nHA-PEUR side at 18 and 20 days (**Table 5.3**). Diagnostic CT showed no apparent degradation of grafting materials for all cases; however, fractured shelves appeared to be pulled away from the tibial plateau. Additionally, two sheep visibly favored the MG/nHA-PEUR side immediately post-operatively, but their gait was improved after 3 weeks and the animals survived to 16 weeks.

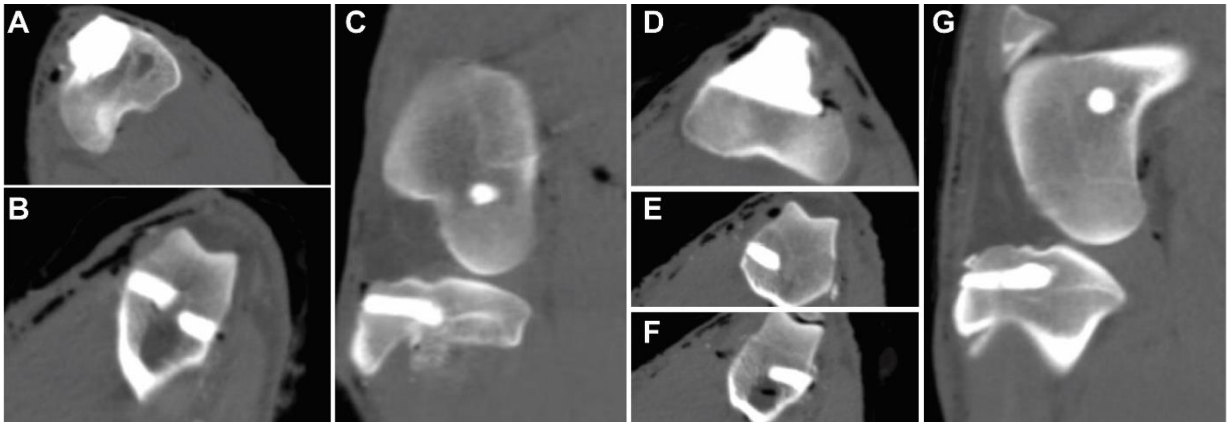

Figure 5.3 CT images at t = 0 showing fill of the defects.(A) transverse view of MG tibial plateau defect. (B) transverse view of MG femoral plug defects. (C) sagittal view of MG tibial plateau and femoral plug defects. (D) transverse view of BGMG tibial plateau defect. (E-F) transverse view of BGMG femoral plug defects. (G) sagittal view of BGMG tibial plateau and femoral plug defects.

Table 5.3 Clinical outcomes

Treatment Group	Stable	Fractured
BG/MG	4/8	4/8
MG	4/8	4/8

Histology analysis at early timepoints

Four sheep were euthanized early after fracture diagnosis and the limbs processed for histology (**Figure 5.4**). Among four MG/nHA-PEUR and four BGMG/nHA-PEUR tibial plateau samples, only one BGMG/nHA-PEUR sample showed significant material degradation. The other seven grafts implanted in tibial plateau defects remained embedded in the defect and completely filled the remaining portion of the defects. In femoral plug defects, all grafts remained intact and completely filled the defects. Histology images (**Figure 5.4B, D**) showed that the interface between the grafts and host bone was well-defined for both tibial plateau and femoral plug defects, suggesting minimal incorporation of the graft with host bone at the early time point. Cells (**Figure 5.4C, D**, blue) were present within host bone near the interface, suggesting that at this early time point, cells were recruited to the fracture site.

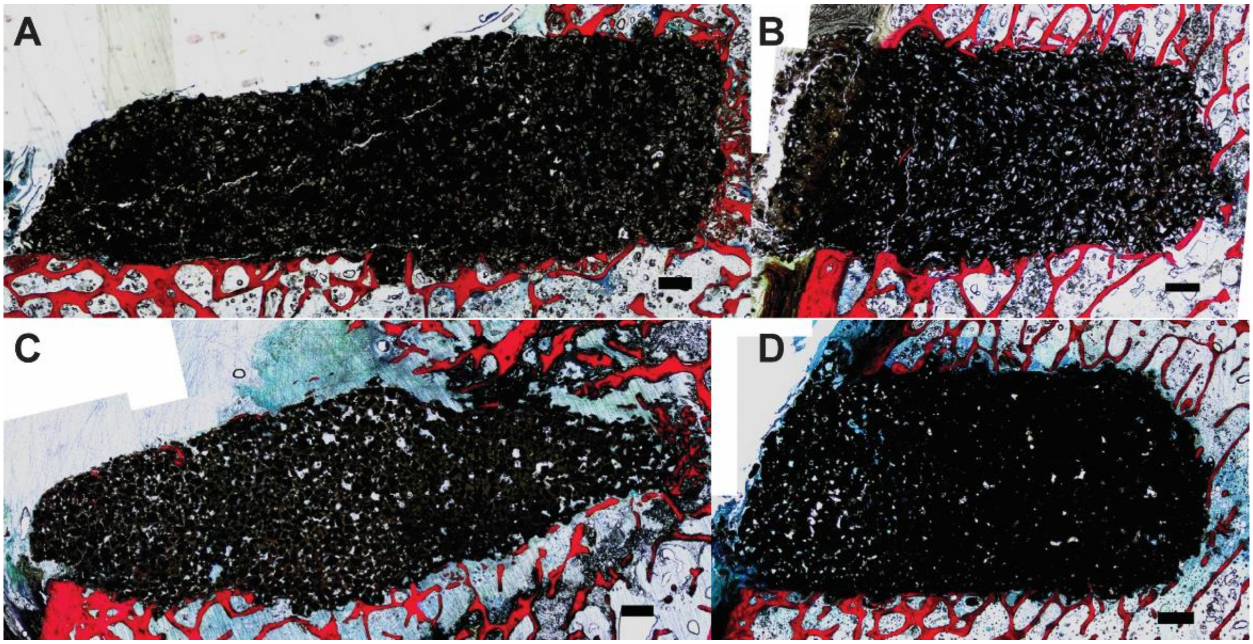

Figure 5.4 Representative histological images of grafts that failed early (Sagittal sections). (A) BGMG tibial plateau defect. (B) BGMG femoral plug defect. (C) MG tibial plateau defect. (D) MG femoral plug defect. Scale bar = 1 mm

MicroCT and histology analysis at 16 weeks

At 16 weeks, BGMG/nHA-PEUR grafts implanted in tibial plateau defects degraded and fragmented (**Figure 5.5A**). There were ~1 mm gaps between the grafts and the host bone. Histology images revealed that the gaps were filled with cells and fibrotic tissue (**Figure 5.6A, E**). The periphery of host bone grew significantly denser in order to compensate for the mechanical loss of the degraded grafts. In contrast, in femoral plug defects, BGMG/nHA-PEUR grafts remained intact, with growth of dense trabecular bone near the interface of the grafts and host bone, indicating that BGMG/nHA-PEUR grafts integrated with host bone (**Figure 5.5B, Figure 5.6 C, G**). MG/nHA-PEUR grafts were stable in both tibial plateau and femoral plug defects (**Figure 5.5 C-D, Figure 5.6 B, F, D, H**). There were no gaps between MG/nHA-PEUR grafts and host bone, and similar trabecular densification was observed at the periphery of the defects. In addition, new bone infiltrated into the grafts and formed on surface of MG particles. No fibrotic tissue was evident between MG particle and newly formed bone.

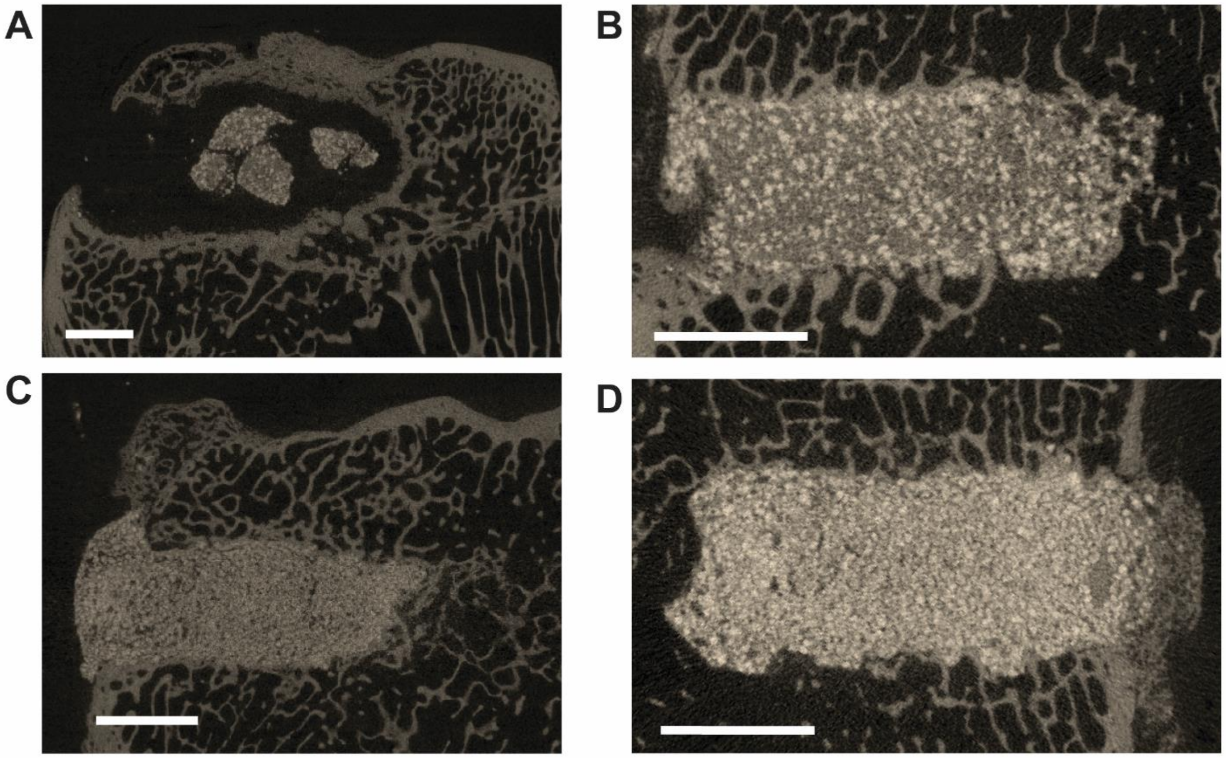

Figure 5.5 Representative microCT images of grafts at 16 weeks (Sagittal view). (A) BGMG tibial plateau defect. (B) BGMG femoral plug defect. (C) MG tibial plateau defect. (D) MG femoral plug defect. Scale bar = 5 mm

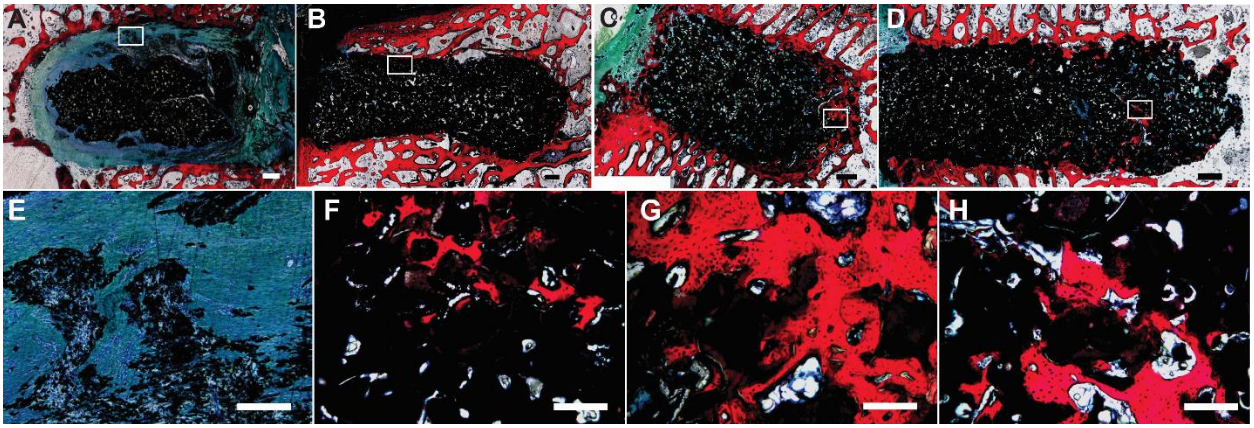

Figure 5.6 Representative sagittal histological sections through the defects at 16 weeks. (A, E) BGMG tibial plateau defect. (B,F) MG tibial plateau defect. (C,G) BGMG femoral plug defect. (D,H) MG femoral plug defect. Scale bar at the top row = 1 mm, scale bar at the bottom row = 250 µm

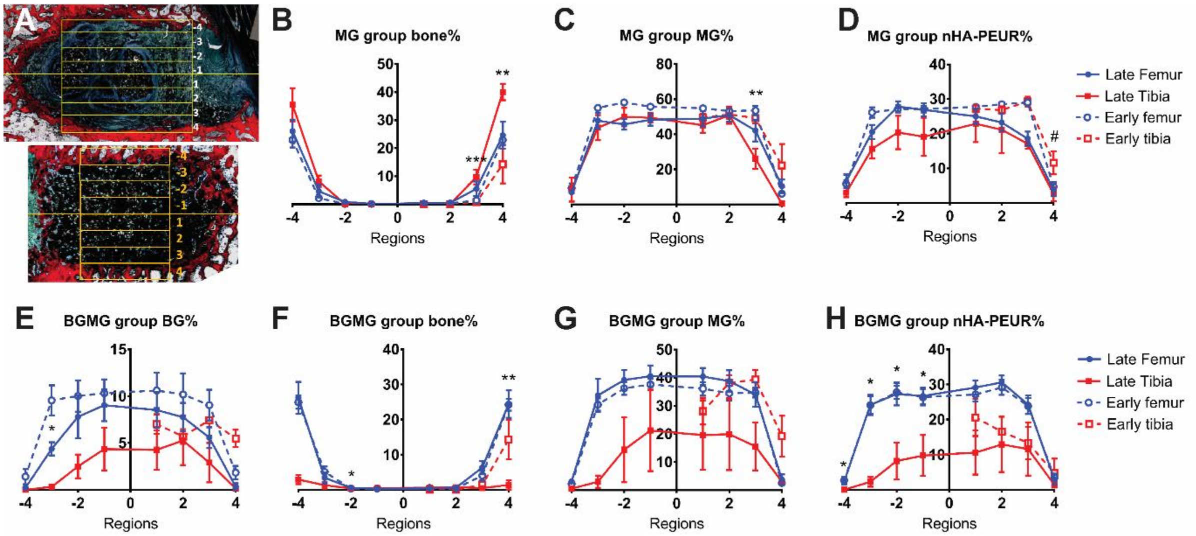

Figure 5.7 (A) Histomorphometry analysis region setup. (B-D) MG group bone%, MG% and nHA-PEUR%. (E-F) BGMG group BG%, bone%, MG% and nHA-PEUR%. Error bars stand for S.E.M. * indicates significant difference between late femur and tibia. # indicates significant difference between early femur and tibia.

In order to compare the rate of new bone formation and graft resorption of the two grafts at weight-bearing and non-weight-bearing sites, histomorphometry analysis was conducted (**Figure 5.7**). Three out of four samples from each group were analyzed. One of the BGMG/nHA-PEUR samples had a collapsed tibial shelf, and one of the MG/nHA-PEUR samples was incompletely filled during surgery . Those samples were excluded from the analysis to ensure the results are representative. Bone% looked similar in early and late femoral plug defects for both BGMG/nHA-PEUR and MG/nHA-PEUR groups, indicating limited new bone formation during the 16 weeks (**Figure 5.7 B, F,** blue lines). For tibial plateau defects, bone% for MG/nHA-PEUR grafts at 16 weeks was higher than that of early time point at regions 3 and 4 (**Figure 5.7B,** red lines). To determine if there was significant difference in bone% between weight-bearing tibial plateau defects and non-weight-bearing femoral plug defects in the same sheep, paired t test was conducted for each region. At early time points, there was no significant difference between bone% in tibial plateau defects and femoral plug defects for MG/nHA-PEUR grafts for any of the regions (**Figure 5.7B**, dashed lines). At 16 weeks, a significant difference in bone% for MG/nHA-PEUR grafts was detected between tibial plateau and femoral plug defects at regions 3 and 4 (**Figure 5.7B,** solid lines). This indicated MG/nHA-PEUR grafts in weight-bearing tibial plateau defects had an enhanced rate of new bone formation during the 16 weeks compared to non-weight-bearing femoral plug defects. This effect was only presented at the bottom interface of the tibial plateau defects. MG% and nHA-PEUR% were measured to evaluate graft resorption. For the MG/nHA-PEUR group, a significant difference in MG% between tibial plateau and femoral plug defects was detected for the late time point at region 3 (**Figure 5.7C,** solid lines). nHA-PEUR% for MG/nHA-PEUR group at region 4 was significantly higher in tibial plateau defects at early time points (**Figure 5.7D**, dashed lines); however, there was no statistical difference at 16 weeks (**Figure 5.7D,** solid lines). These observations indicated that resorption of MG/nHA-PEUR grafts was faster for weight-bearing tibial plateau defects, and the resorption rate at bottom interface of tibial plateau defects was faster than that at the top interface. Bone% for BGMG/nHA-PEUR groups did not change significantly in femoral plug defects during 16 weeks (**Figure 5.7F,** blue lines). However, bone% at the interface of tibial plateau defects at 16 weeks was less than that measured for early time points (**Figure 5.7F,** red lines) and was significantly lower than that of femoral plug defects (**Figure 5.7F,** solid lines). This finding was consistent with the histology image showing large gap at the interface. The height of the tibial plateau defect of late BGMG/nHA-PEUR group was larger than the early BGMG/nHA-PEUR group, indicating the host bone was resorbed or worn away. Due to large errors resulting from graft degradation, no significant difference between tibial plateau and femoral plug defects was detected for BG% and MG% at the early or late time points for BGMG/nHA-PEUR grafts (**Figure 5.7E, G**). nHA-PEUR% for BGMG/nHA-PEUR grafts was significantly lower for late tibial plateau defects compared to femoral plug defects indicating degradation of the BGMG/nHA-PEUR grafts (**Figure 5.7H,** solid lines). In femoral plug defects, MG% and nHA-PEUR% did not change significantly after 16 weeks, which was consistent with the histology finding that the graft remained intact in femoral plug defects after 16 weeks (**Figure 5.7G, H**, blue lines).

Dynamic histomorphometry

The sheep received calcein green (4 week), xylenol orange (8 week) and oxytetracycline (15 week). Oxytetracycline was not visible under a fluorescent microscope, possibly because it was not sufficiently incorporated in the bone before animal sacrifice at 16 weeks. New bone formation was nonlinear at the graft/ host bone interface, thus quantitative analysis was not conducted. Fluorescent images of tibial plateau defects of BGMG/nHA-PEUR group showed immense new bone formation at the periphery of the defect at 8 weeks (xylenol orange, **Figure 5.8A, E**) which was consistent with the notion that the dense bone compensated for the mechanical loss of the degraded graft. In femoral plug defects, layers of new bone were observed at the front edge of host bone for the BGMG/nHA-PEUR group (**Figure 5.8 C, G**), indicating bone remodeling. For MG/nHA-PEUR group, the grafts remained intact in both tibial plateau (**Figure 5.8 B, F**) and femoral plug defects (**Figure 5.8 D, H**), and bone ingrowth was observed at both defects.

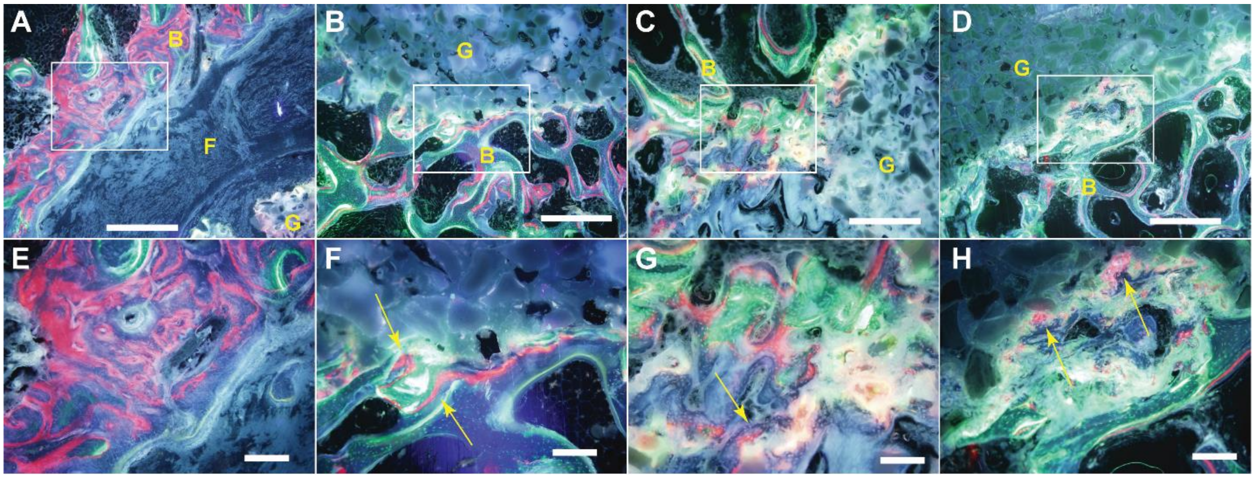

Figure 5.8 Dynamic histomorphometry images (sagittal view) of (A,E) BGMG tibial plateau defect. (B,F) MG tibial plateau defect. (C,G) BGMG femoral plug defect. (D,H) MG femoral plug defect. Arrows point to regions of new bone formation. Scale bar at the top row = 1 mm, scale bar at the bottom row = 250 μm

Discussion

Repair of tibial plateau defects often requires fixation systems, as the graft itself often has inadequate mechanical properties to stabilize the defect throughout remodeling. CPC cements have initial compressive strength comparable to bone, but the bending strength and fatigue resistance is poor. This causes cracks within the cement and gaps between the tibia plateau and the implants, thus CPC cements are suggested for use as a filler material or in conjunction with stabilizing hardware.[16] The goal of this study is to fabricate a degradable polyurethane/ceramic graft with adequate mechanical properties that stabilizes the weight-bearing tibial plateau defect through the remodeling process. Quasi-static compression testing verified the initial bulk mechanical properties of both groups well exceeded those of sheep trabecular bone, which has been reported to have a bulk modulus of 450 ± 90 MPa and yield strength of 17 ± 7 MPa.[33] Fatigue testing was done to investigate the effects of loading on the mechanical properties to ensure the material would not fail after repeated stress *in vivo*. These tests were performed at 5 MPa to simulate the load experienced by bone during daily activities.[1] The materials were not visibly affected by the cyclic loading and did not fail by either definition set forth. Therefore, the materials were considered suitable for implantation in the tibial plateau defect. When implanted in tibial plateau defect without any fixation system, the MG/nHA-PEUR group graft stabilized the defect for 16 weeks, and showed evidence of cellular infiltration, osteoclast mediated resorption, and new bone formation. The material integrated with host bone without gap formation and maintained the mechanical stability and articular congruency of the defect through the early stages of remodeling. These findings highlight the potential of MG/nHA-PEUR composites for treatment of bone defects at weight-bearing sites.

45S5 bioactive glass has been reported to bond with host bone when implanted *in vivo*, and resorbs faster than ceramics in general. The ionic species released from BG stimulate cellular response and material dissolution.[34-37] Thus in this study, we blended BG with MG in the BGMG/nHA-PEUR group, with the hypothesis that BG will enhance rates of new bone formation and graft resorption. Surprisingly, this was not the case in either the tibial plateau or femoral plug defect. In tibial plateau defects, the graft underwent rapid, uncontrolled degradation within the first week, resulting in mechanical loss of the defect and tibial shelf fracture. Although microCT and histology analysis of early fractured samples did not show significant signs of graft degradation, the mechanical properties of the BGMG/nHA-PEUR might have already been impaired. The mechanism of BGMG/nHA-PEUR degradation is unclear. The fact that the graft was stable in femoral plug defect and remained intact through runnout in *in vitro* fatigue tests suggests that the degradation must be related to a combination of mechanical loading and cell interaction with the graft. A previous study investigating polyurethane/BG grafts in a less stringent sheep tibia weight-bearing model revealed that the graft remained intact through 24 months after implantation, with tooth-like new bone ingrowth to the graft.[38] The different observation may result from different formulations of the polymer component, or the difference in mechanical loading - in that model, an empty defect remained stable through a 26 week study.[39] However, in the present study, a negative control, in which no material was used to fill the tibia defects, would have led to catastrophic failures. On the other hand, in femoral plug defects, bone%, MG%, and nHA-PEUR% of BGMG/nHA-PEUR grafts did not change much during 16 weeks, suggesting the rate of graft remodeling was slow. Moreover, the change in bone% of BGMG/nHA-PEUR grafts in femoral plug defect was no larger than that of MG/nHA-PEUR grafts, indicating the incorporation of BG had no benefit compared to MG/nHA-PEUR grafts. This suggests that the osteogenic capacity of the grafts is probably dominated by nHA-PEUR. Previous studies have shown that nHA with grain size less than 100 nm enhances osteogenic differentiation compared to micron-scale HA.[40-48] We have reported that human mesenchymal stem cells (hMSCs) cultured on nHA-PEUR nanocomposites conducted osteogenic differentiation and generated dense sheets of mineralized matrix within 7 days in culture, while on polyurethane matrices without nHA, rat MSCs started to form mineralized nodules on day 21.[30, 49] Taken together, the addition of BG does not improve the osteogenic properties of the graft, and causes rapid degradation of the grafts when exposed to mechanical loading and cellular activity. Thus, BG is unsuitable for incorporation with nHA-PEUR for bone repair and restoration at weight-bearing sites.

Two sheep experienced plateau fracture on the MG/nHA-PEUR side 2-3 weeks after the surgery, the reasoning for which is unclear. One possible explanation is that the animals were kept in a sling system for only 3 days before they were allowed to return to normal weight-bearing activities, which is relatively short compared to other studies.[16] The short period of time might not be enough for the MG/nHA-PEUR grafts to reach full strength, resulting in fracture of the tibia shelf. Future improvement needs to be made to the current model.

Resorption of both BGMG/nHA-PEUR and MG/nHA-PEUR grafts implanted in femoral plug defects and MG/nHA-PEUR grafts implanted in tibia plateau defects appears to be cell-mediated. The interior of the grafts had negligible degradation, while the periphery of the grafts was gradually infiltrated by new bone. Both histology and dynamic histology images showed newly formed bone in direct contact with residual MG particles and expanded from the interface to interior of the grafts through the interspace between MG particles while resorbing the nHA-PEUR polymer. This resorption pattern of the grafts is similar to that of the biphasic CPC cement consisting of dicalcium phosphate dehydrate (DCPD) and β-TCP granules, where the DCPD resorbs faster than β-TCP and free β-TCP granules are incorporated within new bone.[16, 50-52] This is also consistent with our previous finding that nHA-PEUR is hydrolytically stable, and degrades in response to reactive oxygen species secreted by osteoclasts during bone remodeling.[30] No resorption gap or fibrous scar formation was observed in these defects, suggesting a creeping substitution process.[16] The resorption pattern of nHA-PEUR is similar to that reported for CPC cements, suggesting that the nHA-PEUR nanocomposites act more like a ceramic.[53] HA resorbs slower than allograft bone, which attributes to the relatively slow remodeling rate of the grafts.[53] Investigation on a less stringent weight-bearing sheep model has revealed fast integration of nHA/silica gel cements with host bone within 12 weeks, possibly due to fast degradation of the silica gel, but a plateau was reached after 12 weeks where no significant increase in new bone formation or cement resorption was observed.[39] In a dog study using the same model, only a small portion of Norian CPC cement was resorbed during the first 16 weeks, which is similar to this present study. However, by 32 weeks and 72 weeks, a substantial volume of CPC cement was resorbed and replaced by trabecular bone, and vascular penetration started at 32 weeks.[53] In this present study, no vascular formation was observed.

The difference in graft remodeling rates between tibial and femoral defects has been reported. Possible explanations include mechanical force, surface to volume ratio of the defects, and physiological factors.[53] In non-weight-bearing studies, it has been reported that calcium phosphate cements and HA cements remodel faster in femoral models than tibia models, possibly due to difference in cell density and blood flow.[52, 54] A controlled loading experiment has shown that mechanical stimuli associated with physiological stresses improved incorporation and remodeling of morsellized bone graft in goat femurs.[55] Another study has revealed that surface coating of ceramic improved osseointegration of alumina in a load-bearing sheep tibia defect model but not in a non-load-bearing drill hole defect.[56] In a canine model, resorption of CPCs in a tibial plateau defect was faster than observed in a femoral plug defect.[53] The present study reveals a significant difference in remodeling rates of the grafts between the tibia and femur, and also demonstrates the difference in graft remodeling rates between top interface and bottom interface within the same tibia plateau defect. A previous study using a similar tibial plateau model with a plate in the tibia to make it non-weight-bearing has shown that the lower resorption zone of the tibia brushite/β-TCP graft was wider with more new bone formation and a larger cell population compared to the upper resorption zone, but no statistical evaluation was carried out.[52]

Among the four fractured tibial plateau defects, three fractured on the posterior side of the tibia shelf. The other defect was misshaped and the tibia shelf fractured at the thinnest point in the middle. This fracture site is consistent with the reported weakest site where a discontinuity of the bone architecture occurs, suggested by an *ex vivo* experiment.[57] The cruciate ligaments exert an axial force on the tibia plateau which may have caused dislocation of the fractured shelf.

The fast setting time and handling properties of the grafts in the present study are superior to PMMA cements. The preparation of current PMMA cements involves mixing a liquid phase with powder and waiting for the viscosity of the system to become workable. Once the polymerization process of PMMA is initiated, the workable time is very limited. Failure to place PMMA cements within the working time results in leakage of toxic monomer to surrounding tissue and inadequate fill of the defect.[58] The grafts in the present study can be molded by hand immediately after mixing and placed into the defect at any time before the setting time. These materials harden instantly without releasing toxic molecules that could harm the surrounding host tissue. However, the graft is nonflowable, which makes it hard to fill defects with irregular shape, for example, a jagged shape.

Conclusion

MG/nHA-PEUR composites maintain stability at both non-weight-bearing and weight-bearing sites. MG/nHA-PEUR composites remodel significantly faster at the weight-bearing site compared to the non-weight-bearing site, and the rate of remodeling at the bottom interface of a tibial plateau defect is faster than that of the top interface. Mechanical loading at the anatomic site dramatically affects graft remodeling. BGMG/nHA-PEUR grafts undergo controlled remodeling in non-weight-bearing femoral plug defects but resorb rapidly and are infiltrated by fibrous tissue at weight-bearing tibia plateau sites. These findings led to the elimination of BG in PURs for weight-bearing applications.

MG/nHA-PEUR grafts provide favorable handling properties, adequate mechanical stability through the early remodeling phases, integrate with host bone at 16 weeks without formation of a resorption gap or fibrous tissue, stimulate new bone formation and are resorbed by osteoclasts. These findings highlight the potential of MG/nHA-PEUR composites for treatment of bone defects at weight-bearing sites.

References

1. Ramakrishna, S., et al., *Biomedical applications of polymer-composite materials: a review.* Composites Science and Technology, 2001. **61**(9): p. 1189-1224.
2. ISO, *Implants for Surgery-Acrylic resin cements*. 2002.
3. Kuehn, K.-D., *Bone Cements*. 2000, Berlin: Springer.
4. Aamodt, A., et al., *Documentation of hip prostheses used in Norway - A critical review of the literature from 1996-2000.* Acta Orthopaedica Scandinavica, 2004. **75**(6): p. 663-676.
5. Bettencourt, A., et al., *Surface studies on acrylic bone cement.* International Journal of Pharmaceutics, 2004. **278**(1): p. 181-186.
6. Savarino, L., et al., *Microstructural Investigation of Bone-Cement Interface*. Journal of Biomedical Materials Research, 1995. **29**(6): p. 701-705.
7. Berry, D.J., et al., *Twenty-five-year survivorship of two thousand consecutive primary Charnley total hip replacements - Factors affecting survivorship of acetabular and femoral components.* Journal of Bone and Joint Surgery-American Volume, 2002. **84A**(2): p. 171-177.
8. Jasty, M., et al., *The Initiation of Failure in Cemented Femoral Components of Hip Arthroplasties.* Journal of Bone and Joint Surgery-British Volume, 1991. **73**(4): p. 551-558.
9. Bhaskar, S.N., et al., *Biodegradable Ceramic Implants in Bone - Electron and Light Microscopic Analysis.* Oral Surgery Oral Medicine Oral Pathology Oral Radiology and Endodontics, 1971. **32**(2): p. 336-&.
10. Cameron, H.U., I. Macnab, and R.M. Pilliar, *Evaluation of a Biodegradable Ceramic*. Journal of Biomedical Materials Research, 1977. **11**(2): p. 179-186.
11. Constantz, B.R., et al., *Skeletal Repair by In-Situ Formation of The Mineral Phase of Bone.* Science, 1995. **267**(5205): p. 1796-1799.
12. Hubbard, W., *Physiological calcium phosphates as orthopaedic biomaterials*. 1974, Marquette University: Milwaukee, Wisconsin.
13. Manley, M.T., *Calcium phosphate biomaterials. A review of the literature*, in *Hydroxylapatite coatings in orthopaedic surgery*, R.G.T. Geesink and M.T. Manley, Editors. 1993, Raven Press: New York. p. 1-23.
14. Moore, D.C., M.W. Chapman, and D. Manske, *The Evaluation of a Biphasic Calcium-Phosphate Ceramic for Use in Grafting Long-Bone Diaphyseal Defects*. Journal of Orthopaedic Research, 1987. **5**(3): p. 356-365.
15. Nelson, D.G.A., *The Influence of Carbonate on the Atomic-Structure and Reactivity of Hydroxyapatite.* Journal of Dental Research, 1981. **60**: p. 1621-1629.
16. Gisep, A., et al., *Resorption patterns of calcium-phosphate cements in bone.* Journal of Biomedical Materials Research Part A, 2003. **66A**(3): p. 532-540.
17. Dumas, J.E., et al., *Balancing the rates of new bone formation and polymer degradation enhances healing of weight-bearing allograft/polyurethane composites in rabbit femoral defects.* Tissue Eng Part A, 2014. **20**(1-2): p. 115-29.
18. Gay, S., S. Arostegui, and J. Lemaitre, *Preparation and characterization of dense nanohydroxyapatite/PLLA composites.* Materials Science & Engineering C-Biomimetic and Supramolecular Systems, 2009. **29**(1): p. 172-177.
19. Dumas, J.E., et al., *Synthesis of Allograft Bone/Polymer Composites and Evaluation of Remodeling in a Rabbit Femoral Condyle Model.* Acta Biomaterialia, **2010**. **6**: p. 2394–2406.
20. Kruger, R. and J. Groll, *Fiber reinforced calcium phosphate cements -- on the way to degradable load bearing bone substitutes?* Biomaterials, 2012. **33**(25): p. 5887-900.
21. Kruger, R., et al., *Strong and tough magnesium wire reinforced phosphate cement composites for load-bearing bone replacement.* J Mech Behav Biomed Mater, 2013. **20**: p. 36-44.

22. Hafeman, A.E., et al., *Injectable biodegradable polyurethane scaffolds with release of platelet-derived growth factor for tissue repair and regeneration.* Pharmaceutical Research, 2008. **25**(10): p. 2387-2399.
23. Guelcher, S.A., *Biodegradable polyurethanes: Synthesis and applications in regenerative medicine.* Tissue Engineering Part B-Reviews, 2008. **14**(1): p. 3-17.
24. Dumas, J.E., et al., *Synthesis, characterization, and remodeling of weight-bearing allograft bone/polyurethane composites in the rabbit.* Acta Biomaterialia, 2010. **6**(7): p. 2394-2406.
25. Bennett, S., et al., *Initial biocompatibility studies of a novel degradable polymeric bone substitute that hardens in situ.* Bone, 1996. **19**(1): p. S101-S107.
26. Bonzani, I.C., et al., *Synthesis of two-component injectable polyurethanes for bone tissue engineering.* Biomaterials, 2007. **28**(3): p. 423-433.
27. Johnson, A.J.W. and B.A. Herschler, *A review of the mechanical behavior of CaP and CaP/polymer composites for applications in bone replacement and repair.* Acta Biomaterialia, 2011. **7**(1): p. 16-30.
28. Prieto, E.M., et al., *Effects of particle size and porosity on in vivo remodeling of settable allograft bone/polymer composites.* Journal of Biomedical Materials Research Part B-Applied Biomaterials, 2015. **103**(8): p. 1641-1651.
29. Harmata, A.J., et al., *Investigating the effects of surface-initiated polymerization of epsilon-caprolactone to bioactive glass particles on the mechanical properties of settable polymer/ceramic composites.* Journal of Materials Research, 2014. **29**(20): p. 2398-2407.
30. Lu, S., et al., *Resorbable Nanocomposites with Bone-like Strength and Enhanced Cellular Activity.* Journal of Materials Chemistry B, 2017. **5**(22): p. 4198-4206.
31. Dumas, J.E., et al., *Synthesis and Characterization of an Injectable Allograft Bone/Polymer Composite Bone Void Filler with Tunable Mechanical Properties.* Tissue Engineering Part A, 2010. **16**(8): p. 2505-2518.
32. Harmata, A.J., et al., *Compressive fatigue and fracture toughness behavior of injectable, settable bone cements.* Journal of the mechanical behavior of biomedical materials, 2015. **51**: p. 345-355.
33. Mittra, E., C. Rubin, and Y.-X. Qin, *Interrelationship of trabecular mechanical and microstructural properties in sheep trabecular bone.* Journal of biomechanics, 2005. **38**(6): p. 1229-1237.
34. Jones, J.R., *Review of bioactive glass: From Hench to hybrids.* Acta Biomaterialia, 2013. **9**(1): p. 4457-4486.
35. Hoppe, A., N.S. Guldal, and A.R. Boccaccini, *A review of the biological response to ionic dissolution products from bioactive glasses and glass-ceramics.* Biomaterials, 2011. **32**(11): p. 2757-2774.
36. Oonishi, H., et al., *Quantitative comparison of bone growth behavior in granules of Bioglass (R), A-W glass-ceramic, and hydroxyapatite.* Journal of Biomedical Materials Research, 2000. **51**(1): p. 37-46.
37. Talley, A.D., et al., *Effects of Recombinant Human Bone Morphogenetic Protein-2 Dose and Ceramic Composition on New Bone Formation and Space Maintenance in a Canine Mandibular Ridge Saddle Defect Model.* Tissue Engineering Part A, 2016. **22**(5-6): p. 469-479.
38. Ignatius, A., et al., *A new composite made of polyurethane and glass ceramic in a loaded implant model: a biomechanical and histological analysis.* Journal of Materials Science-Materials in Medicine, 1997. **8**(12): p. 753-756.
39. Harms, C., et al., *Osteogenic capacity of nanocrystalline bone cement in a weight-bearing defect at the ovine tibial metaphysis.* International Journal of Nanomedicine, 2012. **7**: p. 2883-2889.
40. Webster, T.J., et al., *Enhanced functions of osteoblasts on nanophase ceramics.* Biomaterials, 2000. **21**(17): p. 1803-1810.
41. Laurencin, C.T., S.G. Kumbar, and S.P. Nukavarapu, *Nanotechnology and orthopedics: a personal perspective.* Wiley Interdisciplinary Reviews-Nanomedicine and Nanobiotechnology, 2009. **1**(1): p. 6-10.

42. Sun, F., H. Zhou, and J. Lee, *Various preparation methods of highly porous hydroxyapatite/polymer nanoscale biocomposites for bone regeneration.* Acta Biomaterialia, 2011. **7**(11): p. 3813-3828.
43. Ngiam, M., et al., *The fabrication of nano-hydroxyapatite on PLGA and PLGA/collagen nanofibrous composite scaffolds and their effects in osteoblastic behavior for bone tissue engineering.* Bone, 2009. **45**(1): p. 4-16.
44. Sato, M. and T.J. Webster, *Nanobiotechnology: implications for the future of nanotechnology in orthopedic applications.* Expert Review of Medical Devices, 2004. **1**(1): p. 105-114.
45. Tran, P.A., et al., *Opportunities for nanotechnology-enabled bioactive bone implants.* Journal of Materials Chemistry, 2009. **19**(18): p. 2653-2659.
46. Meirelles, L., et al., *Nano hydroxyapatite structures influence early bone formation.* Journal of Biomedical Materials Research Part A, 2008. **87A**(2): p. 299-307.
47. Meirelles, L., et al., *Effect of Hydroxyapatite and Titania Nanostructures on Early In Vivo Bone Response.* Clinical Implant Dentistry and Related Research, 2008. **10**(4): p. 245-254.
48. MacMillan, A.K., et al., *Similar healthy osteoclast and osteoblast activity on nanocrystalline hydroxyapatite and nanoparticles of tri-calcium phosphate compared to natural bone.* International Journal of Nanomedicine, 2014. **9**: p. 5627-5637.
49. Guo, R., et al., *Substrate modulus regulates osteogenic differentiation of rat mesenchymal stem cells through integrin beta 1 and BMP receptor type IA.* Journal of Materials Chemistry B, 2016. **4**(20): p. 3584-3593.
50. Ohura, K., et al., *Resorption of, and bone formation from, new beta-tricalcium phosphate-monocalcium phosphate cements: An in vivo study.* Journal of Biomedical Materials Research, 1996. **30**(2): p. 193-200.
51. Munting, E., A.A. Mirtchi, and J. Lemaitre, *Bone Repair of Defects Filled with a Phosphocalcic Hydraulic Cement - an In-Vivo Study.* Journal of Materials Science-Materials in Medicine, 1993. **4**(3): p. 337-344.
52. Theiss, F., et al., *Biocompatibility and resorption of a brushite calcium phosphate cement.* Biomaterials, 2005. **26**(21): p. 4383-4394.
53. Frankenburg, E.P., et al., *Biomechanical and histological evaluation of a calcium phosphate cement.* Journal of Bone and Joint Surgery-American Volume, 1998. **80A**(8): p. 1112-1124.
54. Lovati, A.B., et al., *In Vivo Bone Formation Within Engineered Hydroxyapatite Scaffolds in a Sheep Model.* Calcified Tissue International, 2016. **99**(2): p. 209-223.
55. Lamerigts, N.M.P., et al., *Incorporation of morsellized bone graft under controlled loading conditions. A new animal model in the goat.* Biomaterials, 2000. **21**(7): p. 741-747.
56. Ignatius, A., et al., *Osseointegration of alumina with a bioactive coating under load-bearing and unloaded conditions.* Biomaterials, 2005. **26**(15): p. 2325-2332.
57. Gisep, A., et al., *Mechanical characterisation of a bone defect model filled with ceramic cements.* Journal of Materials Science-Materials in Medicine, 2004. **15**(10): p. 1065-1071.
58. Vaishya, R., M. Chauhan, and A. Vaish, *Bone cement.* J Clin Orthop Trauma, 2013. **4**(4): p. 157-63.

CHAPTER 6 - MEASUREMENT OF RELATIVE OSTEOCLAST-MEDIATED CERAMIC RESORPTION RATES USING PROFILOMETRY

Introduction

Patients suffering open fractures require bone grafting to promote healing. Autologous bone harvested from a donor site is often considered the clinical gold standard for bone grafting. However, autograft has limited availability and is associated with donor site morbidity.[1] Consequently, synthetic ceramics have been investigated as alternatives. The resorption characteristics of ceramic bone grafts regulate their rates of cellular infiltration, osteoblast differentiation, osseous deposition, and mechanical integrity.[2-4] Non-unions and inconsistent healing can occur if the rate of resorption of the bone graft does not match the rate of new bone formation.[5] While osteoclasts are well known to resorb bone grafts, the relative resorption rates of ceramic biomaterials have not been extensively investigated, and thus there is considerable interest in developing an inexpensive, reproducible *in vitro* assay to assess the rate of osteoclast-mediated resorption of synthetic substrates.

Calcium phosphate cements and bioactive glasses are two classes of biomaterials used widely in bone grafting.[6, 7] β-tricalcium phosphate (β-TCP) and hydroxyapatite (HA) are osteoconductive ceramics with mineral content similar to that of natural bone. Previous studies suggest that resorption of calcium phosphate is a predominately cellular process initiated by a number of cell types including macrophages, osteoclasts, and monocytes.[8, 9] In contrast, bioactive glasses (BG) are chemically active after surface contact with body fluids, releasing numerous ionic species that contribute to material dissolution, cellular response, and new bone growth.[6, 10] The dissolution rates of bioactive glasses are specific to the chemical composition of the particular silicate or phosphate based system of interest. In general, it has been shown that bioactive glasses remodel faster than ceramics *in vivo*.[11, 12] Remodeling of bioactive glasses proceeds through two processes: osteoclast-mediated resorption and bulk or surface chemical degradation.[3] Graft porosity, surface topography, biological signals, chemical structure, physiochemical properties (crystallinity, density), implantation site, and other factors all influence remodeling [8, 13-15], contributing to the challenges of measuring resorption rates of these materials.

A number of *in vitro* osteoclast assays have been previously reported. In an early study, 1α,25-dihydroxyvitamin D_3 (VD3) was used to stimulate mouse osteoblast precursor cells isolated from the calvaria to induce osteoclast differentiation in precursor cells harvested from the spleen [16] or long bones.[17] Additionally, some groups employed tumor necrosis factors (TNF) –α and –β [18] or interleukin 1 (IL-1) [19] to induce osteoclast resorption *in vitro*. Later work has revealed that the cytokine Receptor Activator of Nuclear Factor-κβ Ligand (RANKL) is responsible for osteoblast-driven osteoclastogenesis, while Macrophage-Colony Stimulating Factor (M-CSF) aids in osteoclast survival but not active resorption.[20] More recently, groups have used M-CSF and RANKL in *in vitro* osteoclast cultures with primary cells [21] or cell lines [22], but the high cost of these factors can be prohibitive. Commonly accepted markers for osteoclasts include multinucleated, tartrate resistant acid phosphatase (TRAP)-positive cells with actin rings.[23] Areas of osteoclast-mediated resorption have been measured by scanning electron microscopy (SEM) [21, 24], podosome belt formation [25], transmission electron microscopy (TEM) [26], light microscopy [27], three-dimensional (3D) laser color microscopy [24], and optical 3D profilometry.[28, 29] However, there are a limited number of time-course studies for quantifying the rate of osteoclast-mediated resorption of bone grafting biomaterials.

Previous assays using M-CSF and RANKL to differentiate osteoclastic precursor cells produce viable, active osteoclasts. However, these methods are limited by the cost of the growth factors and variability due to animal age and health when harvesting primary cells. It is desirable to develop a co-culture technique based on established cell lines that uses a small concentration of VD3 to reproducibly drive differentiation and to develop a standardized, quantifiable method to analyze relative osteoclast resorption rates. In this study, we co-cultured MC3T3 pre-osteoblast cells with a monocyte cell line (RAW 264.7 cells) on β-TCP, HA, or BG substrates. Dentin (D) chips were used as a bone control. Differentiation of

RAW 264.7 cells to osteoclasts was confirmed by DAPI, TRAP, and actin staining. Rates of resorption of the substrates relative to that of dentin were calculated from optical profilometry measurements of resorption area at three time points.

Experimental

Materials

The murine osteoblast precursor cell line, MC3T3, and the murine macrophage cell line, RAW 264.7, were purchased from ATCC (Manassas, VA). Hydroxyapatite (HA) and β-tricalcium phosphate (TCP) discs, sized to fit a 48 well plate, were purchased from 3D Biotek (Hillborough, NJ). 45S5 bioactive glass (BG) rods were obtained from Mo-Sci Corporation (Rolla, MO) and cut to ~0.5mm thickness using an IsoMet low speed saw (Buehler). Dentin (D) was acquired from the donation of a surrendered elephant tusk from the National Eagle and Wildlife Property Repository of the United States Department of the Interior, U.S. Fishes and Wildlife Service. Cells were cultured in osteogenic media (OM) comprised of α-MEM (minimum essential media) from GIBCO (Grand Island, NY) supplemented with 10% FBS (Hyclone, Logan, UT) and 1% Penicillin-Streptomycin (GIBCO) and the osteogenic factors 10 nM dexamethasone, 50 μg/mL ascorbic acid, and 0.1 mM β-glycerophosphate. 1α,25 dihydroxyvitamin D_3 (VD3) was purchased from Sigma (St. Louis, MO). Chemicals for intracellular and extracellular staining for tartrate resistant acid phosphatase (TRAP) were purchased from Sigma-Aldrich (St. Louis, MO).

Assay Development

MC3T3 cells were plated on a 24 well plate at 1×10^4 cells/well in 1 mL OM supplemented with 10 nM VD3. Cells were grown at 37 °C for 48 hours. Media was aspirated and RAW cells were plated at 1×10^4 cells/well in 1 mL OM supplemented with 10 nM VD3. Every 1-2 days 0.5 mL of OM was removed and replaced with new 0.5 mL OM supplemented with 10 nM VD3. Cells were imaged over the course of the study to analyze cell morphological changes and growth.

Sample sterilization and conditioning

BG discs were initially cleaned by sonication for 5 min in acetone:DI water (95:5 volume ratio). The BG, HA, TCP, and Dentin samples (n=5) were then sonicated for 7.5 min in DI water (3x). To sterilize, samples were immersed in 70% ethanol for 5 min (2x). After which time samples were washed in sterile DI water for 5 min (2x) before being transferred to tissue culture plastic plates. Samples were conditioned overnight in complete α-MEM prior to cell seeding.

Resorption Testing

Incubation media was removed from wells and materials were allowed to dry in a sterile hood for 30 min. MC3T3 cells were then plated on matrices of interest at 1 x 10^4 cells/100 µL OM in each well, following a protocol for osteoblast seeding from 3D Biotek. Well plates were incubated at 37 °C for 30 min to allow for cellular attachment. An additional 900 µL OM with 10 nM VD3 (for the whole 1 mL) was added to each well and cells were grown at 37 °C for 48 hours. Media was aspirated and RAW cells were plated at 1 x10^4 cells/100 µL OM. Well plates were incubated at 37 °C for 30 min to increase initial cellular attachment. An additional 900 µL OM with 10 nM VD3 was added to each well and cells were grown at 37 °C. After 48 hours matrix discs were moved to new well plates. Every 1-2 days 0.5 mL of OM was removed and replaced with new 0.5 mL OM supplemented with 10 nM VD3.

Tartrate resistant acid phosphatase (TRAP) activity

To quantify the amount of TRAP in cell culture supernatant, 0.5 ml cell culture medium at 17, 21 and 25 days was collected and stored at -80 °C. Secreted TRAP was quantified with naphthol AS-BI as the substrate. 50 µL of media was mixed with 150 µL reaction buffer (100 mM sodium acetate, 50 mM sodium tartrate, 2.5 mM naphthol ASBI-phosphate in 4% methoxyethanol) in a 96-well plate and incubated for 35 min at 37°C. The reaction was stopped by the addition of 0.6 M NaOH solution and fluorescence was read at 405 nm (excitation) and 520 nm (emission). Additionally, the fluorescence was corrected by measurements from control wells containing media without cells.

Actin staining

At desired time points, samples were removed from cell culture and fixed in 10% formalin for 10 min at room temperature. Samples were washed 2x with PBS and incubated with 0.1 % Triton-X in PBS for 5 min to permeabilize cells. Samples were incubated with rhodamine phalloidin (5 µL methanol solution in 200 µL PBS) protected from light for 45 min at 37 °C to stain actin. Samples were washed 2x with PBS, counterstained with DAPI (2 µg/mL) for 5 min protected from light, and washed 2x with PBS.

Profilometry

At desired time points, media was removed and sterile DI water was added to wells for 24 hours to loosen cells. Any remaining cells were removed by washing the surface with DI water. Samples were dried overnight on a benchtop. Resorption pits were analyzed using a Zeta Instruments Zeta-20 True Color 3D Optical Profiler (San Jose, CA). Images were collected using a Z-rage of 15-20 µm at 200 steps, resulting in a Z-step size of 0.075 – 0.1 µm. A 20x magnification was used to image at least 3 different areas per sample (field of view: 474 x 356 µm^2). Zeta feature detection software was used to quantify pits, specified as areas with a specified depth from a reference surface on non-resorbed areas. The minimum thresholds for pit detection were established as 3 µm for BG, 2 µm for D, and 1.5 µm for TCP and HA. The percent of the surface area that was resorbed was reported as well as total resorbed volume per image normalized to the analyzed field of view. Roughness of each sample (R_a) was analyzed from feature detection software.

Scanning Electron Microscopy

To further visualize resorption pits on substrates, scanning electron microscopy (SEM) images were taken of both initial, unresorbed samples and co-culture samples after 25 days. Samples were mounted onto a scanning electron microscopy (SEM) pin stub mount and sputter-coated for 40 s using a Cressington Q108 sputter coater, which deposits gold at a 30 mA current. A Zeiss Merlin SEM was used to acquire images.

Statistical analysis

Differences in resorption volumes, resorption area, and roughness among samples were analyzed by two-way ANOVA. Statistical significance was considered for $p < 0.05$.

Results

Assay Development

The MC3T3 and RAW 264.7 cell co-culture assay was developed using transparent tissue culture well plates to determine the time scale of osteoclast maturation. Bright-field images at day 5 (**Figure 6.1A**) show attachment of cells to the well plate. By day 10, large egg-shaped cells began to form (black arrows, **Figure 6.1B**), which suggests that cells were fusing to form monocytes. RAW 264.7 cells were stained for the osteoclastogenic factor TRAP on day 17 (**Figure 6.1C**). While a large number of TRAP+ nondifferentiated RAW cells (small circular cells, white arrows, **Figure 6.1C**) remained at day 17, some of the TRAP+ RAW cells had differentiated to form multi-nucleated osteoclasts (black arrows, **Figure 6.1C**). Differentiation of RAW cells to osteoclasts was further confirmed by DAPI staining at day 17 for multiple nuclei and the formation of actin rings (stained red and indicated by white arrows, **Figure 6.1D**). By day 17, multi-nucleated TRAP+ cells with an actin ring structure were observed, which indicates that RAW cells had differentiated to form osteoclasts.

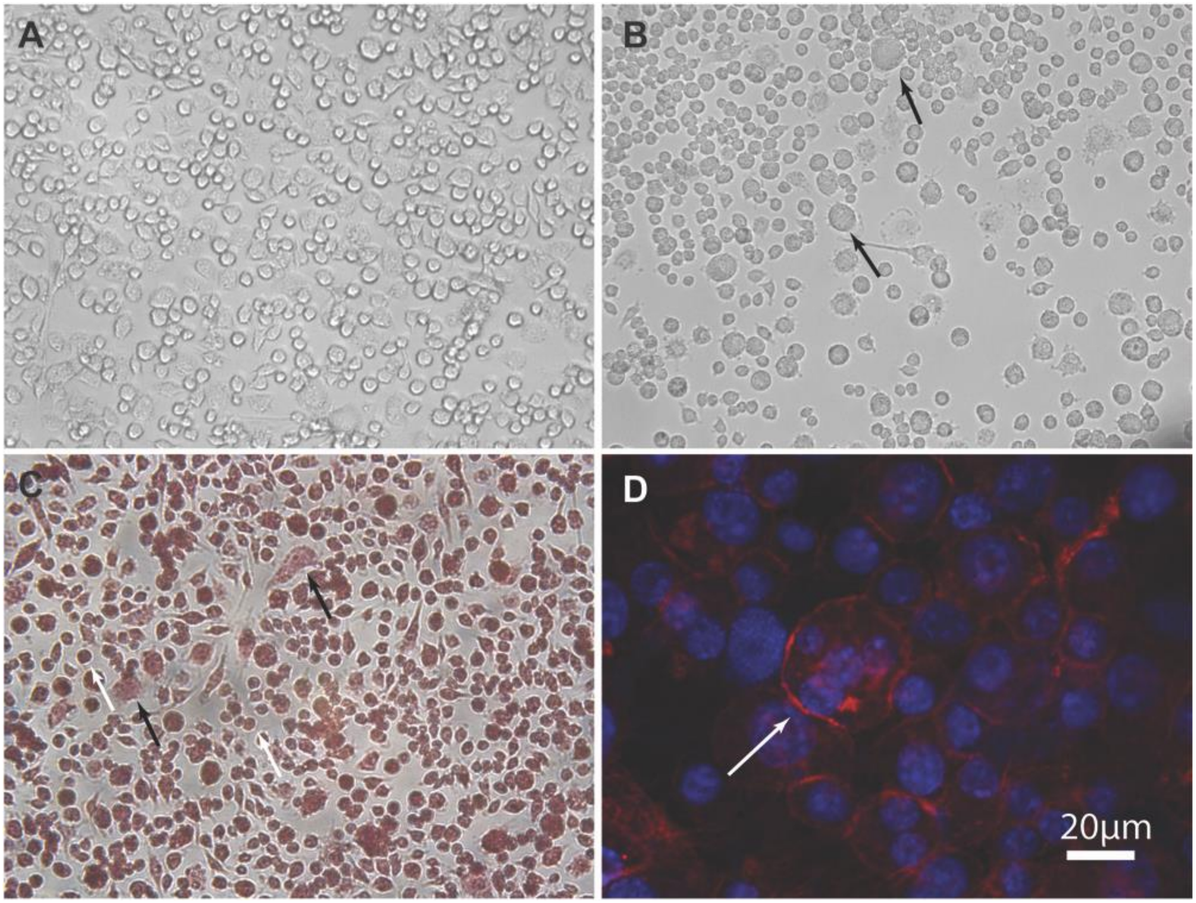

Figure 6.1 Bright field images of cells in co-culture on tissue culture plastic at (A) 5 days and (B) 10 days after the start of the assay. Cells at 17 days were (C) TRAP stained and (D) actin stained to show larger, TRAP+ cells and cells with a visible actin ring structure. Images A-C were taken at 20x.

Resorption Assay

Cells cultured on D, BG, TCP, and HA substrates were stained after 17 and 25 days for actin (red) with DAPI counter-staining for nuclei (blue, **Figure 6.2**). Multinucleated (≥ 3) cells with well-defined actin rings were observed on all materials, thereby indicating the presence of osteoclast-like cells (white arrows). Fewer osteoclasts were present on HA compared to D, BG, and TCP. On HA, a substantial number of cells with 2 nuclei were present, many of which appeared to be in the process of fusing with conjoining actin rings. Secretion of TRAP in cell culture medium was measured at day 17, 21, and 25 to quantify the extent of osteoclast differentiation on each substrate (**Figure 6.3**). Two-way ANOVA revealed a significant substrate effect ($p<0.0001$) between the groups, and one-way ANOVA at each time point suggested that TRAP secretion was significantly higher on dentin compared to BG group on day 17, 21 and 25. By day 25, TRAP secretion was highest on dentin group and lowest on BG group.

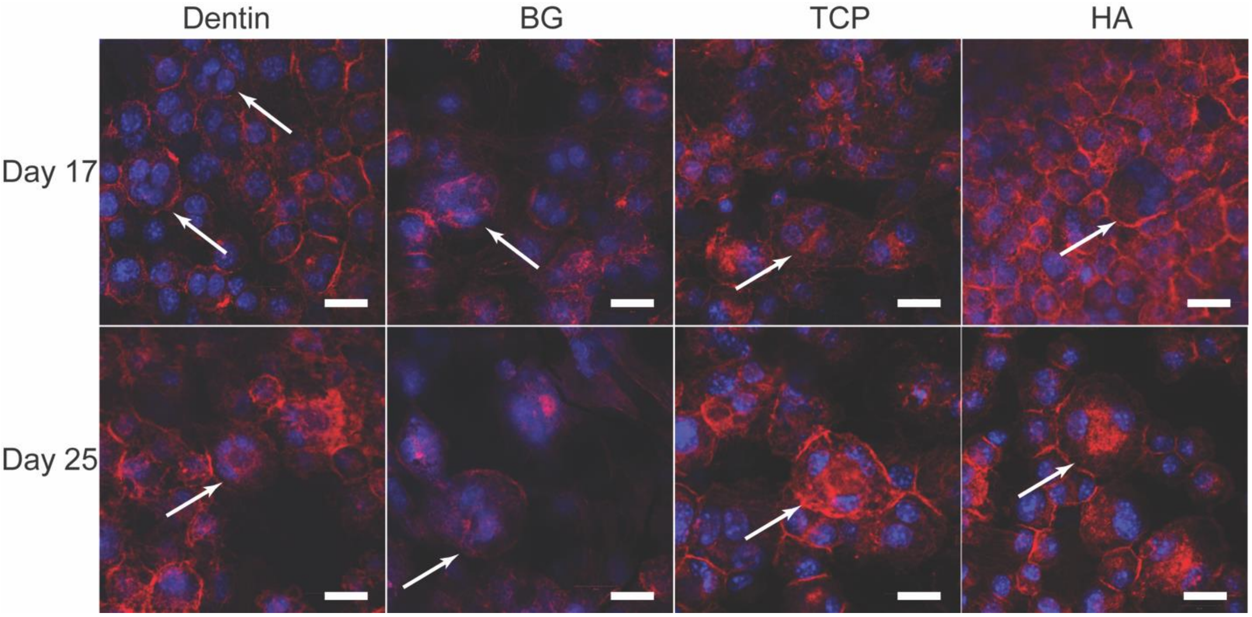

Figure 6.2 Confocal images of cells stained for actin (red) and DAPI (blue) on all substrate at day 17 and 25. White arrows point to osteoclasts. Scale bars represent 20μm.

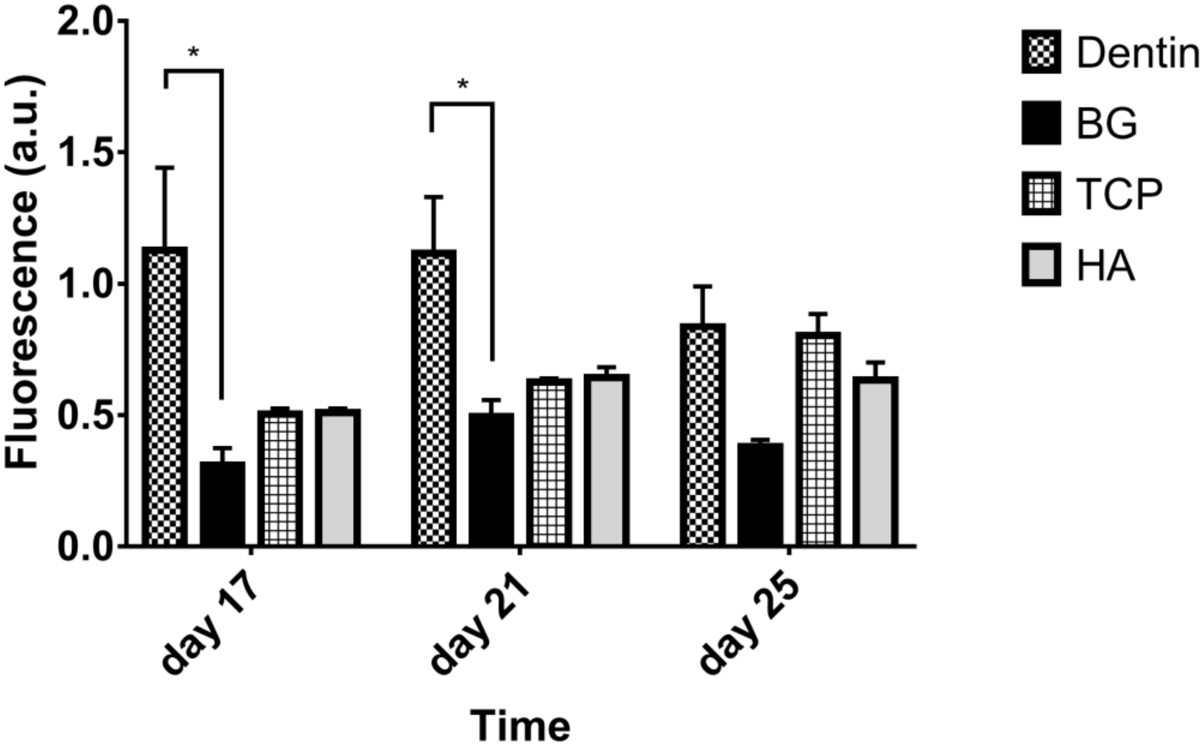

Figure 6.3 TRAP secretion in cell culture medium at day 17, 21 and 25. Error bars indicate SEM

Profilometry.

The substrates were analyzed for resorption pits using optical profilometry. Initial profilometry images of all samples showed no large pits (**Figure 6.4**, top row). Representative images of resorption pits (white arrows) formed after 25 days of co-culture samples are shown in **Figure 6.4** (bottom row). At 25 days, the surface of the BG discs was rougher than that of D, HA, or TCP, which is attributed to the dissolution of BG. While resorption pits were visible on all materials at all of the time points, the dentin substrates showed the largest pits. In contrast, resorption pits on HA were fewer in number and not homogenously distributed over the surface.

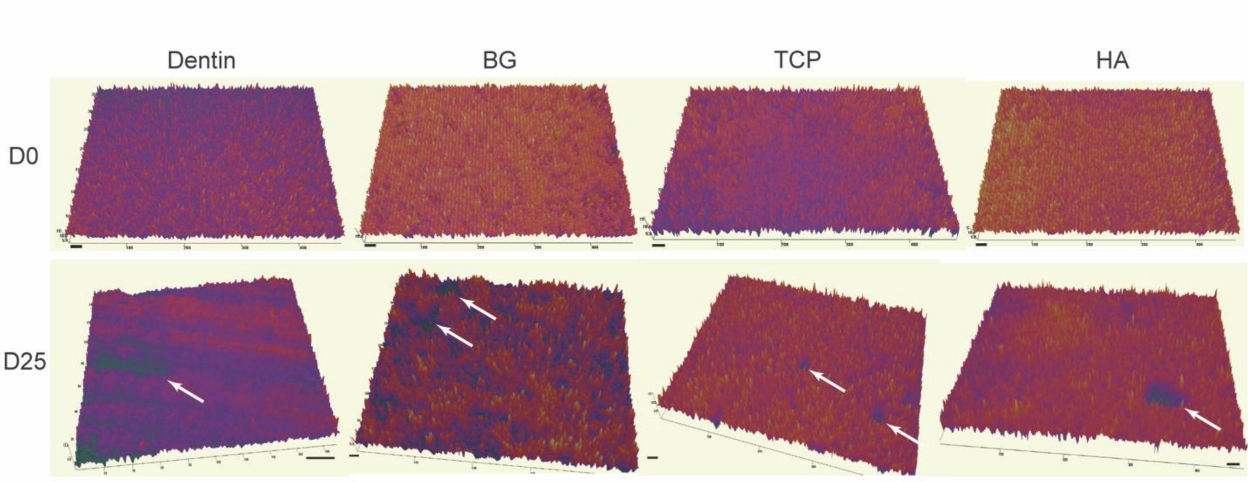

Figure 6.4 3D profilometry images of substrates 0 and 25 days in the osteoclast co-culture assay. White arrows point to resorption pits on the surface. The scale bars represent 20 µm.

The surface roughness (R_a) of the substrates was measured at each 17, 21, and 25 days for the cell-free control (**Figure 6.5A**) and cell-cultured (**Figure 6.5B**) groups. In the absence of cells, there were no significant differences between groups or time points, although the BG substrates trended toward higher surface roughness compared to the other groups (**Figure 6.5A**). In the presence of cells, the surface of the BG discs was significantly rougher than D, TCP, or HA at all time points (**Figure 6.5B**). While surface roughness of D, TCP, and HA substrates did not change over time, BG roughness showed an increasing trend with time (differences were not significant). Similar values of surface roughness were observed for D, TCP, and HA substrates in the absence or presence of cells, which is consistent with their low water solubility and relatively small (< 5) % area resorbed by osteoclasts. However, at day 25 the roughness of the BG substrates was significantly higher in the presence compared to the absence of cells, which suggests that by day 25 both dissolution and osteoclast-mediated resorption were actively modifying the

BG surface. The percent area resorbed on each surface and the resorption volume normalized to the surface area was calculated using Zeta feature detection software (**Figure 6.5C-D**). At day 17, BG showed the highest % area resorbed, which is attributed in part to the dissolution of the material. HA showed the lowest % area resorbed at both 21 and 25 days.

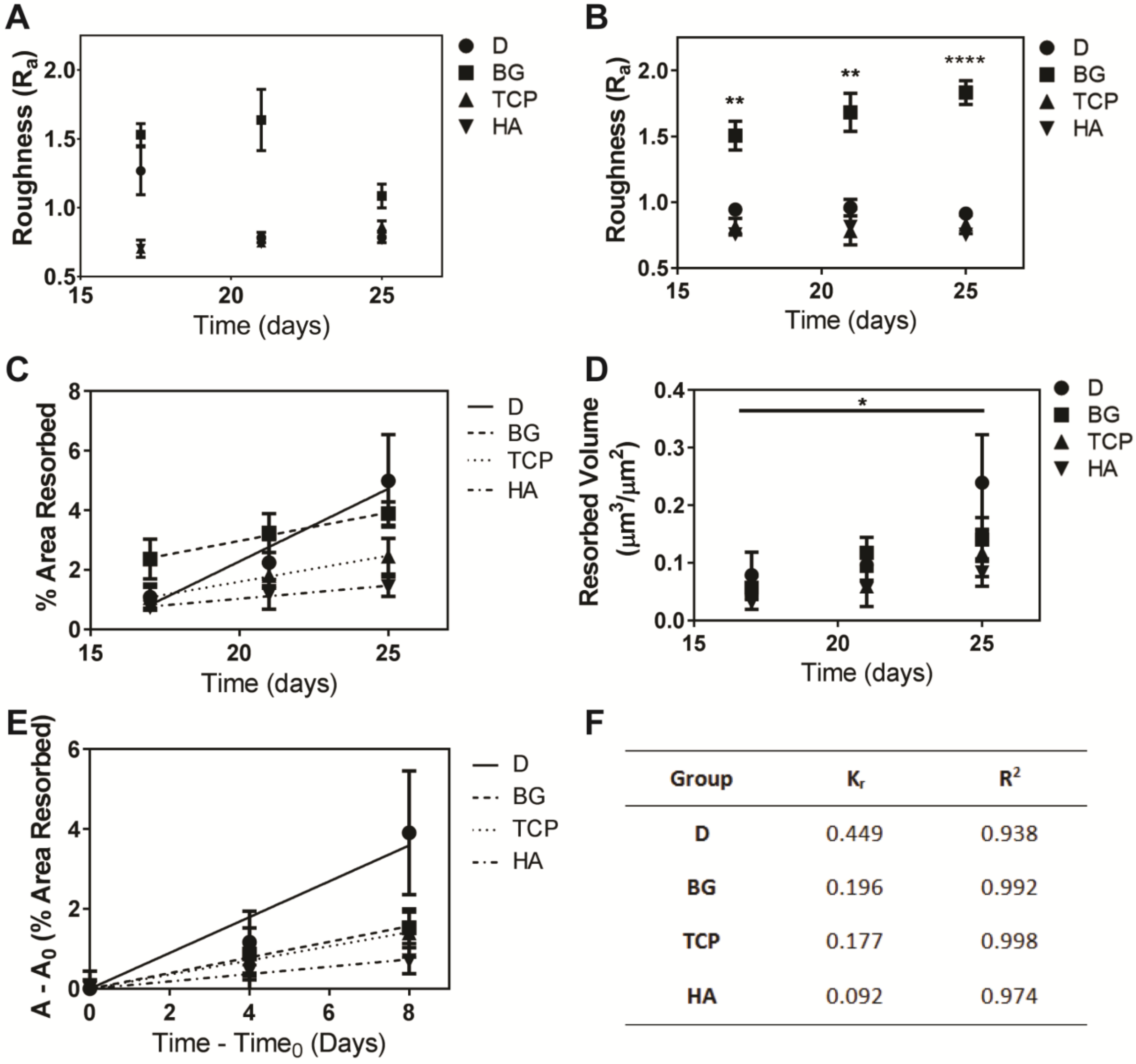

Group	K_r	R^2
D	0.449	0.938
BG	0.196	0.992
TCP	0.177	0.998
HA	0.092	0.974

Figure 6.5 Quantitative analysis of profilometry scans to determine (A) surface roughness of cell-free control samples, (B) surface roughness of substrates after 25 days of co-culture, (C) Area% resorbed at

each time point, (D) normalized resorption volume, (E) normalized Area% resorbed, and (F) fitting parameters for Eqn 5 fit to area percent resorption data. Error bars indicate SEM.

Consider osteoclast-mediated resorption of the substrates as a chemical reaction:

Osteoclast (OC) + Substrate (S) → Pits (P) (6.1)

According to mass-action kinetics, the rate of this reaction depends on the concentration of osteoclasts and substrate:

$$rate = \frac{dP}{dt} = k\left[OC\right]\left[S\right] \tag{6.2}$$

Where *t* represents time, *k* is the specific reaction rate, and [OC] and [S] represent the concentrations of osteoclasts and substrate, respectively. In our experiments, the substrate is in large excess, so the change in substrate concentration due to osteoclast-mediated resorption will be minimal. Consequently, [S] can be considered constant and the rate of pit formation approximated as

$$rate = \frac{dP}{dt} = k\left[S\right]\left[OC\right] \simeq k'\left[OC\right] \tag{6.3}$$

Equation (3) can be further simplified by considering that there were no significant differences in TRAP activity among the D, TCP, and HA groups over time (differences between D and BG were significant on days 17 and 21). Thus, as an approximation the concentration of osteoclasts (and also the rate of resorption) can be assumed constant over the course of the experiment:

$$rate = \frac{dP}{dt} \simeq k'\left[OC\right] \simeq k_r \tag{6.4}$$

Integration of **Equation (4)** gives

$$P - P_0 = k_r\left(t - t_0\right) \tag{6.5}$$

where P_0 is the initial pit area at t_0. **Equation (5)** indicates that resorption should be a linear function of time.

In order to compare the resorption rates of the substrates, we replotted the % area resorbed time-course data in the form of **Equation (5)** assuming that $t_0 = 17$ days (*i.e.*, the time when osteoclasts started to form, **Figure 6.5E**). The fitting parameters are shown in **Figure 6.5F**, where the slope (k_r) represents the resorption rate in units of % area resorbed per day (area-% day^{-1}). Dentin showed the highest rate of resorption at 0.449 area-% day^{-1}. BG and TCP showed similar values of 0.196 area-% day^{-1} and 0.177 area-% day^{-1}, respectively, while HA had the lowest resorption rate at 0.092 area-% day^{-1}. The goodness-of-fit to dentin ($R^2 = 0.94$) was lower than that determined for the other groups ($R^2 > 0.97$).

Scanning Electron Microscopy.

SEM images for TCP, HA, and D were taken after cleaning samples (day 0) and following 25 days in co-culture (**Figure 6.6**). Ridges were evident on clean dentin samples, while no recurrent topographical structures were present on the surface of HA or TCP discs. By 25 days, resorption pits were visible on the surfaces of all three substrates. While no significant differences in pit area (measured by profilometry) were observed between groups, the resorption pits on HA substrates appeared to be shallower and fewer in number compared to TCP and D. SEM images of BG substrates were taken after polishing, after 25 days in media without cells, and after 25 days in co-culture (Figure **6.6**). After polishing, the surface showed only minor blemishes. After 25 days in media without cells, the BG surface was significantly rougher with some cracks visible at higher magnification. After 25 days in co-culture, significant cracking was visible with an increase in surface roughness.

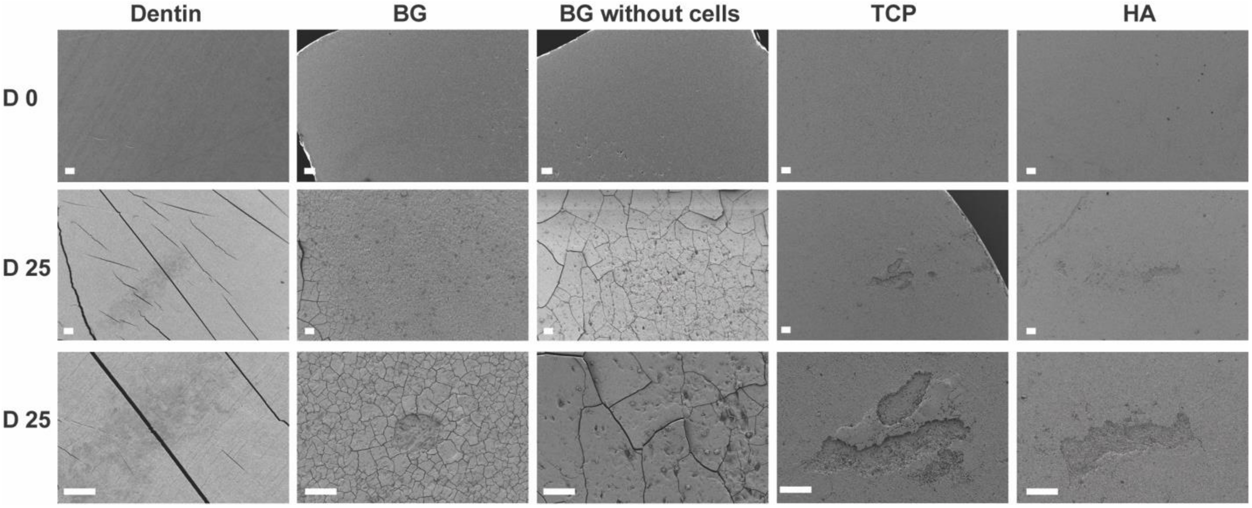

Figure 6.6 SEM images of cleaned substrates (D 0) and substrates after 25 days of co-culture. Scale bars represent 100 µm.

Discussion

In order to design an effective bone graft, it is important to understand its resorption kinetics. A recent study has suggested that defects heal more reproducibly when the rate of graft resorption is comparable to that of new bone deposition.[5] However, there are a limited number of studies reporting the osteoclast-mediated resorption rates of ceramics and bioactive glasses relative to bone, and there is no simple, low-cost, and high-throughput assay for measuring the rate of resorption. In the present study, we report an osteoblast-osteoclast co-culture assay to calculate relative resorption rates on a variety of synthetic materials using optical profilometry to measure the percentage of the surface that has been resorbed by the osteoclasts. The resorption rates of BG, TCP, and HA were 44%, 40%, and 20% of the dentin resorption rate, respectively.

Osteoclastogenesis assays vary widely based on the initial cell source and differentiation methods. While M-CSF and RANKL can be used to drive differentiation of primary monocytes to osteoclasts within 5 – 7 days [25, 30], the cost of these growth factors can be prohibitive. Alternatively, addition of 1α,25-dihydroxyvitamin D_3 (VD3) to osteoblast-osteoclast co-cultures has been shown to promote secretion of RANKL by osteoblasts, resulting in increased osteoclastogenesis.[17, 31] In the present study, we used VD3 to promote osteoclast differentiation in a co-culture of MC3T3 and RAW264.7 cells. Consistent with previous studies, we observed large, egg-like osteoclast precursor cells within 2 weeks that were TRAP+ by 17 days. Fluorescence labeling of the actin ring and the nuclear marker DAPI as well as SEM imaging of resorption pits indicated that multi-nucleated (3 – 5 nuclei) osteoclasts had formed on all substrates by day 17. These findings are consistent with previous studies.[32] Human leukoma monocytes cultured on HA and TCP discs showed more multi-nucleated TRAP+ cells on HA, with F-actin rings and resorption pits (5 – 65 µm in diameter) present on both materials at 21 days.[33]

Once osteoclasts attach to the surface, a resorption lacuna is formed. Secretion of hydrogen ions into this privileged microenvironment reduces the local pH to approximately 4.5 [34], resulting in degradation of the ceramic. The ability of osteoclasts to pit the surface of calcium phosphates is dependent on their chemical composition and crystallinity.[35] In the present study, resorption pits by optical profilometry and SEM on all substrates were tested. The resorption rates were measured by profilometry, which enabled quantitative comparisons between bone (modeled by dentin) and synthetic ceramics. Dentin (D) showed the fastest rate of resorption. The resorption rates of BG, TCP, and HA were 44%, 40% and 20% of the rate measured for D, respectively. These findings exhibit trends similar to previous studies. One study found that osteoclasts will resorb TCP but not HA *in vitro*.[36] Allograft particles have been reported to be resorbed at a much higher rate (up to 70% resorption by osteoclasts *in vitro* after 14 days).[37] Under *in vivo* conditions, TCP ceramics remodel at a rate comparable to osseous deposition, while HA ceramics persist for a significantly longer time.[3] TCP has been reported to undergo resorption *in vivo* at a rate of 1.4 $\mu m^3 \mu m^{-2} day^{-1}$ in femoral diaphyseal defects in rabbits, while BG degraded about 30%-50% after 12 weeks in femoral metaphyseal defects in rabbits.[38] Polymer/allograft bone composites were fully degraded by one year, while residual ceramic was visible in defects treated with MasterGraft (a blend of 85% TCP and 15% HA) at 2 years in a sheep femoral plug model.[39]

Unlike other bone graft substitutes, the degradation products of calcium phosphates are used for *de novo* bone formation.[40] Phosphate ions have been shown to affect osteoblast apoptosis, osteopontin production, and mineralization.[26] Calcium ions aid in the regulation of osteoblast proliferation and osteoclast differentiation. However, the release of large numbers of calcium ions may interfere with resorption, which is of importance for substrates with higher rates of dissolution.[36] Osteoclasts are able to sense Ca^{2+} levels, and high concentrations of Ca^{2+} ions lead to decreased TRAP expression and morphological changes in osteoclasts.[41] While increased Ca^{2+} concentration may inactivate osteoclasts, the increased presence of Ca, P, and Si ions may enhance osteoblast differentiation and activity.[42] The effect of these degradation products from ceramics on cellular signaling pathways in osteoblast/osteoclast co-culture is an important area for potential future studies.

While the rate of resorption of BG was similar to that of TCP, BG discs showed the highest percent % area resorbed, volume resorbed, and surface roughness (**Figures 6.5B-D**). These findings suggest that dissolution contributed to changes in the surface of the BG substrate. Thus, it was difficult to separate the effects of surface dissolution from those of osteoclast-mediated resorption, as both of these mechanisms likely contributed to the degradation of the material. These findings are consistent with a previous study that used inductively coupled plasma–optical emission spectrometry to show that osteoclast-mediated resorption of strontium-substituted bioactive glass processed at a similar time scale as ion dissolution.[22] Another limitation of this study is the assumption of a constant number of osteoclasts on each substrate, resulting in a zero-order rate law (**Equation (4)).** Furthermore, due to the difficulty of counting the number of osteoclasts on the surface, the % area resorbed was normalized to the concentration of secreted TRAP secretion. Thus, the absolute resorption rates (in terms of osteoclast number) of the substrates could not be determined.

Conclusion

The aim of this study was to develop an inexpensive, standardized osteoblast-osteoclast co-culture assay to measure relative resorption rates of ceramic substrates. Resorption by osteoclasts grown from a co-culture of MC3T3 and RAW 264.7 cells was evaluated on D, TCP, HA, and BG substrates. The co-culture assay produced multinucleated cells with a visible actin ring within 3 weeks on all substrates. Resorption was measured by optical profilometry with relative resorption rates determined on ceramics and bioactive glass. The relative rates of resorption of BG, TCP, and HA were 44%, 40%, and 20% of that measured for dentin (a control for bone). This study presents a new method to differentiate osteoclasts directly on substrates of interest and quantify relative resorption rates that will potentially aid in the development of new biomaterials that experience balanced remodeling when implanted *in vivo*.

References

1. Zimmermann, G. and A. Moghaddam, *Allograft bone matrix versus synthetic bone graft substitutes.* Injury, 2011. **42, Supplement 2**: p. S16-S21.
2. Yaszemski, M.J., et al., *Evolution of bone transplantation: molecular, cellular and tissue strategies to engineer human bone.* Biomaterials, 1996. **17**(2): p. 175-185.
3. Lichte, P., et al., *Scaffolds for bone healing: Concepts, materials and evidence.* Injury, 2011. **42**(6): p. 569-573.
4. Bose, S., M. Roy, and A. Bandyopadhyay, *Recent advances in bone tissue engineering scaffolds.* Trends Biotechnol, 2012. **30**(10): p. 546-54.
5. Dumas, J.E., et al., *Balancing the rates of new bone formation and polymer degradation enhances healing of weight-bearing allograft/polyurethane composites in rabbit femoral defects.* Tissue Eng Part A, 2014. **20**(1-2): p. 115-29.
6. Jones, J.R., *Review of bioactive glass: from Hench to hybrids.* Acta Biomater, 2013. **9**(1): p. 4457-86.
7. Hing, K.A., L.F. Wilson, and T. Buckland, *Comparative performance of three ceramic bone graft substitutes.* The Spine Journal, 2007. **7**(4): p. 475-490.
8. Lu, J., et al., *The biodegradation mechanism of calcium phosphate biomaterials in bone.* Journal of biomedical materials research, 2002. **63**(4): p. 408-412.
9. Detsch, R., et al., *The resorption of nanocrystalline calcium phosphates by osteoclast-like cells.* Acta Biomaterialia, 2010. **6**(8): p. 3223-3233.
10. Hoppe, A., N.S. Güldal, and A.R. Boccaccini, *A review of the biological response to ionic dissolution products from bioactive glasses and glass-ceramics.* Biomaterials, 2011. **32**(11): p. 2757-2774.
11. Oonishi, H., et al., *Quantitative comparison of bone growth behavior in granules of Bioglass®, A-W glass-ceramic, and hydroxyapatite.* Journal of Biomedical Materials Research, 2000. **51**(1): p. 37-46.
12. Talley, A.D., et al., *Effects of rhBMP-2 Dose and Ceramic Composition on New Bone Formation and Space Maintenance in a Canine Mandibular Ridge Saddle Defect Model.* Tissue Engineering, 2016(ja).
13. Fröhlich, M., et al., *Tissue Engineered Bone Grafts: Biological Requirements, Tissue Culture and Clinical Relevance.* Current stem cell research & therapy, 2008. **3**(4): p. 254-264.
14. Larsson, S. and G. Hannink, *Injectable bone-graft substitutes: Current products, their characteristics and indications, and new developments.* Injury, 2011. **42, Supplement 2**: p. S30-S34.
15. Barrère, F., C.A. van Blitterswijk, and K. de Groot, *Bone regeneration: molecular and cellular interactions with calcium phosphate ceramics.* International Journal of Nanomedicine, 2006. **1**(3): p. 317-332.
16. Takahashi, N., et al., *Osteoblastic Cells are Involved In Osteoclast Formation.* Endocrinology, 1988. **123**(5): p. 2600-2602.
17. McSheehy, P.M. and T.J. Chambers, *1,25-Dihydroxyvitamin D3 stimulates rat osteoblastic cells to release a soluble factor that increases osteoclastic bone resorption.* Journal of Clinical Investigation, 1987. **80**(2): p. 425-429.
18. Thomson, B.M., G.R. Mundy, and T.J. Chambers, *Tumor necrosis factors alpha and beta induce osteoblastic cells to stimulate osteoclastic bone resorption.* The Journal of Immunology, 1987. **138**(3): p. 775-9.
19. Thomson, B.M., J. Saklatvala, and T.J. Chambers, *Osteoblasts mediate interleukin 1 stimulation of bone resorption by rat osteoclasts.* The Journal of Experimental Medicine, 1986. **164**(1): p. 104-112.

20. Udagawa, N., et al., *Osteoblasts/stromal cells stimulate osteoclast activation through expression of osteoclast differentiation factor/RANKL but not macrophage colony-stimulating factor.* Bone, 1999. **25**(5): p. 517-523.
21. Kirstein, B., T.J. Chambers, and K. Fuller, *Secretion of tartrate-resistant acid phosphatase by osteoclasts correlates with resorptive behavior.* J Cell Biochem, 2006. **98**(5): p. 1085-94.
22. Gentleman, E., et al., *The effects of strontium-substituted bioactive glasses on osteoblasts and osteoclasts in vitro.* Biomaterials, 2010. **31**(14): p. 3949-3956.
23. Botelho, C., et al., *Differentiation of mononuclear precursors into osteoclasts on the surface of Si-substituted hydroxyapatite.* Journal of biomedical Materials research part A, 2006. **78**(4): p. 709-720.
24. Friederichs, R.J., et al., *In vitro osteoclast formation and resorption of silicon-substituted hydroxyapatite ceramics.* J Biomed Mater Res A, 2015.
25. Fuller, K., et al., *Bone is not essential for osteoclast activation.* PLoS One, 2010. **5**(9): p. e12837.
26. Jensen, S.S., et al., *Osteoclast-like cells on deproteinized bovine bone mineral and biphasic calcium phosphate: light and transmission electron microscopical observations.* Clinical Oral Implants Research, 2015. **26**(8): p. 859-864.
27. Wilson, S.R., et al., *Cathepsin K activity-dependent regulation of osteoclast actin ring formation and bone resorption.* J Biol Chem, 2009. **284**(4): p. 2584-92.
28. Pascaretti-Grizon, F., et al., *Measurement by vertical scanning profilometry of resorption volume and lacunae depth caused by osteoclasts on dentine slices.* Journal of Microscopy, 2011. **241**(2): p. 147-152.
29. Pavlos, N.J., et al., *Tctex-1, a novel interaction partner of Rab3D, is required for osteoclastic bone resorption.* Molecular and cellular biology, 2011. **31**(7): p. 1551-1564.
30. Jensen, E.D., et al., *Bone morphogenic protein 2 directly enhances differentiation of murine osteoclast precursors.* J Cell Biochem, 2010. **109**(4): p. 672-82.
31. Kogawa, M., et al., *The metabolism of 25-(OH)vitamin D3 by osteoclasts and their precursors regulates the differentiation of osteoclasts.* The Journal of Steroid Biochemistry and Molecular Biology, 2010. **121**(1–2): p. 277-280.
32. Pham, L., et al., *HDAC3 and HDAC7 have opposite effects on osteoclast differentiation.* Journal of Biological Chemistry, 2011. **286**(14): p. 12056-12065.
33. Detsch, R., H. Mayr, and G. Ziegler, *Formation of osteoclast-like cells on HA and TCP ceramics.* Acta Biomaterialia, 2008. **4**(1): p. 139-148.
34. Bohner, M., L. Galea, and N. Doebelin, *Calcium phosphate bone graft substitutes: Failures and hopes.* Journal of the European Ceramic Society, 2012. **32**(11): p. 2663-2671.
35. Winkler, T., et al., *Volumetric analysis of osteoclastic bioresorption of calcium phosphate ceramics with different solubilities.* Acta Biomaterialia, 2010. **6**(10): p. 4127-4135.
36. Yamada, S., et al., *Osteoclastic resorption of calcium phosphate ceramics with different hydroxyapatite/β-tricalcium phosphate ratios.* Biomaterials, 1997. **18**(15): p. 1037-1041.
37. Muzylak, M., et al., *The in vitro effect of pH on osteoclasts and bone resorption in the cat: implications for the pathogenesis of FORL.* J Cell Physiol, 2007. **213**(1): p. 144-50.
38. Ito, A., et al., *Interlaboratory studies on in vitro test methods for estimating in vivo resorption of calcium phosphate ceramics.* Acta Biomater, 2015. **25**: p. 347-55.
39. Talley, A.D., et al., *Remodeling of Injectable, Low-Viscosity Polymer/Ceramic Bone Grafts in a Sheep Femoral Defect Model.* Journal of Biomedical Materials Research: Part B - Applied Biomaterials **Accepted**.
40. Bohner, M., *Resorbable biomaterials as bone graft substitutes.* Materials Today, 2010. **13**(1–2): p. 24-30.
41. Zaidi, M., et al., *Emerging Insights into the Role of Calcium Ions in Osteoclast Regulation.* Journal of Bone and Mineral Research, 1999. **14**(5): p. 669-674.

42. Chen, Q.Z., et al., *Bioglass®-derived glass–ceramic scaffolds: Study of cell proliferation and scaffold degradation in vitro.* Journal of Biomedical Materials Research Part A, 2008. **84A**(4): p. 1049-1060.

CHAPTER 7 - CONCLUSIONS AND SUGGESTIONS FOR FUTURE WORK

Summary of the dissertation

The research presented in this dissertation describes the design and development of resorbable polyurethane (PUR)-based composites that possess both biological functionality and load-bearing capacity. Findings and conclusions presented in previous chapters have provided insight into the foundation of polyurethane-based formulations for clinical treatments of bone defects at weight-bearing sites.

To our knowledge, Chapter III reports the first injectable and settable bone cements that meet the targeted properties for treating weight-bearing bone defects. A solvent-free process for grafting lysine triisocyanate (LTI) to nanocrystalline hydroxyapatite (nHA) particles was developed. The grafting reaction yielded a flowable prepolymer that was further used to fabricate the cement by two-component mixing with a polyester triol. The resulting nHA-PEUR nanocomposites were injectable and settable, exhibited bone-like strength, stimulated osteoblast mineralization, and resorbed in response to osteoclast and oxidative microenvironment associated with bone remodeling. Furthermore, grafting LTI to nHA enhanced the dispersion of nHA particles in the nanocomposites, resulting in enhanced mechanical properties and osteogenic differentiation. This new technology platform represents a potentially significant advance toward the design of biomaterials that actively heal while maintaining weight-bearing functionality.

While the results presented in Chapter III highlight the potential of nHA-PEUR nanocomposites for repair and restoration of bone defects at weight-bearing sites, the stability of the prepolymer and the mechanical properties of the nanocomposites are highly dependent on the conversion of the nHA-LTI grafting reaction. Reaction conditions need to be optimized to minimize side reactions and achieve high conversion of hydroxyl groups on nHA surface.

Chapter IV demonstrates a detailed study on the nHA-LTI grafting reaction. The reaction was conducted under different conditions, and the extent of the reaction was measured by %NCO titration of the reaction mixture and by surface Nitrogen/Phosphorous (N/P) ratio of nHA particles. In the presence of FeAA catalyst, the reaction mixture gelled after 120 hours. While %NCO of the reaction mixture continued to decrease over time, the N/P ratio appeared to reach steady state, and did not exceed 3, which suggested that the crosslinking was occurring in the bulk phase and not on the nHA surface. FTIR spectrum revealed evidence of urea bonds, which suggested that the grafting reaction competed with the urea reaction between LTI and water, and that the grafting reaction must be performed under dry conditions. When nHA particles were aggressively dried prior to reaction, the %NCO of the reaction mixture was stable over 40 days. These findings identify potential problems and provide solutions related to fabrication of the nHA-PEUR nanocomposites. This information is useful for technology transfer and commercialization.

Chapter V presents an *in vivo* study of the nHA-PEUR nanocomposites demonstrated in Chapter III. Instead of being injected directly into the bone defects, the nHA-PEUR composites were incorporated with micron-sized ceramic MASTERGRAFT® (MG) and bioactive glass (BG) granules to form settable bone grafts that allowed surgeons to shape them by hand. The grafts were tested in weight-bearing tibial plateau defects and non-weight-bearing femoral plug defects in sheep. BGMG/nHA-PEUR grafts underwent controlled remodeling at non-weight-bearing femoral plug defects but resorbed rapidly and were infiltrated by fibrous tissue at weight-bearing tibial plateau sites, while MG/nHA-PEUR composites maintained stability at both non-weight-bearing and weight-bearing sites. Mechanical loading at the anatomic site dramatically affected graft remodeling. MG/nHA-PEUR composites remodeled significantly faster at weight-bearing site compared to non-weight-bearing site, and the rate of remodeling at the bottom interface of tibial plateau defect was faster than that of the top interface. MG/nHA-PEUR grafts provided favorable handling properties and adequate mechanical stability through the early remodeling process, integrated with host bone at 16 weeks without formation of resorption gap and fibrous tissue, stimulated new bone formation and were resorbed by osteoclasts. These findings highlight the potential of MG/nHA-PEUR composites for treatment of bone defects at weight-bearing sites.

In addition to *in vivo* tests on the remodeling of the bone grafts, an *in vitro* assay was developed to quantify relative resorption rates of synthetic ceramic substrates by co-culture technique. Osteoclasts formed on all substrates within 3 weeks from co-culture of MC3T3 and RAW 264.7 cells, as evidenced by actin/DAPI staining. Osteoclast resorption rates on dentin (D), β-tricalcium phosphate (β-TCP), hydroxyapatite (HA) and bioactive glass (BG) were measured by optical profilometry over three time points. The relative rates of resorption of BG, β-TCP, and HA were 44%, 40%, and 20% of that measured for D. The method presented in this chapter is a useful screening tool to quantify and compare resorption rates of synthetic substrates and will aid in the design of new biomaterials that undergo balanced remodeling when implanted *in vivo*.

Suggestions for future work

The results presented in this work have highlighted the potential of nHA-PEUR cements and bone grafts containing nHA-PEUR for treatment of bone defects at weight-bearing sites. In order to apply the developed material into clinics, optimization and modification of the formulation is still needed, and questions regarding the remodeling of the implants *in vivo* need to be thoroughly studied. The following are suggestions for future work that address new research avenues and further translate the technology from bench to clinics.

3D nHA-PEUR scaffolds that recapitulate the composition and morphology of natural bone

The nHA-PEUR nanocomposites demonstrated in Chapter III could be utilized to fabricate porous scaffolds with desired morphology for bone tissue engineering. Studies have shown that the geometry of the porous scaffolds used for bone tissue engineering has significant influence on cellular response and bone regeneration rate.[1] The Guelcher Lab has previously developed a process to fabricate PUR scaffolds with patterned, rod-like pores, whose diameter could be precisely controlled using 3D printed templates, and has shown that osteoblast differentiation and mineralization increased with decreasing pore size.[2] Recently, 3D templates that recapitulate the irregular pores of trabecular bone have been developed using microCT imaging together with 3D inkjet printing technology.[3] However, due to the lack of mineral content in the scaffold formulation in the previous study, osteoblast differentiation and mineralization was not robust.

The development of nHA-PEUR nanocomposites has solved the formulation problem. The uniform distribution of nHA particles in nHA-PEUR nanocomposites significantly enhanced protein adsorption, osteoblast differentiation and mineralization compared to PUR alone. The material also resorbed in response to osteoclasts. The combination of 3D printed templates and nHA-PEUR nanocomposites could be used to develop *in vitro* 3D model that recapitulate both composition and topological properties of natural bone, which will be a powerful tool to study cell-matrix interaction in the bone microenvironment as well as an effective approach to study bone disease and screen drugs.

In vitro 3D model for studying effects of mechanical force on remodeling of bone grafts

The results presented in Chapter V revealed that nHA-PEUR/MG bone grafts remodeled faster at weight-bearing tibial plateau defects compared to non-weight-bearing femoral plug defects. However, the mechanism is unclear. Studies have shown that the repair of skeleton is dependent on mechanical information. Cell population within the bone, including osteoblasts, osteoclasts, and osteocytes are responsive to mechanical signals.[4] In order to develop bone grafts that maintain mechanical stability through the remodeling process at weight-bearing sites, it is necessary to illustrate the mechanism of how mechanical force influence bone cell population.

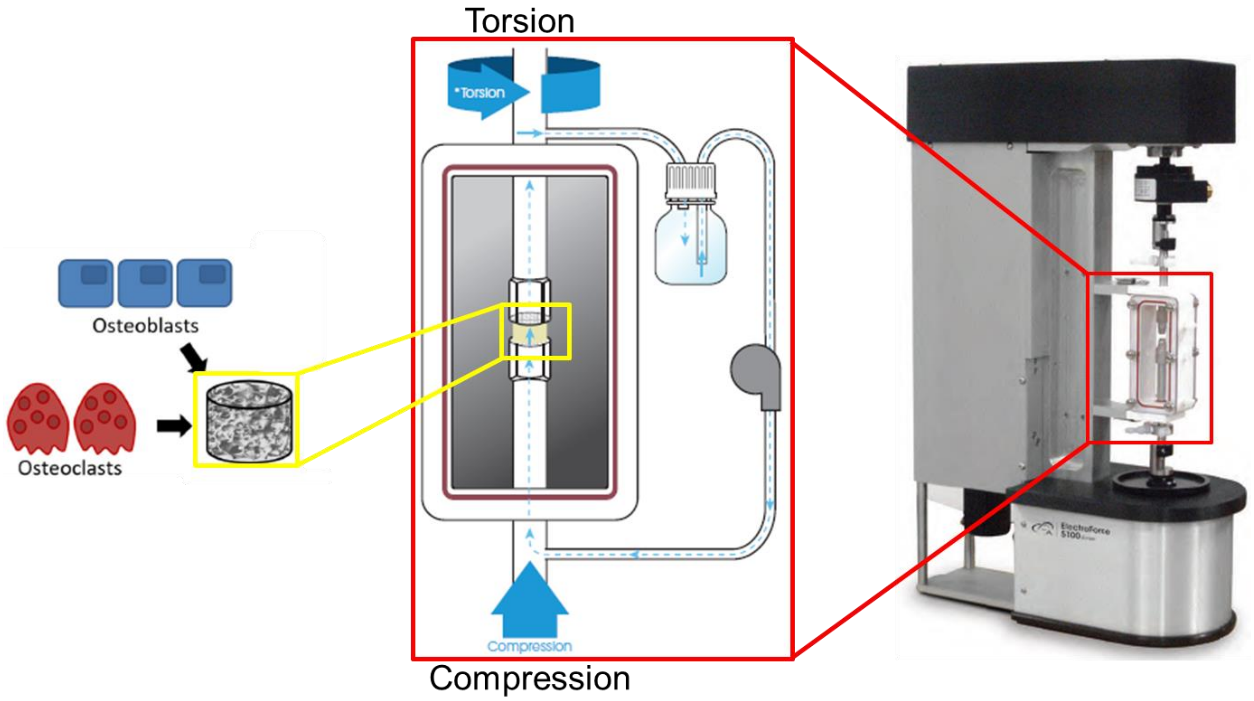

Figure 7.1 *In vitro* bioreactor model for studying effects of mechanical loading on cellular behaviors of osteoblasts and osteoclasts. Adapted from Current Osteoporosis Reports, Engineering 3D Models of Tumors and Bone to Understand Tumor-Induced Bone Disease and Improve Treatments, 15, 2017, Page 252, Kristin A. Kwakwa, et al, with permission of Springer.[5] and TA Instruments, Electroforce® Biodynamic® Test Instruments Brochure, 2016, with permission of TA Instruments [6]

The use of bioreactor reduces the use of complex and expensive animal models, while still gaining clinical relevant results, thus is a useful tool for mechanism study. **Figure 7.1** demonstrates the 3D *in vitro* bioreactor model for studying effects of mechanical loadings on cellular activity. The perfusion bioreactor circulates cell culture medium through the cell culture construct to favor cell viability and prolong culture time compared to conventional static cell culture. The flow rate can be adjusted to match the physiological flow rate and shear stress inserted on cells *in vivo*. At the meantime, mechanical force, including torsion and compression, can be applied to the construct. 3D nHA-PEUR scaffolds described in the previous text can be used as cell culture constructs that mimic bone-like matrix. Since the nHA-PEUR nanocomposites exhibit bone-like mechanical properties, it is expected that the deformation of 3D nHA-PEUR scaffolds will be similar to that of natural bone in response to mechanical loading, and further stimulate cells cultured in the scaffolds. Osteoblasts and osteoclasts could be co-cultured in this model. Gene expression of osteogenic and osteoclastogenic differentiation markers as well as matrix deposition by osteoblasts and osteoclast-mediated resorption could be measured at different loading conditions. The results on how mechanical loading affects osteoblast and osteoclast differentiation and activity would aid in the design of bone grafts that undergo balanced remodeling *in vivo* at weight-bearing sites.

Balancing resorption of nHA-PEUR/MG bone grafts with new bone growth

Chapter V showed the promising results that nHA-PEUR/MG bone grafts maintained mechanical stability while remodeling at weight-bearing tibial plateau defects for up to 16 weeks. Although the grafts resorbed and integrated with host bone at 16 weeks, the resorption rate was relatively slow, resulting in limited cellular infiltration and new bone formation at the interior of the grafts. Several strategies could be explored to optimize the resorption rate of the grafts.

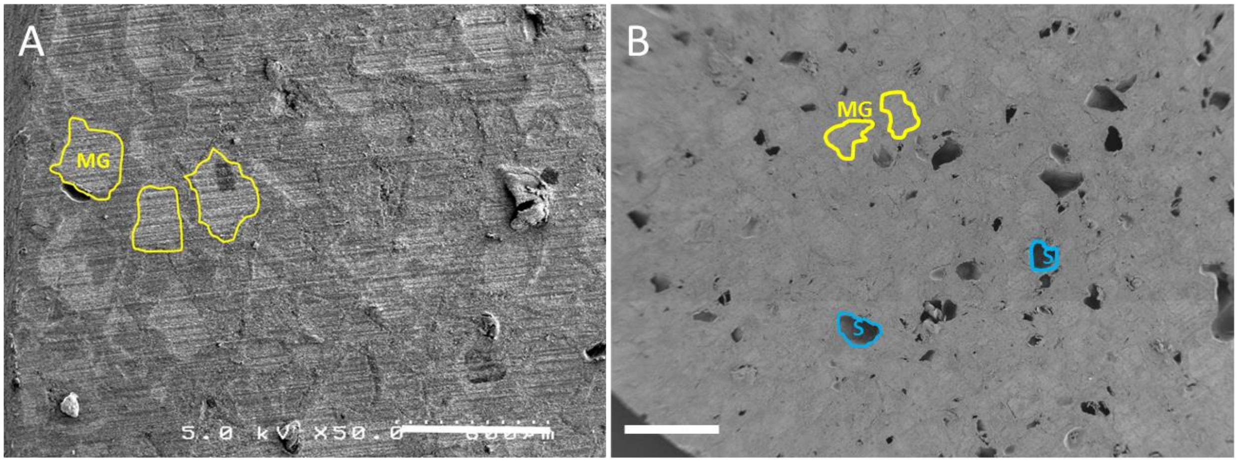

Figure 7.2 SEM images of cross section area of (A) nHA-PEUR/MG grafts and (B) nHA-PEUR/MG/sucrose (10 wt%) grafts. Scale bar=600 µm. MG: mastergraft, S: sucrose.

One strategy is to fabricate porous grafts that allow cells to infiltrate into the graft more rapidly. Since there is a tradeoff between porosity and mechanical strength, porosity of the graft needs to be precisely controlled. Sucrose leaching is an effective way to incorporate pores in a controlled manner. Sucrose particles could be blended into the graft together with MG particles at different ratios. The total volume percent of solid particles in the graft needs to be constant in order to maintain the handling properties. When implanted in the defect, sucrose will be leached out and leave pores in the graft. The porosity of the final graft is controlled by the volume percentage of sucrose, and the diameter of the pores is dependent on the diameter of sucrose particles. **Figure 7.2** shows the SEM images of cross section area of the nHA-PEUR/MG grafts without sucrose and with 10 wt% sucrose after leaching. **Table 7.1** shows the mechanical properties of the grafts. Compression modulus and yield strength of the grafts decreased with increasing amount of sucrose, and the graft with 10 wt% sucrose exhibited compression properties slightly greater than that of natural sheep trabecular bone.[7] These results suggests that nHA-PEUR/MG grafts incorporating 10 wt% sucrose provide pores that allow for cell infiltration, while exhibiting adequate mechanical properties, thus are promising candidates for future studies.

Table 7.1 Compressive modulus and strength of nHA-PEUR/MG grafts as a function of sucrose wt%.

Sucrose wt%	Modulus (MPa)	Yield Strength (MPa)
10	620	25
20	300	18
Sheep[7]	**450**	**17**

Besides introducing porosity to the grafts, chemical formulation of the current grafts could also be modified to adjust the remodeling rate, including formulation of both the inorganic ceramic component and the organic polymer component.

The degradation rate of ceramics could be controlled by crystallinity, grain size and composition to match the rate of new bone growth. It has been reported that the *in vivo* degradation rate of amorphous calcium phosphate is faster than that of highly crystalline HA[8], and osteoclast resorption is enhanced on nanophase ceramics with grain size less than 100 nm compared to conventional ceramics with grain size larger than 100 nm.[9] Besides, β-TCP has a significantly faster degradation rate than HA.[10] Future work could test different sources of ceramic phase in the composite, including nHA particles with difference size, shape and crystallinity, and biphasic calcium phosphates that contain both HA and β-TCP.

On the other hand, the degradation rate of the organic polyurethane matrix could also be tuned by modifying the polyol component. For example, poly(thioketal urethane)s synthesized from a thioketal diol and LTI were hydrolytically stable for 6 months, while degraded within one week under oxidative conditions *in vitro*, which is much faster than 50 days reported for nHA-PEUR nanocomposites synthesized from poly(ε-caprolactone) triol (PCL300) and LTI.[11, 12] In addition, DL-lactic acid and glycolic acid could be incorporated into the PCL backbone of polyol to adjust degradation rate. **Figure 7.3** presents the preliminary data on *in vitro* degradation rates of nHA-PUR composites with different polyol formulation in oxidative environment. The nHA/PCL urethane is the same material as nHA-PEUR nanocomposites (synthesized from nHA-LTI prepolymer and PCL300) reported in Chapter III and Chapter V. The polyol component is stated here in order to distinguish with other polyurethane formulations. The nHA/PCL urethane had the slowest degradation rate under oxidative condition *in vitro*, which is in consistent with the observed slow resorption rate *in vivo*. The nHA/PTK urethane synthesized from nHA-LTI prepolymer and thioketal diol degraded rapidly within 150 hours. The nHA/polyester urethane synthesized from nHA-LTI prepolymer and copolymer of ε-caprolactone, DL-lactic acid and glycolic acid (7:2:1) had moderate degradation rate.

In summary, the remodeling rate of the nHA-PEUR/MG bone grafts could be adjusted by adjusting porosity of the grafts and modifying formulation of ceramic and polymer to achieve balanced graft resorption and new bone growth.

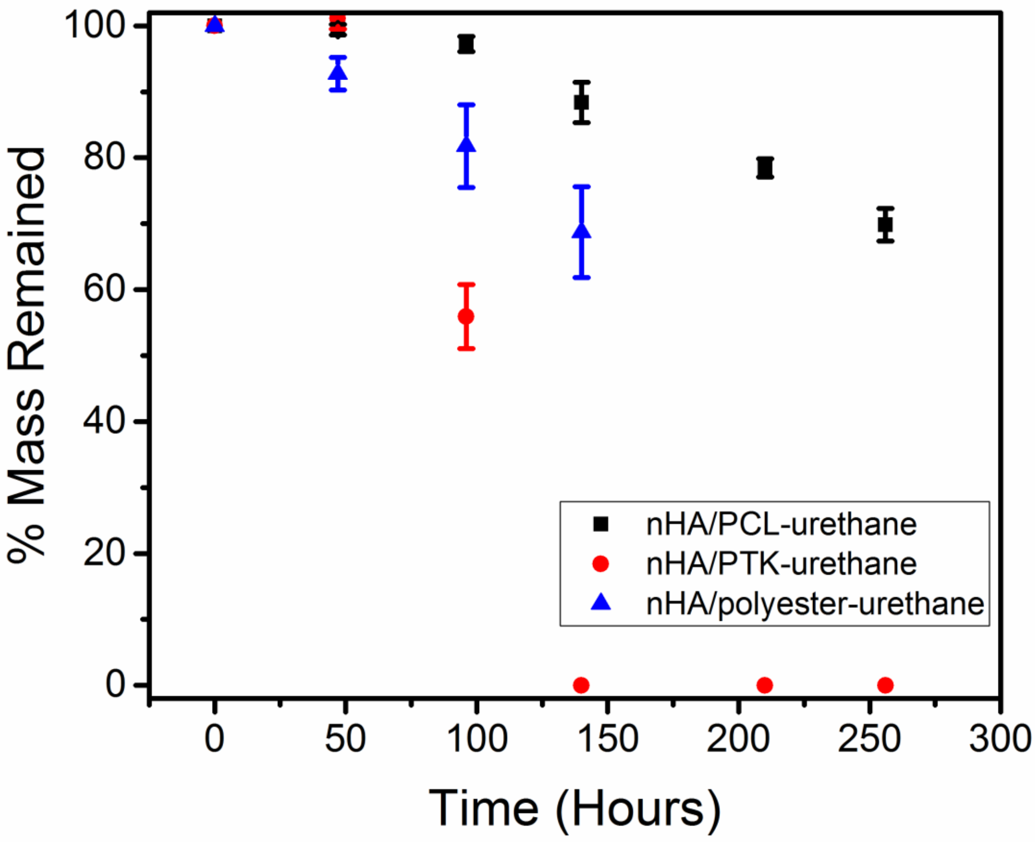

Figure 7.3 Degradation of nHA-polyurethane composites with different polyol formulations in oxidative medium

References

1. Zadpoor, A.A., *Bone tissue regeneration: the role of scaffold geometry.* Biomaterials Science, 2015. **3**(2): p. 231-245.
2. Guo, R.J., et al., *Fabrication of 3D Scaffolds with Precisely Controlled Substrate Modulus and Pore Size by Templated-Fused Deposition Modeling to Direct Osteogenic Differentiation.* Advanced Healthcare Materials, 2015. **4**(12): p. 1826-1832.
3. Vanderburgh, J., et al., *3D In Vitro Bone-templated Model of Tumor-induced Bone Disease.* Tissue Engineering Part A, 2016. **22**: p. S24-S24.
4. Thompson, W.R., C.T. Rubin, and J. Rubin, *Mechanical regulation of signaling pathways in bone.* Gene, 2012. **503**(2): p. 179-193.
5. Kwakwa, K.A., et al., *Engineering 3D Models of Tumors and Bone to Understand Tumor-Induced Bone Disease and Improve Treatments.* Curr Osteoporos Rep, 2017.
6. TA Instruments, *Electroforce Biodynamic Test Instruments Brochure*. 2016.
7. Mittra, E., C. Rubin, and Y.X. Qin, *Interrelationship of trabecular mechanical and microstructural properties in sheep trabecular bone.* Journal of Biomechanics, 2005. **38**(6): p. 1229-1237.
8. Nagano, M., et al., *Differences of bone bonding ability and degradation behaviour in vivo between amorphous calcium phosphate and highly crystalline hydroxyapatite coating.* Biomaterials, 1996. **17**(18): p. 1771-1777.
9. Webster, T.J., et al., *Enhanced osteoclast-like cell functions on nanophase ceramics.* Biomaterials, 2001. **22**(11): p. 1327-1333.
10. Degroot, K., *Clinical-Applications of Calcium-Phosphate Biomaterials - a Review.* Ceramics International, 1993. **19**(5): p. 363-366.
11. McEnery, M.A.P., et al., *Oxidatively degradable poly(thioketal urethane)/ceramic composite bone cements with bone-like strength.* Rsc Advances, 2016. **6**(111): p. 109414-109424.
12. Lu, S., et al., *Resorbable Nanocomposites with Bone-like Strength and Enhanced Cellular Activity*. Journal of Materials Chemistry B, 2017. **5**(22): p. 4198-4206.